Two-particle Response Functions in Strongly Correlated Electron Systems

by

Xi Chen

A dissertation submitted in partial fulfillment
of the requirements for the degree of
Doctor of Philosophy
(Physics and Scientific Computing)
in the University of Michigan
2017

Doctoral Committee:

Professor Emanuel Gull, chair
Professor Eitan Geva
Professor Lu Li
Professor Kai Sun
Professor Liuyan Zhao

Xi Chen

xichenli@umich.edu

ORCID iD: 0000-0002-7701-3737

ACKNOWLEDGMENTS

I am most grateful to my advisor Dr. Emanuel Gull for his patience, support, immense knowledge and demand for excellence during the last five years. Your advice on both my research and career are invaluable.

I would like to thank the members of my committee, Dr. Liuyan Zhao, Dr. Kai Sun, Dr. Lu Li, Dr. Eitan Geva andfor their time, encouragement and expertise.

My sincere thanks also goes to Dr. James LeBlanc, who collaborated with me for my two projects, for his insightful ideas and inputs. I thank my fellow labmates for the stimulating discussions, for their help with my thesis and for all the fun we had.

A special thanks to my parents and sister for their unconditional love and support.

TABLE OF CONTENTS

Acknowledgments . . . . **ii**

List of Figures . . . . **v**

Abstract . . . . **ix**

Chapter

1 Introduction **1**

- 1.1 Overview 1
- 1.2 Strongly Correlated Systems 1
- 1.3 High T_c Superconducting Cuprates 4
- 1.4 Models and Numerical Methods 10
  - 1.4.1 The Hubbard Model 10
  - 1.4.2 Dynamical Mean-field Theory 12
  - 1.4.3 Dynamical Cluster Approximation 16
  - 1.4.4 Continuous Time Auxiliary Field Impurity Solver 19
  - 1.4.5 Analytical Continuation 23

2 Two-particle vertices Response Functions **26**

- 2.1 Overview 26
- 2.2 Introduction 26
- 2.3 Two Particle Vertex Functions 28
- 2.4 Linear Response Theory 33
- 2.5 Dynamical Susceptibilities with DCA 39
- 2.6 Truncation Error 41
- 2.7 Phase Boundaries 43

3 Correlated Pairing Susceptibility **46**

- 3.1 Overview 46
- 3.2 Introduction 46
- 3.3 The Optimal Parameters 49
- 3.4 Different Symmetries 52

4 Theory of NMR Response in the Cuprates **58**

- 4.1 Overview 58
- 4.2 Introduction 58
- 4.3 Knight Shift 61

    - 4.3.1 Extract Energy Scale 64
    - 4.3.2 Spin Susceptibility Scaling 65
  - 4.4 Spin-echo Decay Rate 65
  - 4.5 Spin-lattice Relaxation Time 68

5 NMR Response Below Critical Temperature 75

  - 5.1 Overview 75
  - 5.2 Introduction 75
  - 5.3 Propagator within Nambu Formalism 77
  - 5.4 General Susceptibility 79
  - 5.5 Full Vertex and Irreducible Vertex 84
    - 5.5.1 particle-hole channel 84
    - 5.5.2 particle-particle channel 89
  - 5.6 Equation of Motion 94
  - 5.7 Knight Shift 95

6 Conclusion 102

Bibliography 104

LIST OF FIGURES

1.1 Phase diagrams of representative materials of the strongly correlated electron family. (A) An example of materials having colossal magnetoresistance effect. Structural and magnetic phase diagram of the bilayer manganite $\mathrm{La}_{2-2x}\mathrm{Sr}_{1+2x}\mathrm{Mn}_2\mathrm{O}_7$ in the range $0.3 < x < 1.0$, featuring ferromagnetic metal (FM), canted antiferromagnet (CAF), $A-$, $C-$, $G-$ type antiferomagnetic insulator, long range charge ordering (CO)[1]. (B) General phase diagram of high T_c cuprates, detailed description in the next section. (C) An example of Mott transition system.Phase diagram of single layered ruthenates[2, 3], evolving from superconducting state to AF insulator. (D) The phase diagram of nonhydrated $\mathrm{Na}_x\mathrm{CoO}_2$,determined by changing the Na content x using a series of chemical reactions. Ground state goes from a paramagnetic metal to a charge-ordered insulator, then to a Curie-Weiss metal, and finally to a weak-moment magnetically ordered state [4]. (E) Pressure-temprature phase diagram of the $\kappa-$Cl salt [5]. (F) Generally phase diagram of heavy fermion systems. Figure taken from Ref. [6]. 3

1.2 The critical temperature of superdonducting materials and their year of discovery. Materials in the same family are connected by lines and marked by same symbol. Figure form wikimedia commons. [7]. 5

1.3 Left: The crystal structure of $\mathrm{La}_{2-x}\mathrm{M}_x\mathrm{CuO}_4$, where M is Sr, Ba, or Ca. Right: the crystal structure of $\mathrm{YBa}_2\mathrm{Cu}_3\mathrm{O}_{7-y}$ in the tetragonal phase. Figure reproduced from [8]. 6

1.4 (A) Experimental results showing the existence of pseudogap in high T_c cuprates. (A) ARPES experiment results of temperature dependence of the gap in underdoped Bi 2212 at two locations in the first Brilouin zone. (B) The frequency-dependent scattering rate and the effective mass of $\mathrm{YBa}-2\mathrm{Cu}_4\mathrm{O}_8$ (C) spin-lattice relaxation rate and the Knight shift in optimally doped (squares) and underdoped (circles) YBCO, measured by NMR. (D) Tunnelling conductance for underdoped Bi2212. (E) Temperature dependence of the resistivity of underdoped $\mathrm{La}_{2x}\mathrm{Sr}_x$ CuO_4(F) Specific heat coefficient γ for (a)overdoped and(b)underdoped $\mathrm{Y}_0.8\mathrm{Ca}_0.2\mathrm{Ba}_2\mathrm{Cu}_3\mathrm{O}_7$. (G) Magnetic neutron scattering in $\mathrm{La}_{2x}\mathrm{Sr}_x\mathrm{CuO}$. (H) Raman spectra of Bi 2212. B_{1g} emphasizes processes in the $(\pi, 0)$ direction whereas B_{2g} is sensitive to the (π, π) direction. Figures selected from Ref. [9]. 8

1.5 Simplified doping dependent phase diagram of cuprate superconductors for both electron (n) and hole (p) doping. The phases shown are the antiferromagnetic (AF) phase close to zero doping, the superconducting phase around optimal doping, and the pseudogap phase. Doping ranges possible for some common compounds are also shown. Figure from [10]. 9
1.6 The iterative self-consistent loop of dynamical mean-field theory. 15
1.7 An illustration of the dynamical cluster approximation. 16
1.8 An cluster size $N_c = 4$ example of the definition of the coordinates in real and reciprocal space. The origin of a cluster in real space is labeled by $\tilde{\boldsymbol{x}}$, the sites within a cluster by $\boldsymbol{X}$. In reciprocal space, the wave-vectors of the super-lattice is labeled by $\boldsymbol{K}$, momentum within a "tile" by $\tilde{\boldsymbol{k}}$. 17
1.9 Average sign at $\beta = 15/t$, $t' = 0.1$ using 16-site cluster with continuous time auxiliary field solver. 23

2.1 The decomposition of full vertex function. Figure taken from Ref. [11] 31
2.2 full vertex functions in different channels at momentum $Q = (0, 0)$, $Q = (\pi, \pi)$ and $Q = (0, \pi)$. 34
2.3 $\chi_{ph}(\boldsymbol{q}, \nu)[N_c]$ as a function of inverse cut-off frequency. Data collected at $U = 6t$, $t' = -0.1t$, $\beta = 5/t, 7/t, 10/t, 12/t$, using 8-site cluster. 42
2.4 Comparison of χ_{0m} and χ_m. Data collected at $U = 6t$, $t' = -0.1t$, $\beta = 12/t$ on an 8-site cluster. 43
2.5 Inverse $d_{x^2-y^2}$ superconducting susceptibility plotted against temperature for the two dimensional Hubbard model with $U = 8t$, next nearest neighbor hopping t' = 0 at chemical potential $\mu = -2$, using 2 by 2 cluster. Susceptibility obtained by measuring the response of order parameter with external d-wave field strength 0.01 (solid line,circles black), 0.02 (solid line, squares, red) and 0.04 (solid line, diamonds, green). Susceptibility obtained by measuring 2-particle Green's function at normal state (solid line, triangle, blue). Also shown (right hand axis) the leading d-wave eigenvalue (solid line, star, black), $\lambda_{d_{x^2-y^2}}$, *vs* temperature. For the guide of eye, he horizontal black dashed line is where leading eigenvalue equals one. The vertical dash indicates the temprature at which $\lambda_{d_{x^2-y^2}} = 1$. 44
2.6 The leading eigenvalue of matrix $\Gamma_m \chi_0(Q = (\pi, \pi))$. Data collected at $U = 6t$, $t' = -0.1t$, using 8-site cluster. 44
2.7 AFM boundary of the 2D Hubbard model with DCA for different cluster size/configuration, next-nearest-neighbor hopping t' and interaction U. 45

3.1 Left panel: Superconducting critical temperature of the Hubbard model with nearest neighbour hopping and no next nearest neighbour hopping for $U = 6t$ using an $N_c = 8$ dynamical cluster approximation. Right panel: $P_{d_{x^2-y^2}}$ at different temperatures with $U = 6t$ and $t' = -0.1t$ using an $N_c = 8$ cluster. . . 48

3.2 Left: the contour plot of $P_{d_{x^2-y^2}}$ of the Hubbard model with nearest neighbour hopping and next nearest neighbour hopping $t' = -0.1t$ for $U = 6t$ at different temperature using an $N_c = 8$ dynamical cluster approximation. From top to bottom: $\beta = 7/t$, $\beta = 10/t$ and $\beta = 15/t$. Right: Theoretical phase diagram obtained from cluster dynamical mean-field calculations, showing Fermi liquid (yellow), superconducting (pink) and pseudogapped but not superconducting region (blue); boundary of pseudogap region shown as dashed line. Right panel adapted from Ref. [12]. 49
3.3 $P_{d_{x^2-y^2}}$ for different interaction strengths as a function of carrier concentration on an eight-site cluster, for $t' = 0$ (panel a), $t' = -0.1t$ (panel b) and $t' = -0.2t$ (panel c) at $\beta = 15/t$. $U = 4t$ (solid line, circle, black), $5t$ (dotted line, square, red), $6t$ (dashed line, diamond, green) and $7t$ (dash-dotted line, triangle, blue). 55
3.4 Contour plots for $P_{d_{x^2-y^2}}$ in space of interaction strength and carrier concentration on an 8-site cluster at $\beta = 15/t$. Top panel: $t' = 0$. Middle panel: $t' = -0.1t$. Bottom panel: $t' = -0.2t$. T_c^{max} occurs at $(U^{max}, n^{max}) = (5.5, 0.95$ and $1.05)$, $(6, 1.03)$, $(6, 1.01)$ respectively, marked by a + symbol. . . 56
3.5 The contour plot of $P_{d_{x^2-y^2}}$ in space of interaction strength and carrier concentration with only nearest neighbour hopping. Upper panel:4-site cluster, $\beta = 10/t$; middle panel: 8-site cluster, $\beta = 15/t$; bottom panel: 16-site cluster, $\beta = 5/t$. 56
3.6 Correlated pairing susceptibility P_g in different symmetry channels with interaction strength $U = 6t$, at $\beta t = 15$, using 8-site cluster. Panel(a): $t' = 0$; panel(b): $t' = -0.1t$; panel(c): $t' = -0.2t$ 57
3.7 Left: The leading eigenvalue, λ_g, in each of $x^2 - y^2$, xy, and p channels for $U/t = 2$ at $\beta t = 15$ (dashed) and $\beta t = 33$ (solid). Right: The correlated pairing susceptibility, P_g, in each of $x^2 - y^2$, xy, and p channels for $U/t = 2$ at $\beta t = 33$(solid). 57

4.1 Experimental phase diagram of multiple high T_c cuprates showing the doping dependence of psedogap energy scale and superconducting transition temprature. Data collected from both one-particle quantity probes and two-particle quantity probes. Figure taken from Ref. [13] 60
4.2 Spectral function $A(\omega, \boldsymbol{Q} = (0, \pi))$ for 8 site Hubbard model with $U = 6t$, $t' = -0.1t$, $x = 0, 0.0362, 0.0831, 0.1453$, obtained using DCA and Maxent. . 62
4.3 Side-by-side comparison of Knight shift. 63
4.4 Extraction of $\Delta_{pg(2p)}$ from Knight shift data via $\chi_m(T) = \chi_0 \exp(-\Delta_{pg(2p)}/T)$. Open symbols: data of Fig. 4.3 plotted as $log(\chi_m)$ vs. β. Dashed lines: linear fits to the data in exponentially decaying regime. Inset: comparison between pseudogap energy extracted from the slope of Arrhenius plot (open symbols, right y-axis) and from the single particle spectral function at $K = (0, \pi)$ (filled symbols, left y-axis). 65

4.5 Upper panel: the scaling behavior of Knight shift from NMR experiment on LSCO. Figure taken from Ref. [14]. Lower panel: Knight shift obtained at $U = 6t$, $t' = 0$, 8-site cluster DCA, plotted as $\chi_m(T)/\chi_{m,max}$ vs. T/T_{max}. The resulting scaling curve is a "Universal Curve F" [14] 66
4.6 Temperature dependence of $1/T_2$ in various material. (Fig. 8 in Ref. [15]) . . . 67
4.7 Spin echo decay time T_{2G} as a function of temperature for doping level ranging from $x = 0$ to $x = 0.145$, calculated at $U = 6t$, $t' = -0.1t$. Inset: spin echo decay rate T_{2G}^{-1}. 67
4.8 Spin lattice decay rate of 8-site Hubbard model at $U = 2t$, $t' = 0$. Black solid line, open circle symbol: RPA results. Green solid line with error bar: DCA results. 71
4.9 Side-by-side comparison of $(T_1T)^{-1}$ for copper and oxygen sites. 72
4.10 (a) Zero frequency spin susceptibility at different momentum Q for various temperatures. Inset: The same data, zoomed in near $Q = (0, 0)$.(b) The structure factor for copper ($^{63}F_{\|}$) and oxygen ($^{17}F_{\|}$) sites given by equation 4.5. 74

5.1 The diagram of one particle propagators. From to top to bottom: $G_\sigma(k)$, $F^*_\sigma(k)$, $F_\sigma(k)$. 78
5.2 Upper left: the diagram of normal vertex in particle-hole channel. Upper right: the diagram of anomalous vertex in particle-hole channel. Lower left: the diagram of normal vertex in particle-particle channel. Upper Lower right: the diagram of anomalous vertex in particle-particle channel. 83
5.3 Upper: the diagram of Eq. 5.23. Lower: the diagram of Eq.5.24. 85
5.4 Upper: the diagram of normal full vertex in particle-hole channel. Lower: the diagram of anomalous full vertex in particle-hole channel. 88
5.5 Upper: the diagram of normal full vertex in particle-particle channel. Lower: the diagram of anomalous full vertex in particle-particle channel. 97
5.6 The diagram of the definition of full vertex in particle-particle channel in $pp\overline{\uparrow\downarrow}$ spin-combination. 98
5.7 The diagram of equation of motion in $ph-$channel. 99
5.8 The diagram of equation of motion in $pp-$channel. 100
5.9 The temperature dependence of the Knight shift of chain Cu(1) and planar Cu(2) nuclei in $YBa_2Cu_3O_7$ with different field orientations. The crosses and filled circles are the results with and without diamagnetic field correction, respectively. Panel(c) inset: magnetization at the same field. Figure reproduced from Ref. [16] 101
5.10 Red solid line, square symbol: the Knight shift with temperature range extending into superconducting states. Black solid line, circle symbol: order parameter $F = \langle Tc_\uparrow c_\downarrow \rangle$. Data obtained using $U = 6t$, $t' = 0$, 8 site cluster, DCA calculation. 101

ABSTRACT

In this thesis, we use the dynamical cluster approximation to study strongly correlated electron systems, especially from the angle of two-particle quantities, such as dynamical susceptibilities and vertex functions.

The thesis starts with an introduction to the strongly correlated systems, including their definitions, prominent features, applications, difficulties in explaining them theoretically and some numerical approaches developed. The following section is an introduction to one family of strongly correlated systems we focus on in this thesis, the high temperature cuprates. The salient features in their general phase diagrams are described and discussed. Then an overview of the model we used to study high T_c cuprates is provided, with its limitations and extensions. To solve this model, the numerical method we employ for our study is the dynamical mean-field theory, the dynamical cluster approximation and the continuous time auxiliary field impurity solver. the last part of Chap.1 contains brief derivations for these algorithms.

In Chap. 2, we apply dynamical cluster approximation to solve the one-band 2D Hubbard model. The physical quantities of interest are two-particle quantitites, such as the dynamical susceptibility, irreducible vertex functions and full vertex functions. In this chapter, we describe how to obtain these susceptibilities via linear response theory and write down a detailed example for superconducting susceptibility. Finally we show how to calculate two particle quantities within DCA and obtain phase boundary with them.

Chap. 3 is based on one of our publications. In this work, we specifically address the problem of optimizing the superconducting transition temperature in the 2D Hubbard model by analyzing wide regions of parameter space in density, interaction, and second-nearest-neighbor hopping strength.We mainly focus on d_{x2-y2} superconductivity but show results of other symmetries in the last section.

Chap. 4 follows another publication of ours. We study the temperature and doping evolution of NMR response in the normal state of the 2D Hubbard model using cluster dynamical mean-field theory. We simulate the Knight shift, the spin-echo decay rate and the spin-lattice relaxation time, and compare them to the cuprates experimental results.

The last chapter extends the calculation of the NMR response to the superconducting state with the Nambu formalism. We show the detailed formulas and diagrams to calculate two-particle quantities, including the Dyson-Schwinger equation of motion.

CHAPTER 1

Introduction

1.1 Overview

This thesis focuses on the numerical studies of strongly correlated electron systems. In this chapter, we provide background informations about strongly correlated system, especially the high T_c superconductors. We describe the fundamental aspects of the features, applications and theoretical challenges of strongly correlated electron systems. Then we proceed to the numerical method employed in the following chapters, the dynamical mean-field theory, dynamical cluster approximation, the continuous time auxiliary field impurity solver and the maximum entropy method for analytical continuation.

1.2 Strongly Correlated Systems

In this section, we provide some fundamental information about strongly correlated systems, which is the topic this thesis focused on. The field of strongly correlated systems is one of the most intensively studied fields in condensed matter physics. In these systems, the interaction between constituent particles is comparable to or stronger than their kinetic energy and plays an important role in determining the properties of the materials, hence the name strongly correlated system. Examples of such systems include high temperature superconductors [17], heavy fermion materials [18], manganites [19], transition metal oxides

[17], organic superconductors [20], quantum Hall systems [21] and others. Many of these materials have open d or f electron shells, where electrons occupy narrow orbitals. Those orbitals make electrons spatially confined and experience strong Coulomb repulsion [22]. The comparability of energy scales of spin, charge and orbital degrees of freedom results in interplay effects and competing orders in some regions of their phase diagrams, such as competing magnetic stripe order and superconductivity in pnictide materials [23]. It also makes the system very sensitive to changes in external parameters [22], such as temperature, doping or magnetic field, producing feature-rich phase diagrams. Fig. 1.1 lists the phase diagrams of some widely studied materials belong to the category of strongly correlated systems. What stimulates the research in these materials is not only the challenge of understanding the fundamental mechanism of electronic interaction, but also the great potential in technological applications based on their exotic emergent phenomena. For instance, current commercial applications of high T_c superconductors include magnetic resonance imaging [24], high-energy physics accelerators [25], plasma fusion reactors [26] and power transmission lines. Colossal magnetoresistance effects can be exploited for sensitive magnetic field sensor and the magnetocaloric effects provide a new cooling method[27].

The difficulty of constructing a complete theoretical explanation of strongly correlated systems is rooted in the fact that they cannot be understood as ensemble of free particles or quasi-particles. Interesting emergent properties are not a mere accumulation of individual building blocks but are brought about by the pronounced electron-electron interaction [6]. Their complexity requires theories that are qualitively different from those that govern its individual units [28]. Under these circumstances, traditional *ab initio* methods are bound to fail. With multiple fluctuations activated within comparable energy scales, methods such as density functional theory and band theory are incapable of incorporating interactions properly [22] due to their perturbative nature. For example, for high T_c cuprates, band theory mistakes its Mott-insulating parent compounds for metal [29], Fermi liquid theory gives wrong answers in the strange metal and pseudogap region [30]. In the superconducting

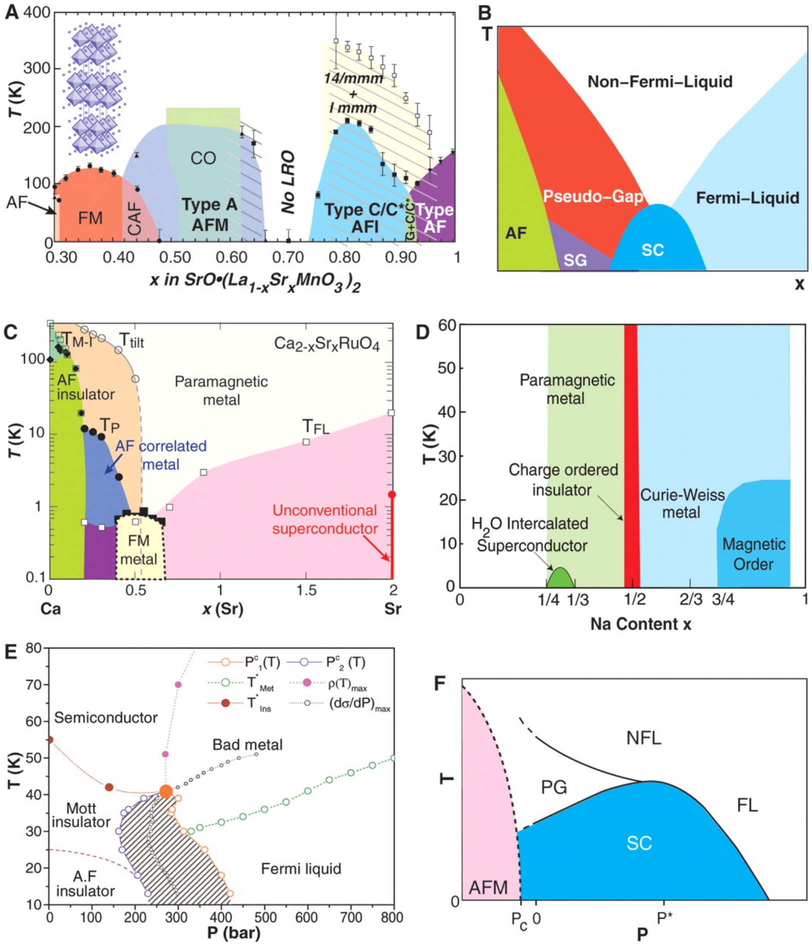

Figure 1.1: Phase diagrams of representative materials of the strongly correlated electron family. (A) An example of materials having colossal magnetoresistance effect. Structural and magnetic phase diagram of the bilayer manganite $La_{2-2x}Sr_{1+2x}Mn_2O_7$ in the range $0.3 < x < 1.0$, featuring ferromagnetic metal (FM), canted antiferromagnet (CAF), $A-$, $C-$, $G-$ type antiferomagnetic insulator, long range charge ordering (CO)[1]. (B) General phase diagram of high T_c cuprates, detailed description in the next section. (C) An example of Mott transition system.Phase diagram of single layered ruthenates[2, 3], evolving from superconducting state to AF insulator. (D) The phase diagram of nonhydrated Na_xCoO_2 ,determined by changing the Na content x using a series of chemical reactions. Ground state goes from a paramagnetic metal to a charge-ordered insulator, then to a Curie-Weiss metal, and finally to a weak-moment magnetically ordered state [4]. (E) Pressure-temprature phase diagram of the $\kappa-$Cl salt [5]. (F) Generally phase diagram of heavy fermion systems. Figure taken from Ref. [6].

state, its d-wave pairing symmetry, the very short coherent length and the high transition temperature are far away from predictions made by BCS theory [31].

In order to get theoretical understanding of strongly correlated materials, a common approach is to extract a few important degrees of freedom from the original Hamiltonian and construct a low energy effective model [22]. However, most models that still retain the essence of physical phenomena lack exact analytical solutions, which is why, along with the fast-paced development of high performance computers, thriving numerical methods have emerged as an important tool in this field in the last decade. The most commonly used numerical techniques are Quantum Monte Carlo (QMC) and Exact Diagonalization (ED). QMC is plagued by the infamous sign problem [32] when applied to fermionic systems. Namely, the sampling weights for different configurations become negative when the temperature is lowered or when the cluster size is increased. ED is only capable of handling small systems since the Hilbert space increases exponentially with the cluster size.

Over the years, researchers have made great strides in developing numerical algorithms to study strongly correlated systems, such as auxiliary-field quantum Monte Carlo (AFQMC) [33, 34], bare and bold-line diagrammatic Monte Carlo (DiagMC) [35, 36, 37], the dual fermion method (DF) [38], density matrix embedding theory (DMET) [39, 40], density matrix renormalization group theory (DMRG) [41, 42], cluster dynamical mean-field theory (CDMFT) and the dynamical cluster approximation (DCA) [43], diffusion Monte Carlo based on a fixed-node approximation (FN) [44, 45], unrestricted coupled cluster theory including singles and doubles (UCCSD), and in certain cases, higher excitations [46], and multireference projected Hartree-Fock (MRPHF) [47, 48]. Ref. [49], a benchmarking project for 2D Hubbard model, shows results from all the methods mentioned above.

1.3 High T_c Superconducting Cuprates

One of the most prominent and widely studied class of strongly correlated materials is the class of high T_c superconductors. The pursuit of higher temperature superconductors started with the discovery of superconductivity in 1911, when Dutch physicist Heike

Kamerlingh Onnes observed almost zero electrical resistance in mercury at 4.19 K [50]. In the subsequent decades, superconductivity was found in multiple kinds of materials. Their year of discovery and maximum transition temperature are shown in Fig. 1.2. The copper-oxygen superconductors are usually called "high T_c" superconductors, since their transition temperatures exceed the boiling point of liquid nitrogen at ambient pressure.

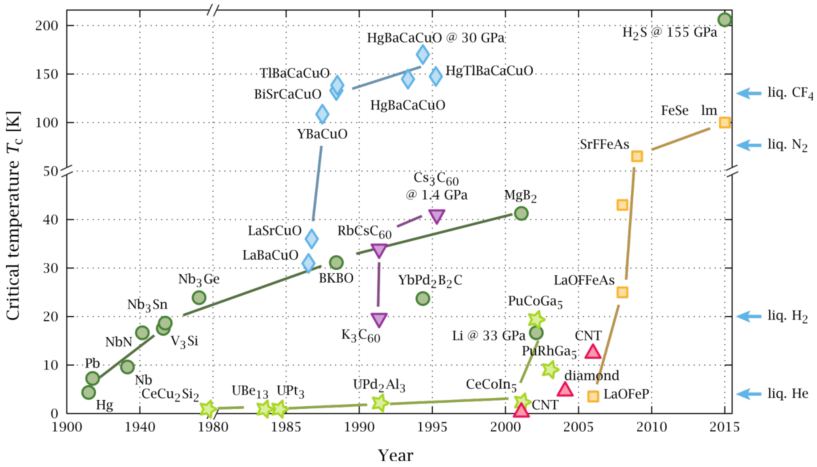

Figure 1.2: The critical temperature of superdonducting materials and their year of discovery. Materials in the same family are connected by lines and marked by same symbol. Figure form wikimedia commons. [7].

Currently discovered copper-based superconductors generally fall into three categories [8]. The lanthanum stronium copper oxide (LSCO), which was the first being discovered, has the K_2NiF_4 crystal structure (a body-centered tetragoanl lattice ($I_4/mmm - D_{4h}^{17}$), as shown in Fig.1.3. The coupling between its adjacent layers are extremely weak [8], so that it is a very suitable material to be simulated by 2D models. By substituting Sr^{2+} cations for La^{3+}, its overall density of doped hole can be tuned continuously from antiferromagnetic phase to superconducting dome and further into overdoped region [14]. Therefore, LSCO is considered a good candidate for studying superconductivity regardless of its relatively lower critical temperature.

The Yttrium Barium copper oxide (YBCO) family was discovered within one year after LSCO and increased maximum critical temperature from 45K to 93K [7]. Within its perovskite crystal structure[8], shown in the left panel of Fig 1.3, two CuO planes are separated by a single layer of Y^{3+} ions. Its doping level is controlled by number of oxygen per formula unit, with $\mathrm{YBa_2Cu_3O_6}$ being the undoped compound [14]. the superconducting properties of $\mathrm{YBa_2Cu_3O_{7-x}}$ are sensitive to its oxygen content.

Bi, Tl and Hg-type compounds, the STM and ARPES experimentalists' favorite materials, have up to 3 CuO layers, even more with external pressure. In 1994, a group in University of Houston was able to push the transition temperature of $\mathrm{HgBa_2Ca_2Cu_3O_{8+\delta}}$ to 164K under quasihydrostatic pressure 30GPa [51].

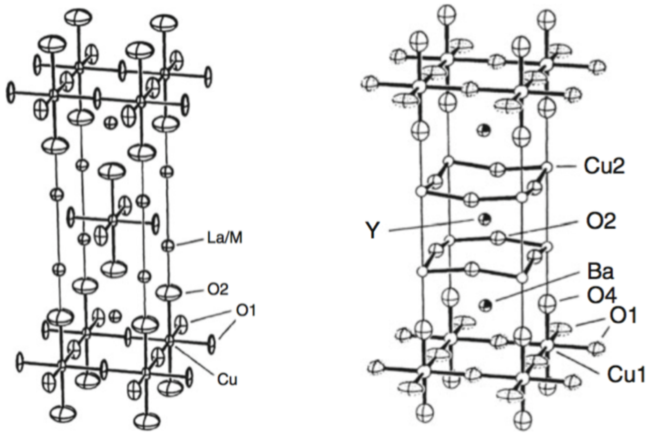

Figure 1.3: Left: The crystal structure of $\mathrm{La_{2-x}M_xCuO_4}$, where M is Sr, Ba, or Ca. Right: the crystal structure of $\mathrm{YBa_2Cu_3O_{7-y}}$ in the tetragonal phase. Figure reproduced from [8].

There are several common features among high T_c cuprate materials. Their key structural feature is the quadratic $\mathrm{CuO_2}$ arrays separated from each other by charge reservoir layers. In these planes, the Cu $d_{s^2-y^2}$ orbitals are bonded to four O p orbitals [8]. The physics of these materials are strongly two dimensional. Strong magnetic correlation between intraplane Cu ions makes the parent compounds antiferromagnetic at low temperature [14]. The hopping process that might lead to conduction is suppressed by coulomb repulsion. Therefore the so called Mott insulator is observed at half-filling. With hole doping the magnetic order quickly disappear and conducting or superconducting phase emerges. A simplified doping dependent phase diagram of high T_c cuprate is presented in Fig. 1.5.

High T_c cuprates have been a fanscinating research topic ever since their discovery. They have drastically different behavior as compared to ordinary d-band metals, both in the normal and the superconducting states. One particularly interesting phenomenon that exists in high T_c cuprates is the pseudogap at the hole doped side. This is a state in which the normal state electronic density of states at fermi level exhibits a momentum dependent depression. It is largest close to antinodal region around $\boldsymbol{k} = (0, \pi)$ in the Brillouin zone and vanishes towards the nodal region direction $\boldsymbol{k} = (0, 0)$ to $\boldsymbol{k} = (\pi, \pi)$ [52].

The existence of pseudogap (PG) has been confirmed by various experimental techniques. It was first discovered by the nuclear magnetic resonance experiment, in the form of reduction of Knight shift (K_s) and spin relaxation time T_1 at temperature below certain T^* see Fig. 1.4(C). Direct evidence is also provided by measurements of the tunneling conductance. A gap-like feature at zero bias is seen to persist in the normal state (see Fig. 1.4(D). Another smoking gun is the specific heat. Fig. 1.4(F) shows specific heat coefficient for (a)overdoped and (b)underdoped $\mathrm{Y_{0.8}Ca_{0.2}Ba_2Cu_3O_7}$. In the overdoped material a gap, signaled by a depression, opens up below T_c. In the underdoped samples a gap starts to form in the normal state below 140 K. The PG also manifest itself in electronic Raman scattering (Fig. 1.4(H)). There is a prominent peak in the B_{1g} Raman spectra which represents the $(0, \pi)$ direction. The magnetic neutron scattering shows a peak in the imaginary part of spin susceptibility in the PG region (Fig. 1.4(G)). The measurement of dc resistivity has a drop at a temperature T^* due to reduced scattering as the result of the formation of the pseudogap (Fig. 1.4(E)). Fig. 1.4(B) is the result of ab-plane optical conductivity. The scattering rate varies linearly at room temperature but develops a gap like depression in the normal state. At the same time the effective mass of the carriers develops a resonance peak. The most powerful technique to study PG is the angle-resolved photoemission spectroscopy (ARPES), which directly measure the density of states at fermi level. As shown in Fig. 1.4(A), a gap in spectral function opens at antinode, small frequency below certain temperature and closes at points closer to node.

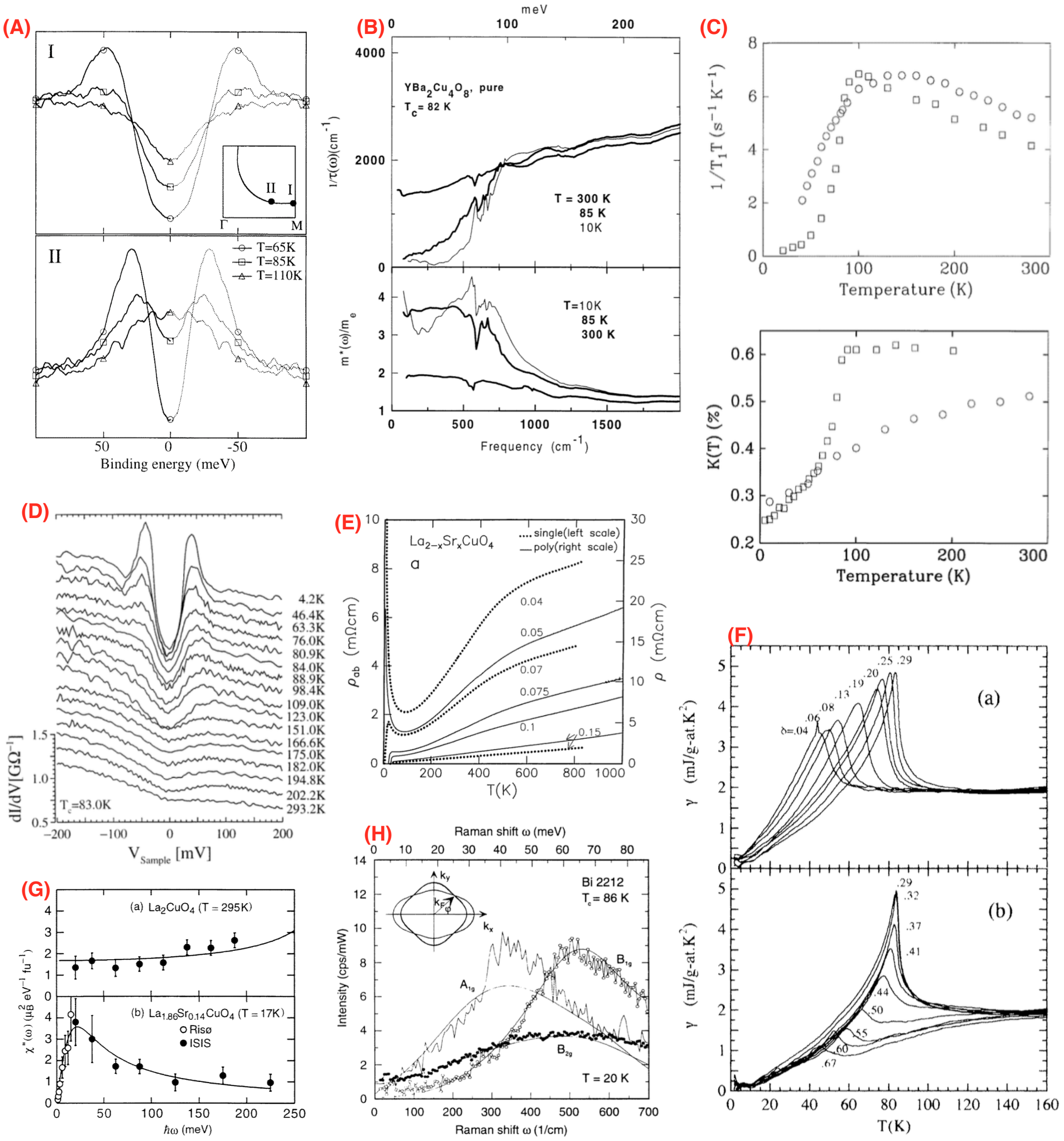

Figure 1.4: (A) Experimental results showing the existence of pseudogap in high T_c cuprates. (A) ARPES experiment results of temperature dependence of the gap in underdoped Bi 2212 at two locations in the first Brilouin zone. (B) The frequency-dependent scattering rate and the effective mass of YBa-2Cu$_4$O$_8$ (C) spin-lattice relaxation rate and the Knight shift in optimally doped (squares) and underdoped (circles) YBCO, measured by NMR. (D) Tunnelling conductance for underdoped Bi2212. (E) Temperature dependence of the resistivity of underdoped La$_{2x}$Sr$_x$ CuO$_4$(F) Specific heat coefficient γ for (a)overdoped and(b)underdoped Y$_0$.8Ca$_0$.2Ba$_2$Cu$_3$O$_7$. (G) Magnetic neutron scattering in La$_{2x}$Sr$_x$CuO. (H) Raman spectra of Bi 2212. B_{1g} emphasizes processes in the $(\pi, 0)$ direction whereas B_{2g} is sensitive to the (π, π) direction. Figures selected from Ref. [9].

The pseudogap onset temperature T^* is much larger in underdoped samples, decreases with increased doping level and eventually disappear in overdoped samples. There has been a heated debate about the interplay between pseudogap and superconductivity. It has been variously argued that the pseudogap is a precursor of superconducting fluctuations, of a competing nonsuperconducting phase or regime, or of physics not contained in the Hubbard model. In later chapters, we will show simulation results of the 2D Hubbard model that supports the idea that the physics of pseudogap is contained in the 2D Hubbard model and competes with the superconducting state.

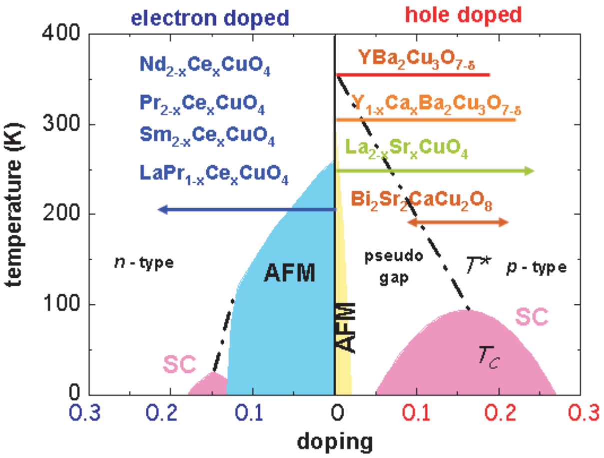

Figure 1.5: Simplified doping dependent phase diagram of cuprate superconductors for both electron (n) and hole (p) doping. The phases shown are the antiferromagnetic (AF) phase close to zero doping, the superconducting phase around optimal doping, and the pseudogap phase. Doping ranges possible for some common compounds are also shown. Figure from [10].

1.4 Models and Numerical Methods

1.4.1 The Hubbard Model

Due to the non-perturbative nature of strongly correlated electron systems, theoretical studies have been very challenging. As mentioned in previous section, one approach is to extract a simpler effective Hamiltonian from the orginal problem, for example, the Falicov-Kimball model [53], the $t-J$ model [54], the Emery model [55] or the Heisenberg model [56]. This thesis focuses on the study of the Hubbard model. Initially proposed in the early 1960s, the Hubbard model offers a simple description of electrons interacting with each other in periodic potentail. The Hamiltonian of Hubbard model is [57, 58]

$$H = \sum_{\boldsymbol{k},\sigma} \left(\epsilon_{\boldsymbol{k}} - \mu\right) c^{\dagger}_{\boldsymbol{k}\sigma} c_{\boldsymbol{k}\sigma} + U \sum_{i} n_{i\uparrow} n_{i\downarrow}, \tag{1.1}$$

where μ is the chemical potential, $\boldsymbol{k}$ momentum, i labels of sites in real-space, U the on site Coulomb interaction, and the dispersion $\epsilon_{\boldsymbol{k}} = -2t\left[\cos(\boldsymbol{k}_x) + \cos(\boldsymbol{k}_y)\right] - 4t' \cos(\boldsymbol{k}_x)\cos(\boldsymbol{k}_y)$, t the hopping matrix amplitude.

The Hubbard model starts its success with understanding the Mott insulator state of several transition metal oxides [59, 60], which would otherwise be predicted by band structure theory as metallic. One more recent successful application is modeling the high temperature cuprates. Phillip W. Anderson stated that the essential physics of high T_c superconductor was contained in the two dimensional Hubbard model [61]. The one band Hubbard model retains the Cu $d_{x^2-y^2}$ orbital while other Cu orbitals and O orbitals are neglected. This model is well acknowledged to be able to capture the important features of the phase diagram of cuprates, including the Mott metal-insulator transition, the anti-ferromagnetic phase, the superconducting phase, and the pseudogap.

Despite the successful application of the Hubbard model in many strongly correlated systems, there is a growing recognition that theoretical analysis of many newly developed materials or newly observed phenomena require more realistic models. There are various of extension to the Hubbard model that reinclude some more details of the high T_c cuprates. The first type is use three bands instead of the effective one band [55]. One fo the studies of three-band Hubbard model [62] with single-site DMFT concluded that one-band model provides reliable picture of the spectral functions and conductivity for frequencies less than 4eV. Ref. [63] investigates the intermediate energy properties of cuprates using LDA+DMFT method to solve three-band Hubbard model and reported that three-band Hubbard model can be reduced to one-band Hubbard model at electron doped side and hole doped side when charge transfer energy is much larger then copper-oxygen hybridization. Similar comparison was also made in Ref. [64]. One thing that they could agree on is that one band Hubbard model works well on low energy scale.

There are also DMFT studies of bilayer Hubbard model [65, 66], which is necessary when interlayer pairing is not negligible. We will also discuss the difference between the NMR signal of LSCO (single CuO layer mateiral) and YBCO (double CuO layer material) in Chap. 4 and Chap. 5

Another extension is the extended Hubbard model which includes not only the onsite but also the nearest neighbor interaction [67]. This also gives rise to new phases in the dynamical mean-field result, such as charge density wave. It has also been found that intersite interaction may be essential for the Wigner-Mott metal-insulator transition [67]. New experimental progress in cold atoms [68, 69] has also intrigued the interest of studying the 3D Hubbard model, which is much more numerically expensive than the 2D Hubbard model.

This thesis is focused on the study of the single orbital Hubbard model in two dimensions on a square lattice with nearest and next-nearest hopping parameters. The main approximations that justify using the one-band, 2D Hubbard model for high T_c cuprates are (1) their physics is believed to be dominated by the almost square CuO_2 plane(s); (2) The interaction between electrons is strongly screened so it almost purely local. For real high

T_c material, interaction $U \approx 7.5t$, $t' \approx -0.15$ for LSCO and $t' \approx -0.3$ for YBCO. t is the unit energy scale, approximately $0.3\ eV$.

1.4.2 Dynamical Mean-field Theory

Despite the simplicity of one-band 2D Hubbard model, it can only be solved exactly in the limit of $d = 1$ [70, 71] and $d = \infty$ (within DMFT [72, 73]). Dynamical mean-field theory (DMFT [72, 73]) has been proved to be a powerful tool for solving the Hubbard model. DMFT is an approximation scheme developed for solving quantum many-body problems. The main idea of dynamical mean-field theory is to map the original lattice problem to a Anderson impurity model subject to a noninteracting, self-consistent bath [73]. DMFT accounts for the correlation between spatially localized degrees of freedom explicitly, while longer range correlations are approximated in a mean-field way. In contrast to perturbative approaches, such as the random phase approximation (RPA) [74] and third-order perturbation method, it treats local quantum fluctuations in a nonperturbative manner. All Feynman diagrams are taken into account, albeit only the local contribution to the self-energy. Therefore, DMFT is suitable for strongly correlated systems in the region where diverse and complicated phases emerge, beyond the limit of weak coupling but where correlations are precominantly local. Additionally, it can be combined with a realistic electronic structure theory to generate numerical calculations for real materials. Examples are LDA+DMFT [75] or GW+DMFT [76].

There are multiple approaches to derive DMFT, including the cavity method [72], local nature of perturbation theory in infinite dimensions [77], expansion around the atomic limit [73], effective medium theory [73] and Potthoff self-energy functional [78]. Ref. [73] presented a derivation for DMFT, starting with removing one lattice site and all its bonds with the rest of the lattice. The remaining lattice is simplified to a dynamical mean-field, i.e. the bath. It is coupled to the representative single site via hybridization. The problem is thus converted to a Anderson impurity problem, which is numerically tractable.

Use Hubbard model as an example, the partition function can be written as a path integral over Grassman variables, with the action S

$$Z = \int \prod_i Dc^*_{i\sigma} Dc_{i\sigma} e^{-S} \tag{1.2}$$

$$S = \int_0^\beta d\tau \left[\sum_{i\sigma} c^*_{i\sigma}(\tau)(\frac{\partial}{\partial \tau} - \mu) c_{i\sigma}(\tau) + \sum_{ij\sigma} t_{ij} c^*_{i\sigma}(\tau) c_{j\sigma}(\tau) + \sum_i U c^*_{i\uparrow}(\tau) c_{i\uparrow}(\tau) c^*_{i\downarrow}(\tau) c_{i\downarrow}(\tau) \right], \tag{1.3}$$

where $c^*_{i\sigma}$ and $c_{i\sigma}$ are Grassman variables, τ the imaginary time, μ the chemical potential, t_{ij} the hopping parameter and U interaction. This action can be separated into the impurity part S_0, the lattice part $S^{(0)}$ and the hybridization part δS as $S = S_0 + S^{(0)} + \Delta S$, where

$$S_0 = \int_0^\beta d\tau \left[\sum_\sigma c^*_{0\sigma}(\tau)(\frac{\partial}{\partial \tau} - \mu) c_{0\sigma}(\tau) + U c^*_{0\uparrow}(\tau) c_{0\uparrow}(\tau) c^*_{0\downarrow}(\tau) c_{0\downarrow}(\tau) \right] \tag{1.4}$$

$$\Delta S = \int_0^\beta d\tau \sum_{i\sigma} [t_{i0} c^*_{i\sigma}(\tau) c_{0\sigma}(\tau) + t_{0i} c^*_{0\sigma}(\tau) c_{i\sigma}(\tau)] \tag{1.5}$$

$$S^{(0)} = \int_0^\beta d\tau \left[\sum_{i\neq 0\sigma} c^*_{i\sigma}(\tau)(\frac{\partial}{\partial \tau} - \mu) c_{i\sigma}(\tau) + \sum_{ij\neq 0\sigma} t_{ij} c^* i\sigma(\tau) c_{i\sigma}(\tau) + U \sum_{i\neq 0} c^*_{i\uparrow}(\tau) c_{i\uparrow}(\tau) c^*_{i\downarrow}(\tau) c_{i\downarrow}(\tau) \right] \tag{1.6}$$

The partition function in grand canonical ensemble can be separated accordingly as

$$\begin{aligned} \mathcal{Z} &= \int \prod_\sigma Dc^*_{0\sigma} Dc_{0\sigma} exp[-S_0] \times \int \prod_{i\neq 0\sigma} Dc^*_{i\sigma} Dc_{i\sigma} \exp[-S^{(0)}] \exp[-\Delta S] \\ &= \mathcal{Z}^{(0)} \int \prod_\sigma Dc^*_{0\sigma} Dc_{0\sigma} \exp[-S_0] \langle \exp[-\Delta S] \rangle_{(0)} \end{aligned} \tag{1.7}$$

where $\langle X\rangle_{(0)}$ is the ensemble average $\frac{1}{\mathcal{Z}^{(0)}}\int\prod_{i\neq 0\sigma} Dc^*_{i\sigma}Dc_{i\sigma}X\exp[-S^{(0)}]$. By expanding the exponential enclosed by$\langle\rangle$ with respect to ΔS, the local action can be written into the form

$$S_{loc} = -\int_0^\beta d\tau_1\int_0^\beta d\tau_2\sum_\sigma c^*_\sigma(\tau_1)\mathcal{G}^{-1}_\sigma(\tau_1-\tau_2)c_\sigma(\tau_2) + U\int_0^\beta d\tau c^*_\uparrow(\tau)c_\uparrow(\tau)c^*_\downarrow(\tau)c_\downarrow(\tau)$$

where

$$\mathcal{G}^{-1}_\sigma(\tau_1-\tau_2) = -(\frac{\partial}{\partial\tau_1}-\mu)\delta_{\tau_1\tau_2} + \sum_{ij\neq 0} t^*_{i0}t^*_{j0}G^{(0)}_{ij\sigma}(\tau_1-\tau_2) \tag{1.8}$$

Then the Green's function of the removed site and the Green's function of the remaining lattice is related by

$$G^{(0)}_{ij\sigma} = G_{ij\sigma} - G_{i0\sigma}G^{-1}_{00\sigma}G_{0j\sigma} \tag{1.9}$$

Here I described the main steps in the derivation of DMFT. Interested readers can refer to the review by Geroges and Kotliar [73], or the review of D.Vollhardt *et al.* [77] for more details.

Fig. 1.6 depicts the iterative scheme of DMFT. Note that the degrees of the freedom of the bath, generally denoted as bare Green's function G_0, are solved self-consistently, hence the name "self-consistency loop".

The selfconsistent loop starts with a guess for the bare Green's function G_0. As has been discovered [79] using DMFT and half-filled Hubbard model, in the "coexistence" region of the phase diagram, the choice of beginning $G_0(\omega)$ will affect the final converged Green's function, either metallic or Mott-insulating. With this initial G_0, one solves the impurity problem using an "impurity solver" and obtain the the Green's function for the impurity $G_{imp}(\omega)$. The self-energy of the impurity is then calculated by the Dyson equation.

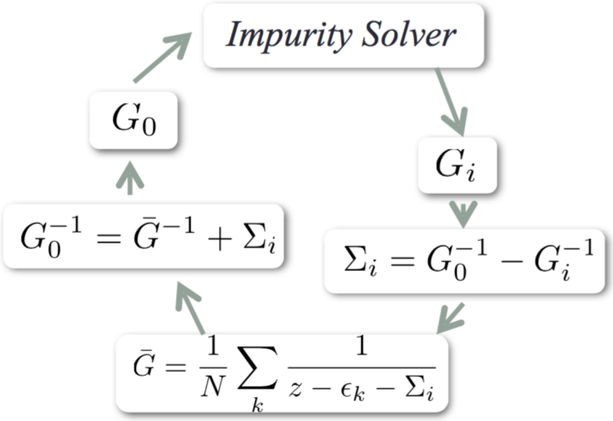

Figure 1.6: The iterative self-consistent loop of dynamical mean-field theory.

$$\Sigma_{imp}(\omega) = G_0^{-1}(\omega) - G_{imp}^{-1}(\omega) \tag{1.10}$$

Within DMFT approximation, the lattice self-energy is the same as the momentum-independent impurity self-energy $\Sigma(k,\omega) = \Sigma(\omega)$. Once self-energy is known, the lattice Green's function is calculated by coarse graining

$$\bar{G}(\omega) = \frac{1}{N}\sum_k \frac{1}{i\omega_n + \mu + \epsilon_k - \Sigma(\omega)} \tag{1.11}$$

Then, new impurity Green's function is recalculated by

$$G_0(\omega)^{-1} = \bar{G}(\omega)^{-1} + \Sigma(\omega)^{-1} \tag{1.12}$$

This procedure is repeated iteratively until Green's function converges. The convergence rate of the Green's function is related to the initial bare Green's function and drastically decrease when the system is close to a phase transition, due to critical slowing down.

1.4.3 Dynamical Cluster Approximation

What can we do beyond DMFT? The motivation for this question is that the applicability of DMFT is by construction limited to materials and properties where spatial correlations can be neglected. The drawbacks are now apparent. It fails to describe independent variations of the quasiparticle residue, the quasiparticle lifetime and the effective mass [80]. It fails to treat more exotic orders whose order parameters involve more than one site, such as antiferromagetism, stripe states, d-wave superconductivity, or charge density waves [81, 82]. All of these states have been observed experimentally in multiple systems (see Fig. 1.1)

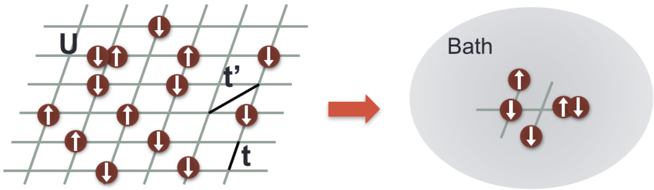

Figure 1.7: An illustration of the dynamical cluster approximation.

Over the years, various extentions to DMFT have been introduced. One direction is the cluster extention approach, which treats the non-local short range correlation explicitly within the cluster and the long range correlation on a mean-field level, as illustrated in Fig. 1.7. This method uses finite clusters instead of a single site as the impurity. This approach includes the dynamical cluster approximation (DCA)[43] and the cluster dynamical mean-field theory (CDMFT)[83, 84]. They succeeded in obtaining a d-wave pairing and antiferromagnetic solution in the Hubbard model for parameters relevant to high T_c superconductors and the effects of on site Coulomb interaction in various transition metal oxides but fails in describing Luttinger liquid formation or van Hove singularities [85].

Another direction of going beyond DMFT are diagrammatic extentions of DMFT. For example, the dual fermion approach [85], the dynamical vertex approximation [86], the multiscale many-body method [87] and self-energy functional theory [88].

In this thesis, we will use the DCA method. With DCA, the first Brillouin zone is

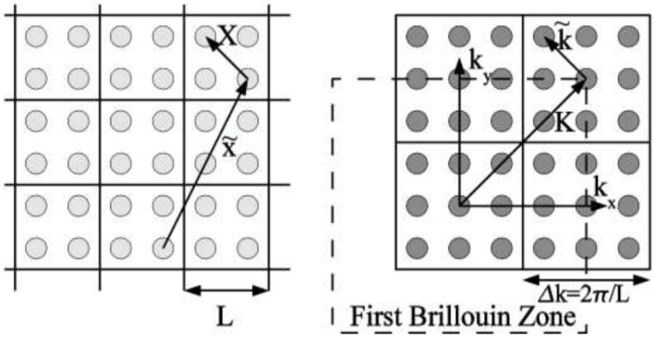

Figure 1.8: An cluster size $N_c = 4$ example of the definition of the coordinates in real and reciprocal space. The origin of a cluster in real space is labeled by $\tilde{\boldsymbol{x}}$, the sites within a cluster by $\boldsymbol{X}$. In reciprocal space, the wave-vectors of the super-lattice is labeled by $\boldsymbol{K}$, momentum within a ”tile” by $\tilde{\boldsymbol{k}}$.

partitioned into N_c patches and the electron self-energy is constant within each patch. The result becomes exact as the size of the cluster tends to infinity. It makes use of the space translational invariance of the lattice and substantially reduces the computational burden by doing calculation in the momentum space. The following derivation of DCA closely follows the review of Maier [43].

In real space, the coordinates of a site is decomposed into the coordinate of cluster and the coordinate within the cluster. Their reciprocal space coordinates are defined in a similar manner, namely

$$\boldsymbol{x} = \tilde{\boldsymbol{x}} + \boldsymbol{X} \tag{1.13}$$

$$\boldsymbol{k} = \boldsymbol{K} + \tilde{\boldsymbol{k}} \tag{1.14}$$

The kinetic term (electron hopping term) in the Hamiltonian can be transformed to dispersion relation $\epsilon_{\boldsymbol{k}}$ with the following Fourier transform that preserves translational invariance of the lattice.

$$[t_{DCA}(\tilde{\boldsymbol{k}})]_{\boldsymbol{X}_i \boldsymbol{X}_j} = \frac{1}{N_c} \sum_{\boldsymbol{K}} e^{i\boldsymbol{K}(\boldsymbol{X}_i - \boldsymbol{X}_j)} \epsilon_{\boldsymbol{K}+\tilde{\boldsymbol{k}}} \tag{1.15}$$

The hopping amplitude t, the self-energy Σ can be separated into inter- and intra-cluster parts

$$[t_{c,DCA}]_{\boldsymbol{X}_i\boldsymbol{X}_j} = \frac{1}{N_c}\sum_{\boldsymbol{K}} e^{i\boldsymbol{K}(\boldsymbol{X}_i-\boldsymbol{X}_j)}\bar{\epsilon}_{\boldsymbol{K}} \tag{1.16}$$

$$[\delta t_{DCA}(\tilde{\boldsymbol{k}})]_{\boldsymbol{X}_i\boldsymbol{X}_j} = \frac{1}{N_c}\sum_{\boldsymbol{K}} e^{i\boldsymbol{K}(\boldsymbol{X}_i-\boldsymbol{X}_j)}\delta t(\boldsymbol{K}+\tilde{\boldsymbol{k}}) \tag{1.17}$$

where $\bar{\epsilon}_{\boldsymbol{K}} = \frac{N_c}{N}\sum_{\tilde{\boldsymbol{k}}}\epsilon_{\boldsymbol{K}+\tilde{\boldsymbol{k}}}$ and $\delta t(\boldsymbol{K}+\tilde{\boldsymbol{k}}) = \epsilon_{\boldsymbol{K}+\tilde{\boldsymbol{k}}} - \bar{\epsilon}_{\boldsymbol{K}}$.

Both the Green's function and self-energy are $N_c \times N_c$ diagonal matrices

$$G(\boldsymbol{K}+\tilde{\boldsymbol{k}},z) = g(\boldsymbol{K},z) + g(\boldsymbol{K},z)\delta t(\boldsymbol{K}+\tilde{\boldsymbol{k}})G(\boldsymbol{K}+\tilde{\boldsymbol{k}},z) = \frac{1}{g^{-1}(\boldsymbol{K},z) - \delta t(\boldsymbol{K}+\tilde{\boldsymbol{k}})}, \tag{1.18}$$

with

$$g(\boldsymbol{K},z) = [z - \bar{\epsilon}_{\boldsymbol{K}} + \mu - \Sigma_c(\boldsymbol{K},z)]^{-1} \tag{1.19}$$

μ is the chemical potential, z is the Matsubara frequency $i\omega_n$ and $g(\boldsymbol{K},z)$ is the Green's function of the cluster decoupled from the remainder of the system. The lattice Green's function is calculated by coarse-graining

$$\bar{G}(\boldsymbol{K},z) = \frac{N_c}{N}\sum_{\tilde{\boldsymbol{k}}} G(\boldsymbol{K}+\tilde{\boldsymbol{k}},z) \tag{1.20}$$

One concern about dynamical cluster approximation is the choice of cluster size and shape. A cluster should at least be big enough to (1) satisfy the lattice point group symmetry; (2) describe the symmetry of intended order parameter; (3) the number of neighbors in each near-neighbor shell of the clusters do not differ too greatly from those of the original lattice [89, 90]. Ref. [89] calculated the antiferromagnetic susceptibility using DCA and quantum Monte Carlo for Hubbard model with various cluster sizes. Their results show that the

Neel transition temperature decreases slowly with increasing cluster size, but off by a large amount when $N_c = 4$. This is understandable since when $N_c = 4$, each site in the lattice only has two neighboring sites instead of four neighboring sites. Ref. [90] discussed the influence of cluster size on Neel temprature, d-wave pair field susceptibility and density of states. The pseudogap is another topic under the spotlight. Ref. [91] investigated the pseudogap phenomenon by measuring the spectral function and self-energy at antinode point $\boldsymbol{k} = (0, \pi)$ (DCA and QMC). They found pseudogap only when $N_c > 1$ and gap size slightly increased as the cluster size becomes larger.

In this thesis, most results are produced with 8-site cluster, which is large enough to be representative of thermodynamic limit and also small enough for current computing ability to reach necessary accuracy. In chapter 2, we compare the anti-ferromagnetic phase boundary determined by 8-site cluster and two 16-site cluster with different configurations. In chapter 3, the correlated paring susceptibility calculated with 4-site, 8-site and 16-site cluster are plotted side-by-side. Both analysis show a qualitative agreement between 8 site and 16 site cluster.

1.4.4 Continuous Time Auxiliary Field Impurity Solver

The main part of the DMFT/DCA self-consistency loop is solving the cluster impurity The continuous-time auxiliary field impurity solver is based on the stochastic sampling of quantum and thermal averages, i.e. quantum Monte Carlo technique.

The example used in this section is a single impurity problem which can be mapped from a one-band Hubbard model using DMFT. It can be easily extended to multiple-band and multiple-sites cluster problem. This section closely follows the review of Ref. [92]. The Hamiltonian of the impurity problem can be separated into two parts, $H = H_0 + V$, where

$$H_0 = -(\mu - \frac{U}{2})(n_\uparrow + n_\downarrow) + \sum_{\sigma,\boldsymbol{k}}(t_{\sigma,k}c_\sigma^\dagger a_k + h.c.) + \sum_{\sigma,\boldsymbol{k}} \epsilon_{\boldsymbol{k}} a_{\sigma,\boldsymbol{k}}^\dagger a_{\sigma,\boldsymbol{k}} \tag{1.21}$$

$$V = U(n_\uparrow n_\downarrow - (n_\uparrow + n_\downarrow)/2) \tag{1.22}$$

Here the chemical potential is shifted by $-U/2$ so that half-filling is at $\mu = 0$. H_0 is the Gaussian term containing both the impurity and the bath degrees of freedom. To disentangle the $n_\uparrow n_\downarrow$ in the V term, we introduce a arbitrary positive constant K and a new varialble, the auxiliary Ising spin s [93]. The partition function can be expressed in an interaction representation,

$$Z = Tre^{-\beta H} = e^{-K} Tr\left[e^{-\beta H_0} T_\tau e^{-\int_0^\beta d\tau (V(\tau) - K/\beta)}\right] \tag{1.23}$$

expand it in powers of $K/\beta - V$, get

$$Z = \sum_n \int_0^\beta d\tau_1 \ldots \int_{\tau_{n-1}}^\beta (\frac{K}{\beta})^n Tr\left[e^{-(\beta-\tau_n)H_0} \times \left(1 - \frac{\beta V}{K}\right) \ldots e^{-(\tau_2 - \tau_1)H_0}\left(1 - \frac{\beta V}{K}\right) e^{-\tau_1 H_0}\right] \tag{1.24}$$

$$= \sum_n \sum_{s_i = \pm 1 1 \leqslant i \leqslant n} \int_0^\beta d\tau_1 \ldots \int_{\tau_{n-1}}^\beta d\tau_n \left(\frac{K}{2\beta}\right)^n Z_n(\{s_i, \tau_i\}) \tag{1.25}$$

where

$$Z_n(\{s_i, \tau_i\}) \equiv Tr \prod_{i=n}^{1} exp(-\delta\tau_i H_0) \exp(s_i \gamma(n_\uparrow - n_\downarrow)) \tag{1.26}$$

and $\delta\tau \equiv \tau_{i+1} - \tau_i$ for $i < n$ and $\delta\tau_n \equiv \beta - \tau_n + \tau_1$. Equation 1.24 makes use of the relation

$$1-\frac{\beta V}{K}=\frac{1}{2}\sum_{s=\pm 1}e^{\gamma s(n_\uparrow - n_\downarrow)} \tag{1.27}$$

$$\cosh(\gamma)=1+\frac{\beta U}{2K} \tag{1.28}$$

In this way, the interaction term is decoupled with the price of expanded configuration space. $\left(\frac{K}{2\beta}\right)^n Z_n(\{s_i,\tau_i\})$ acts as the "weight" for a specific configuration $\{s_i,\tau_i\}$ in the Quantum Monte Carlo procedure. Unlike classical Monte Carlo, it can be negative, causing the infamous sign problem. As shown in Fig. 1.9, there's no sign problem at half-filling. As U increases, sign problem quickly becomes severe, especially at large doping. The core element of configuration weight, $Z_n(\{s_i,\tau_i\})$, can be expressed as

$$\frac{Z_n(\{s_i,\tau_i\})}{Z_0}=\prod_{\sigma=\uparrow,\downarrow} detN_\sigma^{-1}(\{s_i,\tau_i\}), \tag{1.29}$$

$$N_\sigma^{-1}(\{s_i,\tau_i\})\equiv e^{V_\sigma^{\{s_i\}}}-G_{0\sigma}^{\{tau_i\}}\left(e^{V_\sigma^{\{s_i\}}}-1\right), \tag{1.30}$$

$$e^{V_\sigma^{\{s_i\}}}\equiv diag\left(e^{\gamma(-1)^\sigma s_1},\ldots,e^{\gamma(-1)^\sigma s_n}\right), \tag{1.31}$$

where $(-1)^\uparrow \equiv 1$,$(-1)^\downarrow \equiv -1$ and $(G_{0\sigma}^{\{\tau_i\}})_{i,j}=g_{0\sigma}(\tau_i-\tau_j)$ for $i\neq j$, $(G_{0\sigma}^{\{tau_i\}})_{i,i}=g_{0\sigma}(0^+)$. $g_{0\sigma}(\tau)$ is the input of the impurity solver, the bare Green's function.

The sampling of configurations needs to satisfy the detailed balance condition to yield right probability distribution p. With the Metropolis algorithm, the transition probability between two configurations is separated into a propose part and an acceptance part. For example, the probability of proposing to insert a auxiliary spin at a random time with a random direction is $p^{prop}(n\rightarrow n+1)=1/2(d\tau/\beta))$ and to remove a random auxiliary spin is $p^{prop}(n+1\rightarrow n)=1/(n+1)$.

$$\frac{p(n\rightarrow n+1)}{p(n+1\rightarrow n)}=\frac{K}{n+1}\prod_{\sigma=\uparrow\downarrow}\frac{det(N_\sigma^{(n+1)})^{-1}}{det(N_\sigma^{n})^{-1}} \tag{1.32}$$

The change of configuration $x \to y$ is accepted according to

$$W_{acc}(x \to y)\min(1, \frac{p(x)}{p(y)}) \tag{1.33}$$

In each updating step, it is not necessary to calculate the value of $det(N_\sigma^n)^{-1}$, only the ratio between two determinant of slightly differed matrices is needed. This can be accomplished efficiently with the sub-matrix updates algorithm proposed by E.Gull[94].

The main observable is the one-particle Green's function and two-particle Green's function. The one-particle Green's function is measured according to Eq. 1.34. Eq. 1.35 is used to measure two-frequency Green's function, which is a middle step to calculate two-particle Green's function.

$$G(i\omega_n) = g_0(k, i\omega_n) - \frac{g_0(i\omega_n)^2}{\beta}\sum_{pq} e^{i\omega_n\tau_p} M_{pq} e^{-i\omega_n\tau_q} \tag{1.34}$$

$$G(i\omega_n, i\omega_m) = \delta_{mn} g_0(i\omega_n) - \frac{1}{\beta} g_0(i\omega_n) g_0(i\omega_m) \sum_{pq} e^{i\omega_n\tau_p} M_{pq} e^{-i\omega_m\tau_q} \tag{1.35}$$

where matrix M is $M_{pq} = [(e^{V_\sigma^{\{s_i\}}} - 1)N_\sigma(\{s_i, \tau_i\})]_{pq}$. These equations for measurement can also be extended to cluster impurity problem.

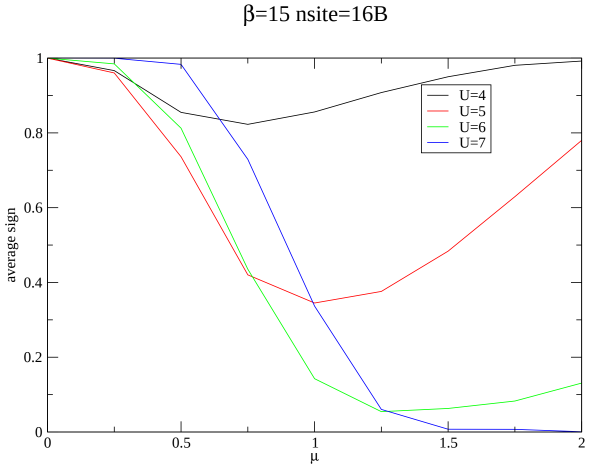

Figure 1.9: Average sign at $\beta = 15/t$, $t' = 0.1$ using 16-site cluster with continuous time auxiliary field solver.

1.4.5 Analytical Continuation

The outputs of CTAUX impurity solver and many other solvers are quantities computed in an imaginary time statistical mechanics formalism. We sometimes need to interpret imaginary time (Matsubara frequency) Green's functions and correlation functions as spectral functions and response functions on the real axis. This analytical continuation procedure is ill-conditioned in the sense that small fluctuation in the input data lead to large fluctuation in the output data. The standard method of solving this problem is the maximum entropy method (MaxEnt).

Here we introduce the basic formalism MaxEnt, following Ref. [95] and Ref. [96]. The Green's function on the imaginary frequency axis is connected to the Green's function on imaginary time access through a Fourier transform

$$G(i\omega_n) = \int_0^\beta e^{i\omega_n \tau} G(\tau), \tag{1.36}$$

where $i\omega_n$ is the Matsubara frequency. $i\omega_n = 2\pi(n + \frac{1}{2})/\beta$ for fermionic operators and $i\omega_n = 2\pi n/\beta$ for bosonic operators. In a Quantum Monte Carlo simulation, the Green's function $G(\tau)$ is not known to arbitrary precision and at arbitrary τ. Rather, we estimate each discrete point $G(\tau_n)$ by averaging a set of M samples. The estimated $G(\tau_n)$ is given by

$$G(\tau_n) = \frac{1}{M}\sum_{j=1}^{M} G(\tau_n)^{(j)}, \tag{1.37}$$

where $G(\tau_n)^{(j)}$ is the j-th measurement of $G(\tau_n)$. In the case of fermions, the real frequency Green's function are related to the imaginary time Green's function and Matsubara frequency Green's function as

$$G(i\omega_n) = -\frac{1}{\pi}\int_{-\infty}^{\infty} \frac{d\omega \mathrm{Im}[G(\omega)]}{i\omega_n - \omega} \tag{1.38}$$

$$G(\tau_n) = \frac{1}{\pi}\int_{-\infty}^{\infty} \frac{d\omega \mathrm{Im}[G(\omega)] e^{-\tau_n \omega}}{1 + e^{-\beta\omega}} \tag{1.39}$$

where τ_n is one point of $G(\tau)$, whose imaginary time range has been discretized into N points in some manner. We can obtain the spectral function $A(\omega)$ from the imaginary part of the Green's function on the real frequency axis

$$A(\omega) = -\frac{1}{\pi}\mathrm{Im}[G(\omega)]. \tag{1.40}$$

Eq. 1.39 can be written into the form

$$G(\tau_n) = \int_{-\infty}^{\infty} d\omega A(\omega) K_n(\omega), \tag{1.41}$$

where $K_n(\omega) = -\frac{e^{-\tau_n\omega}}{1+e^{-\omega\beta}}$ is called the 'kernel' of the analytical continuation. Here we present the kernel for transformation from fermionic imaginary time Green's function to fermionic real frequency Green's function. Kernels for other transformation can be found in Ref. [96].

What we tries to find with analytical continuation is a spectral function whose estimated imaginary axis Green's function $\bar{G}(\tau)$ is most close to the $G(\tau_n)$ we obtained from Monte Carlo simulations. Therefore, we define the ”goodness of fit” χ^2 as

$$\chi^2 = \sum_{n,m}^{M} (\bar{G}(\tau_n) - G(\tau_n))^* C_{nm}^{-1} (\bar{G}(\tau_m) - G(\tau_m)) \tag{1.42}$$

where C_{nm} is the covariance matrix, encapsulating the correlation between Green's function measurents.

$$C_{nm} = \frac{1}{M(M-1)} \sum_{j=1}^{M} (G_n - G_n^{(j)})(G_m - G_m^{(j)}) \tag{1.43}$$

The most straight-forward procedure to solve for $G(\omega)$ using Eq. 1.41 is $A = K^{-1}GK$. However, the condition number of matrix K is usually very large and this problem is ill-conditioned. That is to say, there are many solutions of A that satisfy $G = KA$ within the uncertainty of G.

In the MaxEnt, additional criteria is imposed on A to help regularize the solution. The quantity to be minimized is

$$Q = \frac{1}{2}\chi^2 - \alpha S[A] \tag{1.44}$$

The ”entropy” term $S[A]$ describes the likeliness of A to a reference spectral function.

$$S[A] = -\int d\omega A(\omega) \ln \left[\frac{A(\omega)}{d(\omega)} \right]. \tag{1.45}$$

α is a Lagrange multiplier that controls the competition between χ^2 and S.

CHAPTER 2

Two-particle vertices Response Functions

2.1 Overview

This chapter presents the numerical study of the two-particle response functions in high T_c cuprate superconductors. Sec. 2.2 introduces the background. Sec. 2.3 and Sec. 2.5 provides the formula of calculating two-particle quantities. Sec. 2.4 presents my derivation of superconducting susceptibility using linear response theory. In Sec. 2.6 and Sec, 2.7 show results for the magnetic channel and the superconducting.

2.2 Introduction

The static and single-particle properties of Hubbard model, such as the Green's function, self-energy, spectral function and double occupancy, have been intensively studied hitherto. Yet not much has been accomplished on two-particle properties, whose numerical measurement is time-consuming and sometimes memory-demanding. The workload of obtaining complete two particle frequency and momentum dependent Green's function, $G_{\sigma\sigma'}(\boldsymbol{k}\boldsymbol{k}'\boldsymbol{q}, \omega\omega'\nu)$ increases as $N_c^3\beta^3 N_\omega^3$, where N_c is the number of momentum, N_ω^3 is the number of fermionic Matsubara frequencies and β the inverse temperature. And the requirement for memory and storage space increases as $N_c^3 N_\omega^3$. However, there are plenty of reasons that we should nevertheless attempt to have an accurate, systematic calculation of two particle correlation functions and vertex functions.

First of all, most of the comparison between numerical results and experimental results are performed for one-particle quantities, such as electronic spectral function and APRES [97], while theoretical analysis of a much wider range of experimental techniques including optical conductivity [98], Raman spectroscopy [99], muon-spin relaxation [100] and inelastic neutron scattering [101] requires a vertex function calculation. For very limited situations, such as analyzing optical and thermal conductivity, it may be sufficing to use bare susceptibility $\chi_0 = GG$ so that one-particle level measurement is enough [102, 103, 104]. But for most two-particle level experiments, an actual two-particle calculation is inevitable. In chapter 4 and 5 we show simulation results and detailed explanation of nuclear magnetic resonance (NMR) experiment where vertex corrections are crucial.

Secondly, the calculation of momentum and frequency dependent reducible and irreducible vertex functions are important in diagrammatic DMFT extensions. The dual fermion method [105, 38], the one particle irreducible approach [106], the dynamical vertex approximation [86] and the recently develped DMF^{2}RG method [107] depend on the measurement on two-particle level. These are DMFT extensions that take into account longer range fluctuations.

Thirdly, the investigation of (quantum) phase transition can be performed in disordered state by observing the divergence of static susceptibility as a function of external control parameters.

Last but not the least, the two-particle quantities can be used for the self-energy decomposition, the so-called fluctuation diagnostics [108]. While self-energy describes all scattering effects of one added/removed electron, it lacks the detail of the origination of these effects. One can use the Dyson-Schwinger equation of motion to connects self-energy to the full vertex function and decompose it into different channels. With the knowledge of contribution to self-energy from each channel, momentum and frequency, information about the role of different fluctuation can be obtained. Chapter 5 provides the formula for equation of motion within Nambu formalism.

Attempts have been made to calculate the two-particle quantities. One can assume that the irreducible vertex $\Gamma(K, K', Q)$ is only weakly dependent on K and K' to circumvent the numerical complexity [109]. Unfortunately, this assumption will fail at low temperature and large interaction. Two particle correlations analysis using functional renormalization group scheme wasfound to be limited to the one-particle irreducible vertex while higher order vertex part are nontrivial [110].

Recent development in the numerical simulation of interacting fermionic lattice models have made exact calculation of two particle quantities possible. Equations in this chapter follows Ref. [11] but have been extended to cluster approximation. Some calculations in this framework have been performed in recent years. A recently developed DCA+ method was combined with Bethe-Salpeter equation to analyze the leading eigenvalue of $\Gamma\chi_0$ matrix to get superconducting transition temperature of Hubbard model at weak and intermediate coupling with different cluster sizes [111]. Analysis of the Hubbard-Holstein model[112] has also been performed. Getting results with very large cluster size was made possible by focusing on static spin susceptibility, but was limited to very weak interaction [113].

In this chapter, we derive the Bethe-Salpeter equation within DCA, and the linear response theory for filtering out the channel of susceptibility of interest. We will show aspect of the phase diagram of 2D Hubbard model within the DCA approximation by examining the divergence of the susceptibility, which includes the phase boundaries for AFM, d-wave superconductivity.

2.3 Two Particle Vertex Functions

In this section the calculation of dynamical susceptibility using dynamical cluster approximation is illustrated. The notation and calculation of this section closely follows the Ref. [11] and Ref. [43]. We start by defining the one-particle and two-particle Green's functions in imaginary time τ as

$$G_\sigma(\boldsymbol{r}_1\tau_1, \boldsymbol{r}_2\tau_2) = \langle T_\tau(c^\dagger_{\boldsymbol{r}_1\sigma_1}(\tau_1)c_{\boldsymbol{r}_2\sigma_2}(\tau_2)\rangle \tag{2.1}$$

$$G_{2,\sigma_1\sigma_2\sigma_3\sigma_4}(\boldsymbol{r}_1\tau_1, ..., \boldsymbol{r}_4\tau_4) = \langle T_\tau(c^\dagger_{\boldsymbol{r}_1\sigma_1}(\tau_1)c_{\boldsymbol{r}_2\sigma_2}(\tau_2)c^\dagger_{\boldsymbol{r}_3\sigma_3}(\tau_3)c_{\boldsymbol{r}_4\sigma_4}(\tau_4)\rangle. \tag{2.2}$$

The generalized susceptibility can be written in imaginary time τ, in terms of the one- and two-particle Green's functions as [11]

$$\begin{aligned}\chi_{\sigma_1\sigma_2\sigma_3\sigma_4}(\boldsymbol{r}_1\tau_1, \boldsymbol{r}_2\tau_2, \boldsymbol{r}_3\tau_3, \boldsymbol{r}_4\tau_4) = {} & G_{2,\sigma_1\ldots\sigma_4}(\boldsymbol{r}_1\tau_1, \boldsymbol{r}_2\tau_2, \boldsymbol{r}_3\tau_3, \boldsymbol{r}_4\tau_4) \\ & - G_{\sigma_1\sigma_2}(\boldsymbol{r}_1\tau_1, \boldsymbol{r}_2\tau_2)G_{\sigma_3\sigma_4}(\boldsymbol{r}_3\tau_3, \boldsymbol{r}_4\tau_4).\end{aligned} \tag{2.3}$$

The susceptibility can be represented in frequency space via the Fourier transform. In the particle-particle (pp) convention, it is defined as

$$\begin{aligned}\chi^{\omega\omega'\nu}_{pp\sigma\sigma'}(\boldsymbol{k}, \boldsymbol{k}', \boldsymbol{q}) = {} & \int_0^\beta \int_0^\beta \int_0^\beta d\tau_1 d\tau_2 d\tau_3 \chi_{\sigma\sigma\sigma'\sigma'}(\boldsymbol{r}_1\tau_1, \boldsymbol{r}_2\tau_2, \boldsymbol{r}_3\tau_3, \boldsymbol{0}0) \\ & \times e^{-i\omega\tau_1} e^{i(\nu-\omega')\tau_2} e^{-i(\nu-\omega)\tau_3} \times e^{-i\boldsymbol{k}\boldsymbol{r}_1} e^{i(\boldsymbol{q}-\boldsymbol{k}')\boldsymbol{r}_2} e^{-i(\boldsymbol{q}-\boldsymbol{k})\boldsymbol{r}_3}\end{aligned} \tag{2.4}$$

In the particle-hole (ph) convention, it is defined as

$$\begin{aligned}\chi^{\omega\omega'\nu}_{ph\sigma\sigma'}(\boldsymbol{k}, \boldsymbol{k}', \boldsymbol{q}) = {} & \int_0^\beta \int_0^\beta \int_0^\beta d\tau_1 d\tau_2 d\tau_3 \chi_{\sigma\sigma\sigma'\sigma'}(\boldsymbol{r}_1\tau_1, \boldsymbol{r}_2\tau_2, \boldsymbol{r}_3\tau_3, \boldsymbol{0}0) \\ & \times e^{-i\omega\tau_1} e^{i(\nu+\omega)\tau_2} e^{-i(\nu+\omega')\tau_3} \times e^{-i\boldsymbol{k}\boldsymbol{r}_1} e^{i(\boldsymbol{q}+\boldsymbol{k})\boldsymbol{r}_2} e^{-i(\boldsymbol{q}+\boldsymbol{k}')\boldsymbol{r}_3}\end{aligned} \tag{2.5}$$

where ω and ω' are fermionic Matsubara frequencies, ν is a bosonic Matsubara frequency, σ and σ' are spin labels and k, k' and q are initial, final and transfer momenta respectively. For simplicity, we will use $k = (\boldsymbol{k}, \omega)$ and $q = (\boldsymbol{q}, \nu)$. The pp and ph channel are connected to each other as

$$\begin{aligned}\chi_{pp}(k,k',q) &= \chi_{ph}(k,k',q-k-k') \\ \chi_{ph}(k,k',q) &= \chi_{pp}(k,k',(k+k'+q))\end{aligned} \tag{2.6}$$

When the system is in paramagnetic state, there are only three independent spin combination. We will simplify their notation as $\sigma\sigma\sigma'\sigma' \rightarrow \sigma\sigma'$,$\sigma\sigma\sigma\sigma \rightarrow \sigma\sigma$ and $\sigma\sigma'\sigma'\sigma \rightarrow \overline{\sigma\sigma'}$ The susceptibility can be separated into two parts, the “bare” susceptibility(the bubble term) and the vertex contribution.

$$\begin{aligned}\chi_{ph\sigma\sigma'}(k,k',q) = &-\beta N G_\sigma(k)G_\sigma(k+q)\delta_{kk'}\delta_{\sigma\sigma'} \\ &- G_\sigma(k)G_\sigma(k+q)K_{ph\sigma\sigma'}(k,k',q)G_{\sigma'}(k')G_{\sigma'}(k'+q)\end{aligned} \tag{2.7}$$

where N is the number of momenta or volume of momentum space in the continuous case, and K is the full vertex function. Note that while most papers use F to denote the full vertex function, we use K to avoid confusion with the anomalous Green’s function $F(\tau) = \langle Tc(\tau)c\rangle$.

The full vertex function consists of all types of interaction of a four-point function. It is the sum of all ”fully connected” two particle diagrams [11]. These diagrams are either fully irreducible or reducible in only one channel. The two-particle reducibility of one diagram means whether is can be divided into two parts by cutting two propogating lines. There are three channels (pp, ph, $\overline{ph}$), defined by how the four ”legs” of the two particle diagrams are seperated. Fig. 2.1 shows the decomposition of full vertex function, known as the parquet equation [114].

By defining the bare susceptibility as follows, we can write Eq. 2.7 as a compact matrix

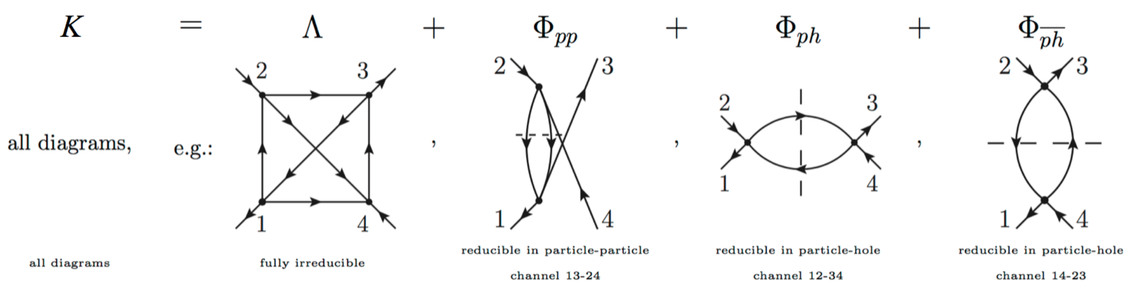

Figure 2.1: The decomposition of full vertex function. Figure taken from Ref. [11]

multiplication

$$\chi_{0ph}(k,k',q) = -\beta N G_\sigma(k) G_\sigma(k+q)\delta_{\sigma\sigma'}\delta_{kk'} \tag{2.8}$$

$$\chi_{0pp}(k,k',q) = -\beta N G_\sigma(k) G_\sigma(q-k')\delta_{\sigma\sigma'}\delta_{kk'} \tag{2.9}$$

$$\begin{aligned}\chi_{ph\sigma\sigma'}(k,k',q) = {} & \chi_0(k,k',q)\delta_{\sigma\sigma'} \\ & - \frac{1}{\beta^2 N^2}\sum_{k_1 k_2} \chi_0(k,k_1,q) K_{ph\sigma\sigma'}(k_1,k_2,q)\chi_0(k_2,k',q)\end{aligned} \tag{2.10}$$

The four independent channel are defined as density(d), magnetic(m), singlet(s) and triplet(t) channels

$$\begin{aligned} K_d &= K_{ph\uparrow\uparrow} + K_{ph\uparrow\downarrow} \quad & K_m &= K_{ph\uparrow\uparrow} - K_{ph\uparrow\downarrow} \\ K_s &= K_{pp\uparrow\downarrow} - K_{pp\overline{\uparrow\downarrow}} \quad & K_t &= K_{pp\uparrow\downarrow} + K_{pp\overline{\uparrow\downarrow}} \end{aligned} \tag{2.11}$$

We define the sum of all diagrams that are irreducible in r channel as Γ_r. As mentioned before, full vertex function can be decomposed into diagrams that are irreducible in one channel and diagrams that are reducible in this channel. K and Γ_r can be connected via two Green's function or anomalous Green's function lines, which is the Bethe-Salpeter equation

$$K = \Gamma_r + \int \Gamma_r GGK, \tag{2.12}$$

where the integral-symbol denotes an integration/summation over all internal degrees of freedom. In the ph and ph channels defined above, the Bethe-Salpeter equations are

$$\begin{aligned}
K_{ph\uparrow\uparrow}(k,k',q) &= \Gamma_{ph\uparrow\uparrow}(k,k',q) \\
&\quad + \frac{1}{\beta N}\sum_{k_1\sigma_1}\Gamma_{ph\uparrow\sigma_1}(k,k_1,q)G(k_1)G(k_1+q)K_{ph\sigma_1\uparrow}(k_1,k',q) \\
K_{ph\uparrow\downarrow}(k,k',q) &= \Gamma_{ph\uparrow\downarrow}(k,k',q) \\
&\quad + \frac{1}{\beta N}\sum_{k_1\sigma_1}\Gamma_{ph\uparrow\sigma_1}(k,k_1,q)G(k_1)G(k_1+q)K_{ph\sigma_1\downarrow}(k_1,k',q) \\
K_{pp\uparrow\downarrow}(k,k',q) &= \Gamma_{pp\uparrow\downarrow}(k,k',q) \\
&\quad - \frac{1}{2\beta N}\sum_{k_1\sigma_1}\Gamma_{pp\sigma_1(-\sigma_1)\uparrow\downarrow}(k,k_1,q)G(k_1)G(q-k_1)K_{pp\uparrow\downarrow\sigma_1(-\sigma_1)}(k,q-k_1,q) \\
K_{pp\overline{\uparrow\downarrow}}(k,k',q) &= \Gamma_{pp\overline{\uparrow\downarrow}}(k,k',q) \\
&\quad - \frac{1}{2\beta N}\sum_{k_1\sigma_1}\Gamma_{pp\sigma_1(-\sigma_1)\downarrow\uparrow}(k,k_1,q)G(k_1)G(q-k_1)K_{pp\uparrow\downarrow\sigma_1(-\sigma_1)}(k,q-k_1,q)
\end{aligned} \tag{2.13}$$

Combining the channel definition (Eq. 2.11) and Eq. 2.13, we can get four decoupled channels

$$K_d(k,k',q) = \Gamma_d(k,k',q) + \frac{1}{\beta N}\sum_{k_1}\Gamma_d(k,k_1,q)G(k_1)G(k_1+q)K_d(k_1,k',q) \tag{2.14}$$

$$K_m(k,k',q) = \Gamma_m(k,k',q) + \frac{1}{\beta N}\sum_{k_1}\Gamma_m(k,k_1,q)G(k_1)G(k_1+q)K_m(k_1,k',q) \tag{2.15}$$

$$K_s(k,k',q) = \Gamma_s(k,k',q) + \frac{1}{\beta N}\sum_{k_1}\Gamma_s(k_1,k',q)G(k_1)G(q-k_1)K_s(k,q-k_1,q) \tag{2.16}$$

$$K_t(k,k',q) = \Gamma_t(k,k',q) + \frac{1}{\beta N}\sum_{k_1}\Gamma_t(k_1,k',q)G(k_1)G(q-k_1)K_t(k,q-k_1,q) \tag{2.17}$$

Eq. 2.14 combined with Eq. 2.7 yields the Belthe-Salpeter equation for general susceptibility in the matrix multiplication form

$$\begin{aligned}
\chi_{d,m}(k,k',q) &= \chi_{0,ph}(k,k',q) - \frac{1}{\beta^2N^2}\sum_{k_1,k_2}\chi_{0,ph}(k,k_1,q)\Gamma_{d,m}(k_1,k_2,q)\chi_{d,m}(k_2,k',q)\\
\chi_s(k,k',q) &= -\chi_{0,pp}(k,k',q) - \frac{1}{2\beta^2N^2}\sum_{k_1,k_2}(\chi_{0,pp}(k,k_1,q)-\chi_s(k,k_1,q))\Gamma_s(k_1,k_2,q)\chi_{0,pp}(k_2,k',q)\\
\chi_t(k,k',q) &= \chi_{0,pp}(k,k',q) - \frac{1}{2\beta^2N^2}\sum_{k_1,k_2}(\chi_{0,pp}(k,k_1,q)+\chi_t(k,k_1,q))\Gamma_t(k_1,k_2,q)\chi_{0,pp}(k_2,k',q)
\end{aligned} \tag{2.18}$$

Fig. 2.2 shows the feature of full vertex functions in different channels at momentum $\boldsymbol{Q} = (0,0)$, $\boldsymbol{Q} = (\pi,\pi)$ and $\boldsymbol{Q} = (0,\pi)$.

2.4 Linear Response Theory

There are many cases in which we are interested in the change of a system, where the system was initially in thermodynamic equilibrium, induced by a small applied external field or force. For example, one can calculate the dynamical susceptibility, when we are interested in the response at some other point $\boldsymbol{r}'$ at some later time t'. We can also obtain

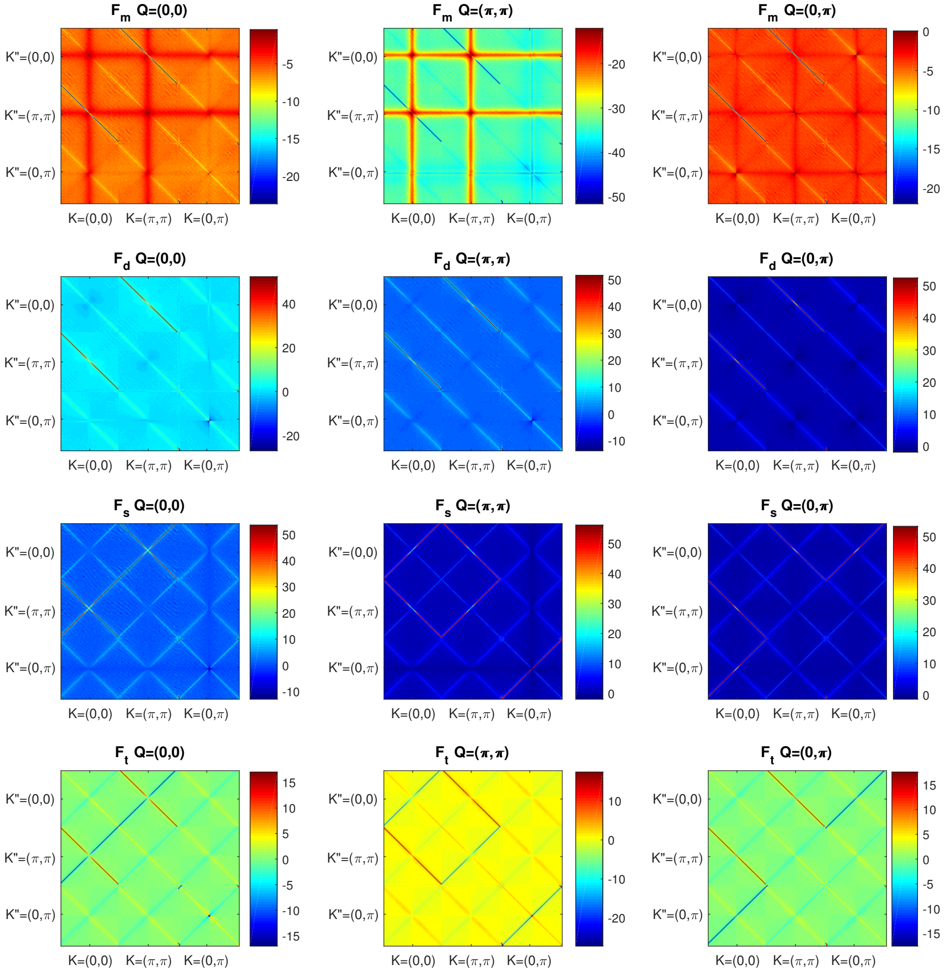

Figure 2.2: full vertex functions in different channels at momentum $Q = (0, 0)$, $Q = (\pi, \pi)$ and $Q = (0, \pi)$.

the global response of the system to an uniform perturbation.

The linear response theory for quantum manybody system has been provided by Baym and Kadanoff over a half century ago[115]. For the calculation of dynamical spin susceptibility, one can follow their paper which uses the expectation value of density is the response to an external field. Other types of external field and responses can follow their derivation.

In this section, we study the response of a system to small external superconducting field with certain symmetry. Here I present my derivation of the superconducting susceptibility by calculating the response of superconducting order parameter, i.e., anomalous Green's function under the external disturbance.

To study superconductivity, we employ the Nambu formalism. We define the Nambu spinor [116] as

$$\Psi^{\dagger}(\boldsymbol{k}_1,\tau_1) = (c^{\dagger}_{\boldsymbol{k}_1\uparrow}(\tau_1), c_{-\boldsymbol{k}_1\downarrow}(\tau_1)) \tag{2.19}$$

$$\Psi(\boldsymbol{k}_1,\tau_1) = (\Psi(\boldsymbol{k}_1,\tau_1)^{\dagger})^{\dagger} = \begin{pmatrix} c_{\boldsymbol{k}_1\uparrow}(\tau_1) \\ c^{\dagger}_{-\boldsymbol{k}_1\downarrow}(\tau_1) \end{pmatrix} \tag{2.20}$$

The external field adds a source term to the Hamiltonian[43]:

$$\begin{aligned} H' &= \sum_{\boldsymbol{k}_2} \Psi^{\dagger}(\boldsymbol{k}_2,\tau_2)\eta(\boldsymbol{k}_2,\tau_2)\sigma_x\Psi(\boldsymbol{k}_2,\tau_2) \\ &= \sum_{\boldsymbol{k}_2} \left(c_{-\boldsymbol{k}_2\downarrow}(\tau_2)c_{\boldsymbol{k}_2\uparrow}(\tau_2) + c^{\dagger}_{\boldsymbol{k}_2\uparrow}(\tau_2)c^{\dagger}_{-\boldsymbol{k}_2\downarrow}(\tau_2)\right)\eta(\boldsymbol{k}_2,\tau_2) \end{aligned} \tag{2.21}$$

where σ_x is the Pauli Matrix $\begin{pmatrix} 0 & 1 \\ 1 & 0 \end{pmatrix}$

For convenience, we omit τ in annihilation and creation operators for a while. $c_{\pm\boldsymbol{k}_i\sigma}$ means $c_{\pm\boldsymbol{k}_i\sigma}(\tau_i)$

The Green's function in the presence of the source term $\eta(\boldsymbol{k}_2,\tau_2)$ is[117]

$$G(\boldsymbol{k}_1,\tau_1,\boldsymbol{k}'_1,\tau'_1;\eta) = \langle[\Psi(\boldsymbol{k}_1,\tau_1)\Psi^{\dagger}(\boldsymbol{k}'_1,\tau'_1]\rangle_{\eta} = \frac{Tr\{e^{-\beta H}T_{\tau}[S\Psi(\boldsymbol{k}_1,\tau_1)\Psi^{\dagger}(\boldsymbol{k}'_1,\tau'_1)]\}}{Tr(e^{-\beta H}T_{\tau}S)} \tag{2.22}$$

where H is the original Hamiltonian without a source field and

$$S = \exp[-\int_0^{\beta} d\tau_2 \sum_{\boldsymbol{k}_2} \left(c_{-\boldsymbol{k}_2\downarrow}c_{\boldsymbol{k}_2\uparrow} + c^{\dagger}_{k_2\uparrow}c^{\dagger}_{-k_2\downarrow}\right)\eta(\boldsymbol{k}_2,\tau_2)] \tag{2.23}$$

In the numerator of Eq. 2.22, $\Psi(\boldsymbol{k}_1,\tau_1)\Psi^{\dagger}(\boldsymbol{k}'_1,\tau'_1)$ is a matrix. We operate in a formalism which allows for a non-zero anomalous Green's function, in the superconducting state which is defined as

$$F(\boldsymbol{k},\tau) = -\langle T_\tau c_{\boldsymbol{k}\uparrow}(\tau) c_{-\boldsymbol{k}\downarrow}(0)\rangle. \tag{2.24}$$

Since we use this anomalous Green's function as order parameter for superconductivity, consider the matrix element $c_{\boldsymbol{k}_1\uparrow} c_{-\boldsymbol{k}'_1\downarrow}$ in Eq. 2.22

$$F(\boldsymbol{k}_1,\tau_1,\boldsymbol{k}'_1,\tau'_1;\eta) = \frac{Tr[e^{-\beta H} T_\tau (S c_{\boldsymbol{k}_1\uparrow} c_{-\boldsymbol{k}'_1\downarrow})]}{Tr(e^{-\beta H} T_\tau S)} = \frac{N}{D} \tag{2.25}$$

where N means numerator and D means demoninator.

$$\frac{\delta F(\boldsymbol{k}_1,\tau_1,\boldsymbol{k}'_1,\tau'_1;\eta)}{\delta\eta(\boldsymbol{k}_2,\tau_2)} = \frac{\delta N}{\delta\eta(\boldsymbol{k}_2,\tau_2)}\frac{1}{D} - \frac{N}{D^2} \times \frac{\delta D}{\delta\eta(\boldsymbol{k}_2,\tau_2)} \tag{2.26}$$

$$\begin{aligned}\frac{\delta N}{\delta\eta(\boldsymbol{k}_2,\tau_2)} &= Tr\{e^{-\beta H} T_\tau [\frac{\delta S}{\delta\eta(\boldsymbol{k}_2,\tau_2)} c_{\boldsymbol{k}_1\uparrow} c_{-\boldsymbol{k}'_1\downarrow}]\} \\ &= Tr\{e^{-\beta H} T_\tau [-S \times (c_{-\boldsymbol{k}_2\downarrow} c_{\boldsymbol{k}_2\uparrow} + c^\dagger_{\boldsymbol{k}_2\uparrow} c^\dagger_{-\boldsymbol{k}_2\downarrow}) c_{\boldsymbol{k}_1\uparrow} c_{-\boldsymbol{k}'_1\downarrow}]\}\end{aligned} \tag{2.27}$$

$$\frac{\delta D}{\delta\eta(\boldsymbol{k}_2,\tau_2)} = Tr(e^{-\beta H} T_\tau \frac{\delta S}{\delta\eta(\boldsymbol{k}_2,\tau_2)}) = Tr\{e^{-\beta H} T_\tau [-S \times (c_{-\boldsymbol{k}_2\downarrow} c_{\boldsymbol{k}_2\uparrow} + c^\dagger_{\boldsymbol{k}_2\uparrow} c^\dagger_{-\boldsymbol{k}_2\downarrow})]\} \tag{2.28}$$

$$\frac{\delta S}{\delta\eta(\boldsymbol{k}_2,\tau_2)} = -S \times (c_{-\boldsymbol{k}_2\downarrow} c_{\boldsymbol{k}_2\uparrow} + c^\dagger_{\boldsymbol{k}_2\uparrow} c^\dagger_{-\boldsymbol{k}_2\downarrow}) \tag{2.29}$$

When $\eta = 0$,S=1, put it all together

$$\left.\frac{\delta F(\boldsymbol{k}_1,\tau_1,\boldsymbol{k}'_1,\tau'_1;\eta)}{\delta\eta(\boldsymbol{k}_2,\tau_2)}\right|_{\eta=0} = -\langle (c_{-\boldsymbol{k}_2\downarrow} c_{\boldsymbol{k}_2\uparrow} + c^\dagger_{\boldsymbol{k}_2\uparrow} c^\dagger_{-\boldsymbol{k}_2\downarrow}) c_{\boldsymbol{k}_1\uparrow} c_{-\boldsymbol{k}'_1\downarrow}\rangle + F(1,1')\langle (c_{-\boldsymbol{k}_2\downarrow} c_{\boldsymbol{k}_2\uparrow} + c^\dagger_{\boldsymbol{k}_2\uparrow} c^\dagger_{-\boldsymbol{k}_2\downarrow})\rangle$$

Outside of the superconducting region, $F(\boldsymbol{k}_1,\tau_1,\boldsymbol{k}'_1,\tau'_1) = 0$, and $\langle c_{-\boldsymbol{k}_2\downarrow} c_{\boldsymbol{k}_2\uparrow} c_{\boldsymbol{k}_1\uparrow} c_{-\boldsymbol{k}'_1\downarrow}\rangle = 0$

$$\left.\frac{\delta F(\boldsymbol{k}_1,\tau_1,\boldsymbol{k}_1',\tau_1')}{\delta\eta(\boldsymbol{k}_2,\tau_2)}\right|_{\eta=0} = \langle c^\dagger_{\boldsymbol{k}_2\uparrow} c_{-\boldsymbol{k}_1'\downarrow} c^\dagger_{-\boldsymbol{k}_2\downarrow} c_{\boldsymbol{k}_1\uparrow}\rangle \tag{2.30}$$

Set $\boldsymbol{k}_2 = \boldsymbol{k}$,$\boldsymbol{k}_1 = \boldsymbol{k}_1' = \boldsymbol{k}'$

$$\left.\frac{\delta F(\boldsymbol{k}',\tau_1')}{\delta\eta(\boldsymbol{k}_2,\tau_2)}\right|_{\eta=0} = \langle c^\dagger_{\boldsymbol{k}\uparrow}(\tau_2) c_{-\boldsymbol{k}'\downarrow}(\tau_1') c^\dagger_{-\boldsymbol{k}\downarrow}(\tau_2) c_{k'\uparrow}(\tau_1)\rangle \tag{2.31}$$

There are only one momentum and one imaginary time dependence, because with time translational invariance, we can do the variable substitution $\tau_2 \leftarrow \tau_2 - \tau_1$, $\tau_1' \leftarrow \tau_1' - \tau_1$ According to [11]

$$\begin{aligned}\chi_{pp\overline{\uparrow\downarrow}}(\boldsymbol{k}\tau_2,-\boldsymbol{k}'\tau_1',-\boldsymbol{k}\tau_2,k'0) &= G_{2,\uparrow\downarrow\downarrow\uparrow}(\boldsymbol{k}\tau_2,-\boldsymbol{k}'\tau_1',-\boldsymbol{k}\tau_2,\boldsymbol{k}'0) - G_{\uparrow\downarrow}(\boldsymbol{k}\tau_2,-\boldsymbol{k}'\tau_1')G_{\downarrow\uparrow}(-\boldsymbol{k}\tau_2,k'0)\\ &= \langle c^\dagger_{\boldsymbol{k}\uparrow}(\tau_2) c_{-\boldsymbol{k}'\downarrow}(\tau_1') c^\dagger_{-\boldsymbol{k}\downarrow}(\tau_2) c_{\boldsymbol{k}'\uparrow}(0)\rangle\end{aligned} \tag{2.32}$$

where $G_{\uparrow\downarrow} = G_{\downarrow\uparrow} = 0$ due to spin-conservation.

Do a inverse Fourier transform for equation(7b) in [11]

$$\begin{aligned}&\chi_{pp\overline{\uparrow\downarrow}}(\boldsymbol{k}\tau_2,-\boldsymbol{k}'\tau_1',-\boldsymbol{k}\tau_2,\boldsymbol{k}'0)\\ &= \frac{1}{\beta^3N^3}\sum_{\omega\omega'\nu}\chi_{pp\overline{\uparrow\downarrow}}(\boldsymbol{k}\omega,-\boldsymbol{k}'(\nu-\omega'),-\boldsymbol{k}(\nu-\omega),\boldsymbol{k}'\omega')e^{i\omega\tau_2}e^{i(\nu-\omega')\tau_1'}e^{i(\nu-\omega)\tau_2}\end{aligned} \tag{2.33}$$

when $\tau_1' = 0$

$$\chi_{pp\overline{\uparrow\downarrow}}(\boldsymbol{k}\tau_2,-\boldsymbol{k}'0,-\boldsymbol{k}\tau_2,\boldsymbol{k}'0) = \frac{1}{\beta^3}\sum_{\omega\omega'\nu}\chi_{pp\overline{\uparrow\downarrow}}(\boldsymbol{k}\omega,-\boldsymbol{k}'(\nu-\omega'),-\boldsymbol{k}(\nu-\omega),\boldsymbol{k}'\omega')e^{i\nu\tau_2} \tag{2.34}$$

Integrating τ_2 over $(0, \beta)$, we get

$$\int_0^\beta d\tau_2 \chi_{pp\overline{\uparrow\downarrow}}(\boldsymbol{k}\tau_2, -\boldsymbol{k}'0, -\boldsymbol{k}\tau_2, \boldsymbol{k}'0) = \int_0^\beta d\tau_2 \frac{1}{\beta^3} \sum_{\omega\omega'\nu} \chi_{pp\overline{\uparrow\downarrow}}(\boldsymbol{k}\omega, -\boldsymbol{k}'(\nu-\omega'), -\boldsymbol{k}(\nu-\omega), \boldsymbol{k}'\omega')e^{i\nu\tau_2}$$
$$= \frac{1}{\beta^2} \sum_{\omega\omega'} \chi_{pp\overline{\uparrow\downarrow}}(\boldsymbol{k}\omega, -\boldsymbol{k}'(-\omega'), -\boldsymbol{k}(-\omega), \boldsymbol{k}'\omega') \tag{2.35}$$

$$\int_0^\beta d\tau \left.\frac{\delta F(\boldsymbol{k}', 0)}{\delta \eta(\boldsymbol{k}, \tau)}\right|_{\eta=0} = \frac{1}{\beta^2} \sum_{\omega\omega'} \chi_{pp\overline{\uparrow\downarrow}}^{\omega\omega'\nu=0}(\boldsymbol{k}, \boldsymbol{k}', \boldsymbol{q}=0) \tag{2.36}$$

Using the SU(2) and crossing symmetry of the general susceptibility. $\chi_{pp\overline{\uparrow\downarrow}}$ is the difference between the $\sigma\sigma' \equiv \uparrow\uparrow$ and $\uparrow\downarrow$ susceptibilities as

$$\chi_{pp\overline{\uparrow\downarrow}} = \chi_{pp\uparrow\uparrow} - \chi_{pp\uparrow\downarrow}. \tag{2.37}$$

We can sum over fermionic matsubara frequency and momentum to get static susceptibility with different symmetry.

$$\frac{1}{\beta^2 N^2} \sum_{\boldsymbol{k}\boldsymbol{k}'\omega\omega'} \chi_{pp\overline{\uparrow\downarrow}}^{\omega\omega'\nu=0}(\boldsymbol{k}, \boldsymbol{k}', \boldsymbol{q}=0) g(\boldsymbol{k}) g(\boldsymbol{k}') = \frac{1}{N^2} \int_0^\beta d\tau' \sum_{\boldsymbol{k}\boldsymbol{k}'} \left.\frac{\delta F(\boldsymbol{k}, \tau=0; \eta)}{\delta \eta(\boldsymbol{k}', \tau')} g(\boldsymbol{k}) g(\boldsymbol{k}')\right|_{\eta=0} \tag{2.38}$$

where η is the strength of an external superconducting field and $F(\boldsymbol{k}, \tau; \eta)$ is the anomalous Green's function with the existence of an external field. $g(\boldsymbol{k})$ is any symmetry function[118] and within DCA, the accessible $s-$, $p-$, d_{xy} or $d_{x^2-y^2}$ symmetries are enforced by including symmetry factors $g(\boldsymbol{K})g(\boldsymbol{K}')$ while summing over all initial $\boldsymbol{K}$ and final $\boldsymbol{K}'$ states in

Eq. 2.36 [119, 120, 121], with

$$g(\boldsymbol{K}) = \begin{cases} 1 & s \\ \sin(K_x) & p \\ \sin(K_x)\sin(K_y) & d_{xy} \\ \cos(K_x) - \cos(K_y) & d_{x^2-y^2} \end{cases} . \tag{2.39}$$

Higher order symmetries require calculation with larger clusters.

This is the same quantity as the uniform pairing susceptibility defined in Ref. [122],

$$\begin{aligned} \chi^\alpha &= \frac{1}{N}\int_0^\beta d\tau \langle \sum_i \Delta_i^\alpha(\tau) \sum_j \Delta_j^\alpha(0) \rangle \\ &= \frac{1}{N}\int_0^\beta d\tau \langle \frac{1}{4} \sum_{mm'ij} f_{im} f_{jm'} \left(c_{i\uparrow}c_{m\downarrow}c^\dagger_{m'\downarrow}c^\dagger_{j\uparrow} - c_{i\uparrow}c_{m\downarrow}c^\dagger_{m'\uparrow}c^\dagger_{j\downarrow} - c_{i\downarrow}c_{m\uparrow}c^\dagger_{m'\downarrow}c^\dagger_{j\uparrow} + c_{i\downarrow}c_{m\uparrow}c^\dagger_{m'\uparrow}c^\dagger_{j\downarrow} \right) \rangle, \end{aligned} \tag{2.40}$$

where f_{ij} is the symmetry factor in real space, varies with spin pariring symmetry. For example, $f_{ij} = \delta_{ij}$ for s-wave; for d-wave $f_{ij} \neq 0$ if i and j are nearest neighbors and $j > i$; if the bond is along x axis $f_{ij} = 1$, otherwise $f_{ij} = -1.\Delta_i(\tau)$ is the pairing parameter defined as

$$\Delta_i(\tau) = \frac{1}{2}\sum_j f^\alpha_{ij} e^{\tau H}(c_{i\uparrow}c_{j\downarrow} - c_{i\downarrow}c_{j\uparrow})e^{-\tau H}. \tag{2.41}$$

2.5 Dynamical Susceptibilities with DCA

As has been discussed in Chap. 1, the cluster Green's function and lattice Green's function is connected by DCA approximation $\Sigma(\boldsymbol{k}, \omega) = \Sigma(\boldsymbol{K}, \omega)$. In this section, we show how cluster susceptibility and lattice susceptibility are connected within DCA approximation.

Use magnetic channel $\chi_m = \chi_{ph\uparrow\uparrow} - \chi_{ph\uparrow\downarrow}$ as an example. The Bethe-Salpeter equation is [11]

$$\chi_m^{\omega\omega'\nu}(\boldsymbol{k},\boldsymbol{k}',\boldsymbol{q}) = \chi_{0ph}^{\omega\omega'\nu}(\boldsymbol{k},\boldsymbol{k}',\boldsymbol{q}) - \frac{1}{\beta^2 N^2}\sum_{\boldsymbol{k}_1\boldsymbol{k}_2,\omega_1\omega_2}\chi_m^{\omega\omega_1\nu}(\boldsymbol{k},\boldsymbol{k}_1,\boldsymbol{q})\Gamma_m^{\omega_1\omega_2\nu}(\boldsymbol{k}_1,\boldsymbol{k}_2,\boldsymbol{q})\chi_{0ph}^{\omega_2\omega'\nu}(\boldsymbol{k}_2,\boldsymbol{k}',\boldsymbol{q}). \tag{2.42}$$

Within the DCA approximation, the single particle lattice self energy is coarse grained from its cluster counterpart, $\Sigma_\sigma(\boldsymbol{k}, i\omega) = \Sigma_\sigma(\boldsymbol{K}+\tilde{\boldsymbol{k}}, i\omega) = \Sigma_\sigma(\boldsymbol{K}, i\omega)$ and similarly the lattice susceptibility

$$\overline{\chi}_{0ph}^{\omega\omega'\nu}(\boldsymbol{K},\boldsymbol{K}',\boldsymbol{Q}) = \delta_{\omega\omega'}\delta_{\boldsymbol{K}\boldsymbol{K}'}\frac{N}{N_c}\sum_{\tilde{\boldsymbol{k}}} G_\sigma(\boldsymbol{K}+\tilde{\boldsymbol{k}}, i\omega)G_\sigma(\boldsymbol{Q}+\boldsymbol{K}'+\tilde{\boldsymbol{k}}, i\nu - i\omega'). \tag{2.43}$$

Also, using $\Gamma = \frac{\delta\Sigma}{\delta G}$ (see Fotso *et al.* [118]), we can make the DCA substitution for vertex Γ

$$\Gamma_m^{\omega\omega'\nu}(\boldsymbol{K},\boldsymbol{K}',\boldsymbol{Q}) = \Gamma_m^{\omega\omega'\nu}(\boldsymbol{K}+\tilde{\boldsymbol{k}},\boldsymbol{K}'+\tilde{\boldsymbol{k}}',\boldsymbol{Q}+\tilde{\boldsymbol{q}}) \rightarrow \Gamma_{cm}^{\omega\omega'\nu}(\boldsymbol{K},\boldsymbol{K}',\boldsymbol{Q}). \tag{2.44}$$

where the subscript ”c” means cluster quantities. To get such cluster DCA quantities, in Eq. 2.42, sum over lattice momenta with one patch of k-space to get coarse-grain equation as

$$\begin{aligned}\overline{\chi}_m^{\omega\omega'\nu}(\boldsymbol{K},\boldsymbol{K}',\boldsymbol{Q}) &= \overline{\chi}_{0ph}^{\omega\omega'\nu}(\boldsymbol{K},\boldsymbol{K}',\boldsymbol{Q}) \\ &\quad - \frac{1}{\beta^2 N_c^2}\overline{\chi}_m^{\omega\omega''\nu}(\boldsymbol{K},\boldsymbol{K}'',\boldsymbol{Q})\Gamma_{cm}^{\omega''\omega'''\nu}(\boldsymbol{K}'',\boldsymbol{K}''',\boldsymbol{Q})\overline{\chi}_{0ph}^{\omega'''\omega'\nu}(\boldsymbol{K}''',\boldsymbol{K}',\boldsymbol{Q}).\end{aligned} \tag{2.45}$$

Cluster quantities also follow the Bethe-salpeter equation,

$$\begin{aligned}\chi_{cm}^{\omega\omega'\nu}(\boldsymbol{K},\boldsymbol{K}',\boldsymbol{Q}) = \chi_{0cph}^{\omega\omega'\nu}(\boldsymbol{K},\boldsymbol{K}',\boldsymbol{Q}) \\ - \frac{1}{\beta^2 N_c^2}\chi_{cm}^{\omega\omega''\nu}(\boldsymbol{K},\boldsymbol{K}'',\boldsymbol{Q})\Gamma_{cm}^{\omega''\omega'''\nu}(\boldsymbol{K}'',\boldsymbol{K}''',\boldsymbol{Q})\chi_{c0ph}^{\omega'''\omega'\nu}(\boldsymbol{K}''',\boldsymbol{K}',\boldsymbol{Q}).\end{aligned} \tag{2.46}$$

One then combines equations (2.45) and (2.46) to eliminate the cluster vertex, Γ_c, to obtain lattice susceptibility, as

$$\overline{\chi}^{-1} = \chi_c^{-1} - \chi_{0c}^{-1} + \overline{\chi}_0^{-1} \tag{2.47}$$

where $\overline{\chi}$, χ_c, χ_{0c} and $\overline{\chi}_0$ are all matrices in cluster momentum K and frequency ω. Equation (2.45) can also be written into a compact matrix form

$$\overline{\chi}_m = \frac{\overline{\chi}_0}{1 + \frac{1}{\beta^2 N_c^2}\Gamma_{cm}\overline{\chi}_0} \tag{2.48}$$

Obtaining the lattice susceptibility within DCA in other channels follows similar steps.

To calculate the phase boundary for superconductivity and antiferromagnetism, one can identify the parameters where $\bar{\chi}_m$ and $\bar{\chi}_{pp\bar{\uparrow\downarrow}}$ diverge. The divergence of $\bar{\chi}_m$ or $\bar{\chi}_{pp\overline{\uparrow\downarrow}}$ coincides with the place where leading eigenvalue of matrices $-\frac{1}{\beta^2 N_c^2}\Gamma_{cpp\overline{\uparrow\downarrow}}\overline{\chi}_0$ or $-\frac{1}{\beta^2 N_c^2}\Gamma_{cm}\overline{\chi}_0$ equals 1 respectively. The symmetry of each fluctuation is the same as the symmetry of the corresponding eigenvector. The advantage of this method to calculate phase diagram is that one does not need to push the system to the ordered state.

2.6 Truncation Error

In real simulations, the high frequency part of Γ and χ_0 are truncated at certain fermionic frequency. This brings about a systematic error to Γ since the matrix product and inversion mix up the high frequency and low frequency part. Fortunately, when calculating the general susceptibility, Γ is not the final result and does not need to be obtained explicitly. As studied in the PhD thesis of David Luitz [123], the truncation error of fermionic high frequency tail is masked in the χ to some extent but without any correction, the susceptibility will have wrong asymptotic behavior.

The first method of extrapolating the sum of all fermionic frequency is a logarithm extrapolation, assuming static χ increases as some power law with ω over certain high frequency, then

$$\log \chi_{ph}(\boldsymbol{Q},\nu)[n_c] = \log \frac{1}{\beta^2 N_c^2} \sum_{\boldsymbol{KK'}} \sum_{i\omega_n i\omega'_n}^{n_c<n<n_c} {\chi_{ph}^{\omega\omega'}}^{\nu}(\boldsymbol{KK'Q}) \propto \frac{1}{n_c} \propto \frac{1}{\omega_c} \tag{2.49}$$

In Fig. 2.3, we calculate $\chi_{ph}(\boldsymbol{Q},\nu) = \frac{1}{\beta^2 N_c^2} \sum_{\boldsymbol{KK'}\omega\omega'} {\chi_{ph}^{\omega\omega'}}^{\nu}(\boldsymbol{KK'Q})$ with different limited frequency. At high frequency, this curve becomes linear and we can extrapolate it to $\frac{1}{\omega_c} = 0$. The second method make use of the fact that χ and χ_0 have the same asymptotic behavior and $\chi - \chi_0$ decreases to zero fast at all momentum point, as shown in Fig. 2.4

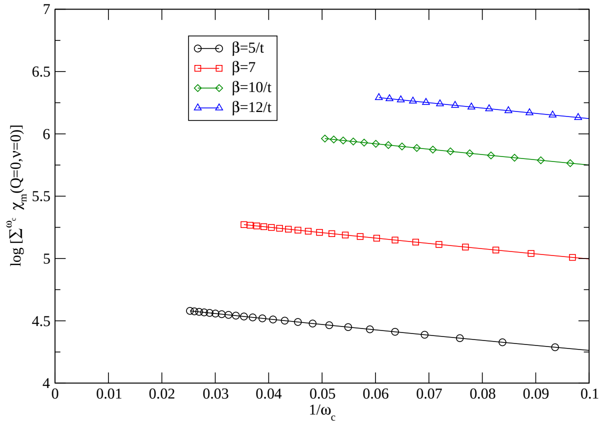

Figure 2.3: $\chi_{ph}(\boldsymbol{q},\nu)[N_c]$ as a function of inverse cut-off frequency. Data collected at $U = 6t$, $t' = -0.1t$, $\beta = 5/t, 7/t, 10/t, 12/t$, using 8-site cluster.

One should also be concerned about the truncation error of bosonic frequency when a

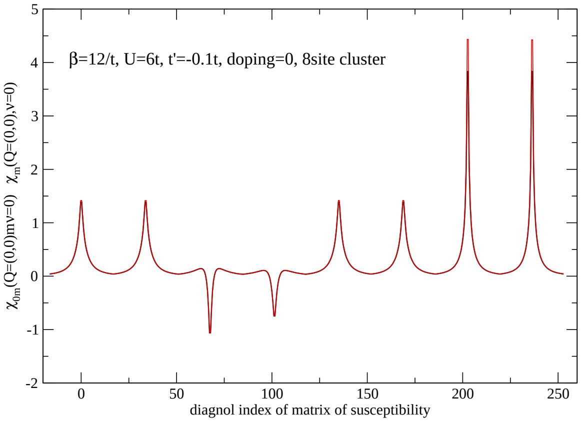

Figure 2.4: Comparison of χ_{0m} and χ_m. Data collected at $U = 6t$, $t' = -0.1t$, $\beta = 12/t$ on an 8-site cluster.

sum of bosonic Matsubara frequency is performed, for example, in the calculation of spin lattice decay rate and the analytical continuation of dynamical susceptibility. One method of dealing with such problem is explained in detail in chapter 4.

2.7 Phase Boundaries

We show in Fig. 2.5 an explicit example where the point of divergence of χ coincides with the temperature where the leading eigenvalue with $d_{x^2-y^2}$ symmetry equals 1.

Using this method, we are able to construct temperature-density phase diagram. For AFM phase boundary as plotted in Fig. 2.6, the phase transition temperatures are the intersection of leading eigenvalue with the dashed line ($\lambda_d = 1$). In Fig. 2.7, the AFM phase boundary calculated with 8 site cluster and two 16 site clusters with different configuration is plotted. When $t' \neq 0$, the AFM boundary is slightly asymmetric and tilted to the electron doped side, which is consistent with the phase diagram of real material. When the cluster size increases, the AFM regime shrinks a little. This agrees with the discovery by Jarrel [89] *et al.* that the Neel temperature decreases slowly with larger cluster size when $N_c > 4$.

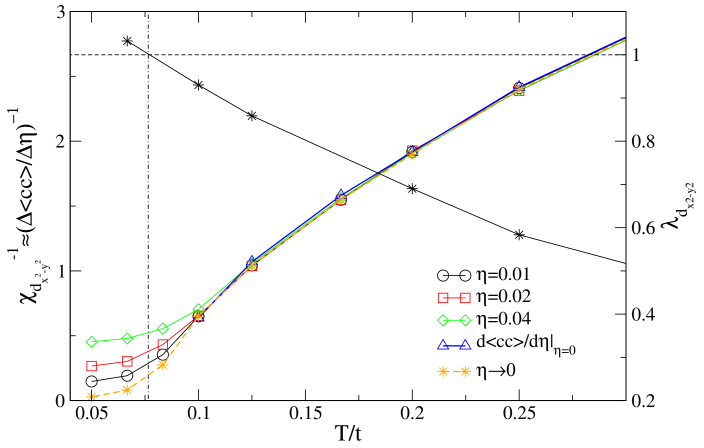

Figure 2.5: Inverse $d_{x^2-y^2}$ superconducting susceptibility plotted against temperature for the two dimensional Hubbard model with $U = 8t$, next nearest neighbor hopping t' = 0 at chemical potential $\mu = -2$, using 2 by 2 cluster. Susceptibility obtained by measuring the response of order parameter with external d-wave field strength 0.01 (solid line,circles black), 0.02 (solid line, squares, red) and 0.04 (solid line, diamonds, green). Susceptibility obtained by measuring 2-particle Green's function at normal state (solid line, triangle, blue). Also shown (right hand axis) the leading d-wave eigenvalue (solid line, star, black), $\lambda_{d_{x^2-y^2}}$, *vs* temperature. For the guide of eye, he horizontal black dashed line is where leading eigenvalue equals one. The vertical dash indicates the temprature at which $\lambda_{d_{x^2-y^2}} = 1$.

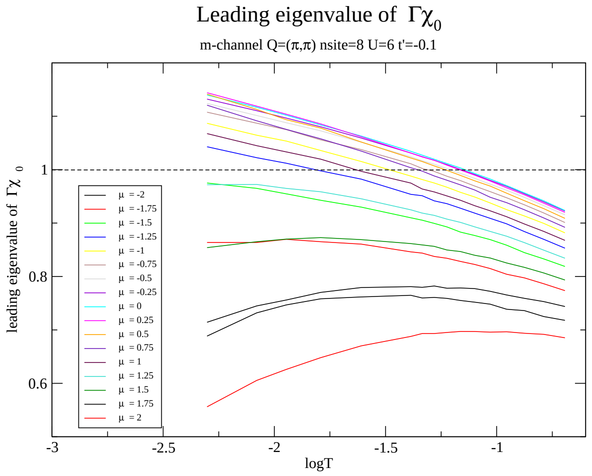

Figure 2.6: The leading eigenvalue of matrix $\Gamma_m\chi_0(Q = (\pi, \pi))$. Data collected at $U = 6t$, $t' = -0.1t$, using 8-site cluster.

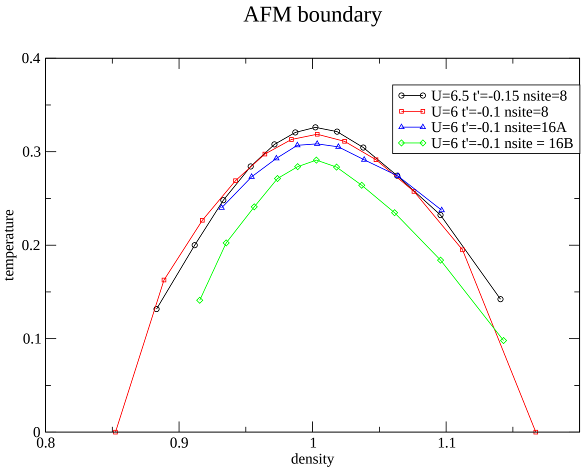

Figure 2.7: AFM boundary of the 2D Hubbard model with DCA for different cluster size/configuration, next-nearest-neighbor hopping t' and interaction U.

CHAPTER 3

Correlated Pairing Susceptibility

3.1 Overview

This chapter closely follows Ref. [124] Chen, X., LeBlanc, J. P. F., and Gull, E., *Superconducting Fluctuations in the Normal State of the Two-Dimensional Hubbard Model, Phys. Rev. Lett.*, Vol. 115, Sep 2015, pp. 116402. It starts with a brief discussion about the background. In Sec. 3.2, we also introduce and the validate our method that can find the vicinity of optimal superconducting region with high efficiency. Sec. 3.3 and Sec. 3.4 shows the results and discoveries using this method.

3.2 Introduction

From Fig. 1.2 and Fig. 1.5, we realize that the value of T_c differs largely among materials and also depends on the concentration of doping ions. Some questions arise: what are the underlying factors that suppress or increase the critical temperature? If we describe the system with a model, how to find the set of parameters that optimize superconducting transition temperature? Can we use the results as a ”recipe” to synthesize better superconducting compound? These questions have been primary motivations, in the sense of both theoretical analysis and practical application, behind computational research of strongly correlated systems.

Study superconductivity with two-particle quantities in the particle-particle channel is not new idea. There are several results [125, 120, 126]of the temperature dependence of pair-field susceptibility P and uncorrelated pair-field susceptibility of the 2D Hubbard model in different symmetries on finite lattices. These results show enhanced response in $d_{x^2-y^2}$ and s^* and suppressed response in other symmetries at zero and finite doping. Pairing in ground state has also been intensively studied where multiple symmetries were found at various doping and t'[127, 128, 129]

The most direct method is to allow the system to enter superconducting phase and a steep change in order parameter indicates the critical temperature. In the last chapter, another method of getting phase boundary using the Bethe-Salpeter equation was presented. We can systematically lower the temperature with each parameter set and get the actual T_c. Despite its advantage of detecting phase transition by simulation only in ”normal” state i.e. paramagnetic state or non-superconducting state, it is still difficult computationally since the workload increase as β^3, accompanied by more severe sign problem at lower temperatures. In this chapter, we specially address the problem of optimizing the superconducting transition temperature in the 2D Hubbard model by analyzing wide regions of parameter space. This is made possible by using the vertex contribution to pairing susceptibility as an indicator of the proximity to superconducting transition temperature at much higher temperature.

The superconducting correlation function $\chi_{pp\overline{\uparrow\downarrow}}$, obtained by linear response theory in the last chapter, diverges at superconducting phase transition. The divergence of $\chi^{\omega\omega'\nu}$ is caused by the vertex correction part $\chi^{\omega\omega'\nu} - \chi_0^{\omega\omega'\nu}$. We impose a shorthand notation for this quantity of interest, which we call the correlated pairing susceptibility P_g, where g refers to the corresponding symmetry function defined in Eq. 2.39, and we take this to be the summation over fermionic Matsubara frequencies and momenta

$$P_g := (\chi - \chi_0)_g = \frac{1}{\beta^2}\sum_{\omega\omega'\boldsymbol{K}\boldsymbol{K}'} g(\boldsymbol{K})g(\boldsymbol{K}') \tag{3.1}$$
$$\times \left(\chi^{\omega\omega'0}_{pp\overline{\uparrow\downarrow}}(\boldsymbol{K},\boldsymbol{K}',0) - \chi_0^{\omega\omega'0}(\boldsymbol{K},\boldsymbol{K}',0)\right) / \sum_{\boldsymbol{K}} g(\boldsymbol{K})^2.$$

The fact that the correlated pairing susceptibility P_g must become large on approach to T_c grants us additional insights at $T > T_c$, where P_g can be used as a qualitative measure of the proximity of the system to a transition. The left panel of Fig. 3.1 shows the critical temperature obtained from systematically reducing T and explicitly evaluating the eigenvalues of $-\frac{1}{\beta^2}\Gamma_{pp\overline{\uparrow\downarrow}}\chi_0$ to find the divergence of the $d_{x^2-y^2}$ susceptibility. The right panel contrasts this with the magnitude of P_g at much higher temperatures $\beta = 10/t$, $15/t$, $20/t$, and $25/t$. We see P_g tracks T_c and shows the largest superconducting fluctuations approximately where T_c is highest, as also indicated by the vertical blue lines. The correspondence of P_g to T_c improves as T decreases towards T_c. We can plot the same set of data into a contour plot and compare it to the phase diagram of doping and interaction obtained at $\beta = 60$. As shown in the Fig. **??**, the region that has the largest value of $P_{d_{x^2-y^2}}$ (region inside the

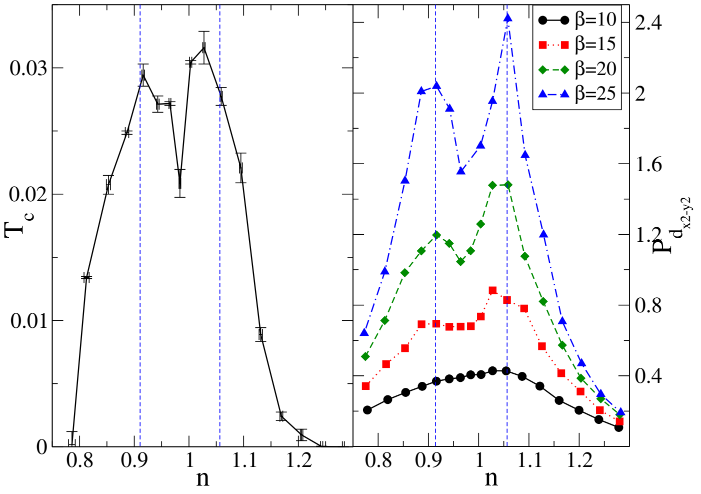

Figure 3.1: Left panel: Superconducting critical temperature of the Hubbard model with nearest neighbour hopping and no next nearest neighbour hopping for $U = 6t$ using an $N_c = 8$ dynamical cluster approximation. Right panel: $P_{d_{x^2-y^2}}$ at different temperatures with $U = 6t$ and $t' = -0.1t$ using an $N_c = 8$ cluster.

red line in the bottom of the left panel) coincides with the superconducting state in phase diagram. These two evidences proved that the correlated pairing susceptibility $P_{d_{x^2-y^2}}$ is

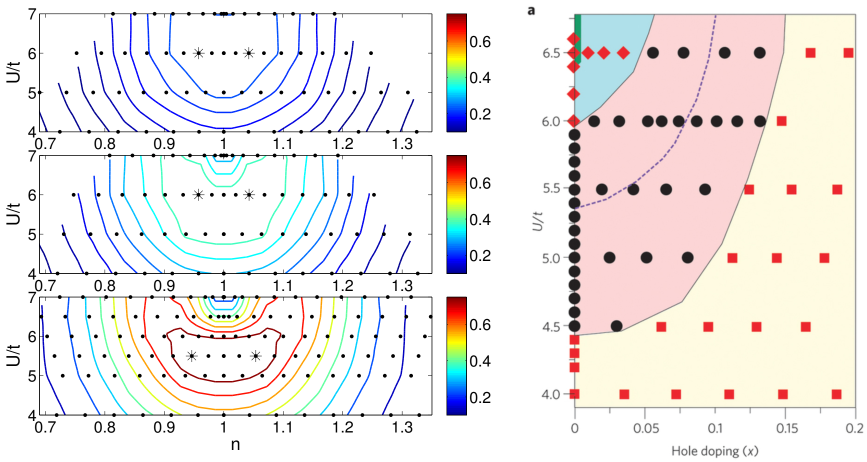

Figure 3.2: Left: the contour plot of $P_{d_{x^2-y^2}}$ of the Hubbard model with nearest neighbour hopping and next nearest neighbour hopping $t' = -0.1t$ for $U = 6t$ at different temperature using an $N_c = 8$ dynamical cluster approximation. From top to bottom: $\beta = 7/t$, $\beta = 10/t$ and $\beta = 15/t$. Right: Theoretical phase diagram obtained from cluster dynamical mean-field calculations, showing Fermi liquid (yellow), superconducting (pink) and pseudogapped but not superconducting region (blue); boundary of pseudogap region shown as dashed line. Right panel adapted from Ref. [12].

a good indicator for inducibility of superconductivity and can be used to locate best parameter set for superconductivity at temperature much higher than T_c. Therefore, this will allow as to sweep large range of parameters with less computational burden and less sign problem. In the next few sections, we use this method to explore maximum superconducting fluctuation in parameter regions of interaction, doping level, next-nearest-neighbor hopping and pairing symmetry.

3.3 The Optimal Parameters

In Fig. 3.3(a) we explore $P_{d_{x^2-y^2}}$ as a function of particle density n ($n = 1$ denotes half filling) in the intermediate interaction strengths regime $U/t = 4$ to 7 at $\beta = 15/t \approx 2T_c$. For the weakest interaction strength considered here, $U = 4t$, the superconducting

$d_{x^2-y^2}$ fluctuations are strongest at half filling and decrease rapidly towards larger hole and electron doping. At 10% doping, the model has been shown to be $d_{x^2-y^2}$ superconducting by DCA calculations extrapolated to the thermodynamic limit [89], and 8-site fluctuations have shown to be weaker than for the lattice model. The maximum of fluctuations at half filling is consistent with results from weak coupling theory [130], FLEX [131], and diagrammatic Monte Carlo in the weak coupling limit [121], and is also observed in results from lattice quantum Monte Carlo [132] and the two-particle-self-consistent approximation [133]. Reduction of U rapidly suppresses the strength of fluctuations. $P_{d_{x^2-y^2}}$ increases at all n as U is raised to $5t$. As U is further raised to $6t$, the strength of fluctuations increases away from half filling but decreases near half filling, and the fluctuation maximum moves to finite doping, establishing a dome. The suppression at half filling coincides with the establishment of a pseudogap at this interaction strength [134, 135], and is also seen in QMC [120] and TPSC [136, 133] (though it seems to be absent in four-site CDMFT [137]). Simulations directly in the superconducting phase [138] have also shown that that superconductivity in this region is suppressed.

Above $U/t = 6.4$ the half-filled system becomes Mott insulating [135] and superconducting fluctuations are further suppressed (but remain non-zero), while their maximum strength moves to higher doping, giving the appearance of a dome structure centered at doping, $\delta \sim \pm 1/8$ for $U/t \sim 8$. As the interaction strength is further increased, fluctuations are suppressed and quickly decay, in qualitative agreement with simulations of the $t - J$ model [139] and Hubbard NLCE calculations [122].

Fig. 3.4 expands further upon the data of Fig. 3.3, including additional data points at intermediate interaction values, as a false color contour plot at $t' = 0$ in Fig. 3.4(a). The plot clearly shows the intermediate interaction region most conducive to superconductivity. The point of maximum susceptibility which occurs at U^{max}, n^{max} is marked as + and occurs at $U/t = 6$, $n = 0.92$ for the 8-site cluster. A wide area in the vicinity of this point exhibits fluctuation within 10% of the maximum value, showing that $d_{x^2-y^2}$ superconducting fluctuation is a robust feature of the model. Finite size effects change the precise location and general strength of the fluctuations (see supplemental material) but not the overall shape. Long-range antiferromagnetism may preempt the superconducting phase near half filling, see e.g. Ref. [140].

Next-nearest neighbor hopping, shown in Fig. 3.3 and Figs. 3.4 panels (b) and (c), has a profound effect on $d_{x^2-y^2}$ fluctuations. As the interaction strength is raised, a pronounced particle hole asymmetry appears for $t'/t = -0.1$ (panel (b)) that increases superconducting fluctuations on the electron doped side ($n > 1$) while suppressing them on the hole doped side. Increasing t' to $-0.2t$ (Fig. 3.3(c)) leads to a further enhancement of fluctuations on the electron doped side and increased suppression on the hole doped side near half filling. This behavior seems to be unrelated to any feature in the single particle density of states which has a van Hove maximum on the hole-doped side. Rather, we attribute it to the establishment of a pseudogap on the hole doped side, which is absent on the electron doped side [135], and which is know to rapidly suppress critical temperature near half filling [138]. The magnitude of fluctuation at the electron doped side (and outside of the pseudogap region at the hole doped side) is not significantly changed, suggesting (in agreement with ED and DMRG simulations on $t - J$ ladders [141, 139] and NCA results on 2×2 clusters) that the t' trends observed in real materials are not captured by the single band Hubbard model [142]. We find that further increase of t' continues this trend and reduces the overall susceptibility to $d_{x^2-y^2}$ superconductivity.

Our results suggest that the low-energy effective models of high T_c compounds do not just differ by t', but also by their on-site interactions U. As the electron doped compounds have a much lower critical temperature than the hole doped ones, we surmise that they are not localized at the point in phase space that yields the highest T_c, and that an increase of U would rapidly increase the critical temperature.

We also explore the variation in system size in Fig. 3.5 for $N_c = 4$, 8, and 16 at temperatures $\beta t = 10$, 15 and 5 respectively, which corresponds to $\approx 2T_c^{\max}$ for $N_c = 4, 8$

and $\approx 8T_c^{\text{max}}$ for $N_c = 16$. We remark that larger clusters and lower temperatures are in principle accessible for some of the points presented in this phase diagram, but that the sign problem prevents us from showing an overview over the entire phase space for much lower T. For $N_c = 4$ the maximum in $P_{d_{x^2-y^2}}$ has been split into two along the line $n = 1$, due to the tendency of the 2×2 plaquette to form a Mott insulating phase at much weaker interaction than larger clusters (note that the physics of this cluster in DCA is different from the pseudogap physics observed on larger clusters, see, e.g., Refs. [143, 144]). We see that $N_c = 16$ contains no such artifact (similarly to $N_c = 8$). Further the structure near $n = 1$ is nearly identical in shape to the case of $N_c = 8$ for example, comparison to Fig. **??**(a) shows the same structure.

Fig. 3.2 and 3.5 suggest that both reduction in temperature and increase in cluster size have an equivalent effect on the location of $\{U^{max}, n^{max}\}$, but the effect appears primarily as a shift in U^{max}, to a lower value, and not as a change in optimal density, n^{max}. Convergence of these finite size effects will require larger clusters but has been done for T_c on clusters with about twice the size considered here [89].

3.4 Different Symmetries

Finally, we establish the absence of high-temperature superconducting fluctuations in other symmetry channels by considering $g(k)g(k')$ factors with alternate symmetry in the two-particle representation of the susceptibility. We plot results for $t'/t = 0$, -0.1 and -0.2 in Figs. 3.6(a→c) at $U/t = 6$, for d_{xy} and p-wave symmetry and include $d_{x^2-y^2}$ for reference (also shown in Fig. 3.3).

In the large doping weak coupling regime, $d_{x^2-y^2}$ superconductivity is preempted by d_{xy} superconductivity [145, 146]. This is also found in RPA calculations [147, 148] and Diagrammatic QMC calculations [121]. In contrast, the vertex contribution to d_{xy} superconductivity is repulsive near half filling, consistent with early QMC calculations [120].

Fig. 3.6 shows how it changes sign for larger doping and eventually becomes the dominant contribution.

As U is raised in the dilute ($n \to 0$) limit, d_{xy} order is replaced immediately by p-wave superconductivity [131, 121]. Third order perturbative calculations [147] also find a large range of p-wave stability (but no d_{xy}) in the large doping regime at $U = 6$, and DCA calculations similarly found dominant p-wave contributions [149]. Within our calculations, p-wave contributions to the vertex are zero within errors in the entire range of phase space, except near half filling, where they are repulsive. Our data is consistent with Ref. [149] on the level of the susceptibility, but we find that the dominant contribution observed in that work is carried by χ_0, not the vertex part. Whether a DCA simulation could find dominant p-wave contributions to the vertex at smaller U, lower T, or on larger systems is an open question. The highest critical temperature of any non-$d_{x^2-y^2}$ superconductivity is far below the T examined in this work.

Over the entire phase space, s-wave superconductivity (not plotted in Fig. 3.6) is strongly repulsive, consistent with QMC calculations [120, 150, 151]. At $t' = -0.2$ and in the dilute limit, weak coupling and RPA results suggest a favored d_{xy} symmetry [145, 152, 148], consistent with our results at larger U/t and high temperatures.

We expand upon the exploration of symmetries in the main text, by examining the doping dependence of the superconducting order symmetry in the weak coupling regime. In Figs. 3.7 we examine the case of $U/t = 2$, a weakly coupled case, which has been suggested by recent weak coupling work to show a transition from $p-$wave to d_{xy} to $d_{x^2-y^2}$ [121]. We find from examining the leading eigenvalue at two temperatures, $\beta = 15$ and 33, that in the $n = 2$ limit has a weakly dominant p-wave component, which gives way to d_{xy} and then $d_{x^2-y^2}$ as number density is decreased towards half filling. However, in the case of d_{xy} symmetry, there is essentially no temperature dependence in the eigenvalue, suggesting no clear proximity to a divergence in this eigenvalue at the temperature examined, despite being the dominant channel. This is contrasted by the same temperature change, and it's effect on $\lambda_{d_{x^2-y^2}}$ which shows rather substantial temperature changes. Similarly the $p-$wave eigenvalue near $n = 2$ changes somewhat with β (though any T_c would be far below the temperatures accessible in this simulation).

At $n = 1.75$, the leading eigenvalue of the system has d_{xy} symmetry (Fig. 3.7 left panel) but is very far away from 1. For the same parameters, the correlated pairing susceptibility, shown in Fig. 3.7 right panel, similarly has a dominant contribution but is far away from a divergence. Decreasing temperature reduces the value of $P_{d_{xy}}$ rather than increasing it as would be expected on approach to a transition to a d_{xy} order.

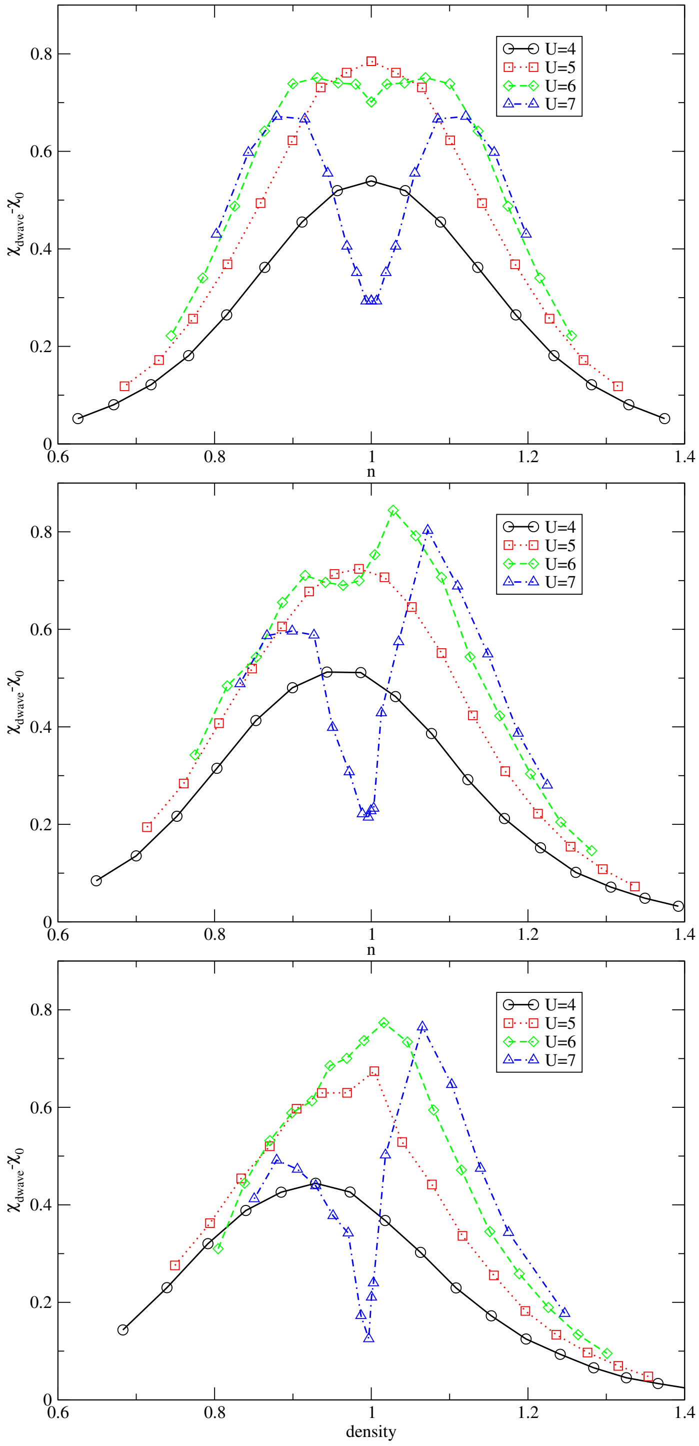

Figure 3.3: $P_{d_{x^2-y^2}}$ for different interaction strengths as a function of carrier concentration on an eight-site cluster, for $t' = 0$ (panel a), $t' = -0.1t$ (panel b) and $t' = -0.2t$ (panel c) at $\beta = 15/t$. $U = 4t$ (solid line, circle, black), $5t$ (dotted line, square, red), $6t$ (dashed line, diamond, green) and $7t$ (dash-dotted line, triangle, blue).

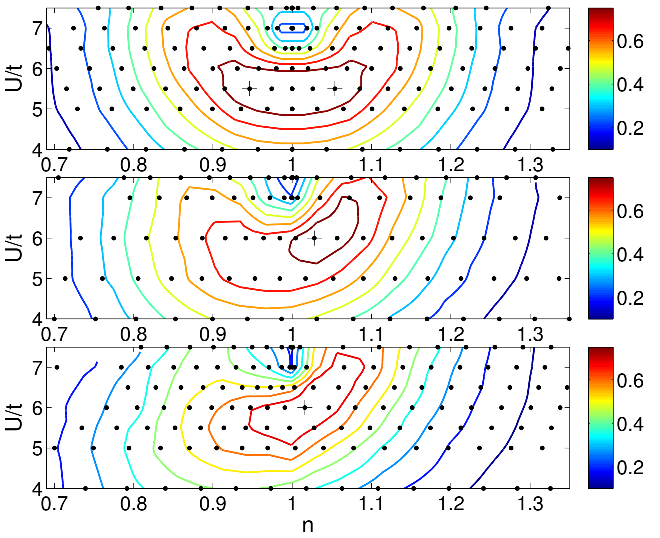

Figure 3.4: Contour plots for $P_{d_{x^2-y^2}}$ in space of interaction strength and carrier concentration on an 8-site cluster at $\beta = 15/t$. Top panel: $t' = 0$. Middle panel: $t' = -0.1t$. Bottom panel: $t' = -0.2t$. T_c^{max} occurs at $(U^{max}, n^{max}) = (5.5, 0.95$ and $1.05)$, $(6, 1.03)$, $(6, 1.01)$ respectively, marked by a + symbol.

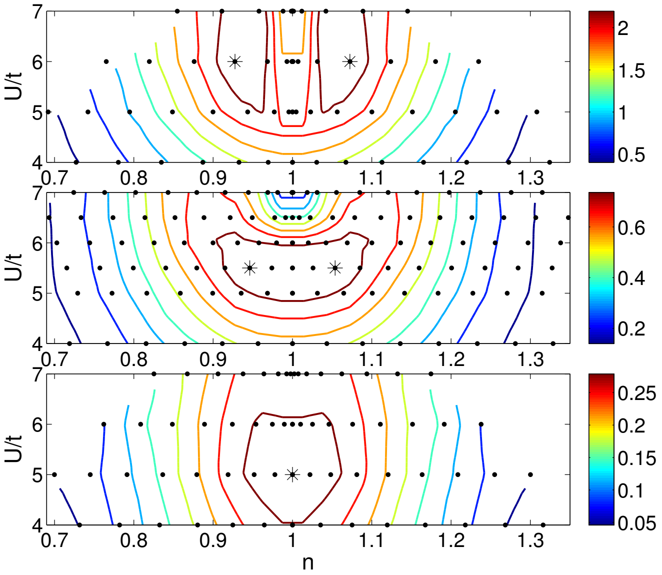

Figure 3.5: The contour plot of $P_{d_{x^2-y^2}}$ in space of interaction strength and carrier concentration with only nearest neighbour hopping. Upper panel:4-site cluster, $\beta = 10/t$; middle panel: 8-site cluster, $\beta = 15/t$; bottom panel: 16-site cluster, $\beta = 5/t$.

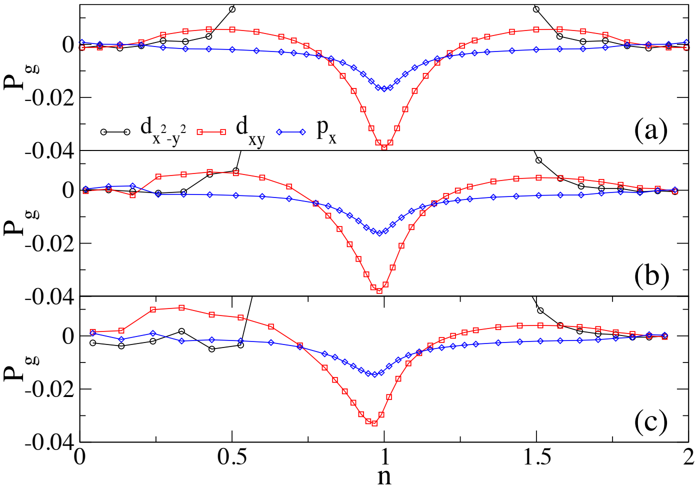

Figure 3.6: Correlated pairing susceptibility P_g in different symmetry channels with interaction strength $U = 6t$, at $\beta t = 15$, using 8-site cluster. Panel(a): $t' = 0$; panel(b): $t' = -0.1t$; panel(c): $t' = -0.2t$

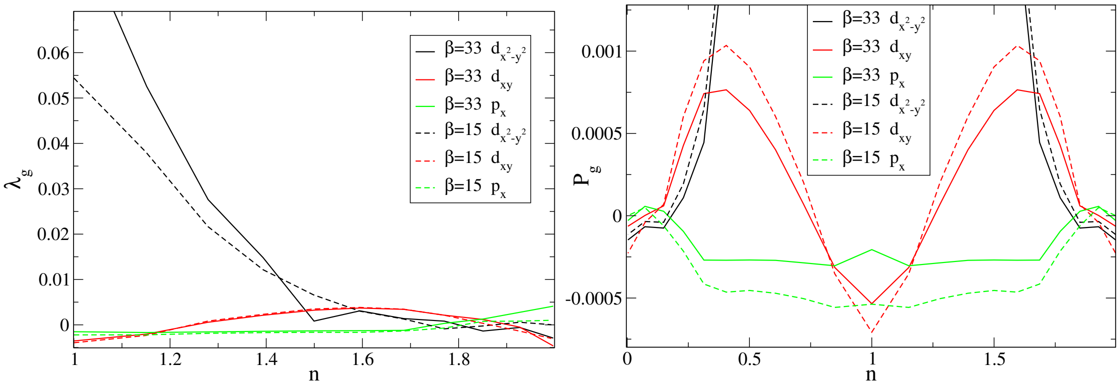

Figure 3.7: Left: The leading eigenvalue, λ_g, in each of $x^2 - y^2$, xy, and p channels for $U/t = 2$ at $\beta t = 15$ (dashed) and $\beta t = 33$ (solid). Right: The correlated pairing susceptibility, P_g, in each of $x^2 - y^2$, xy, and p channels for $U/t = 2$ at $\beta t = 33$(solid).

CHAPTER 4

Theory of NMR Response in the Cuprates

4.1 Overview

This chapter closely follows Ref. [153] Chen, X., LeBlanc, J. P. F., and Gull, E., *Simulation of the NMR response in the pseudogap regime of the cuprates, Nature Communications*, Vol. 8, Apr 2017, pp. 14986 EP –, Article. Sec. 4.2 introduces the background and motivation of simulating the NMR response. Sec. 4.3 shows the simulated results of the Knight shift and analysis of pseudogap based on the data. Sec. 4.4 and Sec. 4.5 shows results of spin-echo decay rate and spin-lattice relaxation rate respectively, including the comparison to the NMR experimental results.

4.2 Introduction

The nuclear magnetic resonance (NMR) probe measures radio-frequency radiation re-emitted from certain nuclei in the observed material [154]. The signals reveal important information about magnetic excitation in the sample, since the nuclei are coupled to their immediate magnetic environment by hyperfine interaction. The investigation of high T_c cuprates made by NMR has unveiled anomalous phenomena, provided constraints on theoretical models and implied possible origins of high temperature superconductivity. Historically, the pseudogap in the cuprates was discovered as a reduction of the Knight shift (K_{s})

and spin relaxation time T_1 measured in nuclear magnetic resonance (NMR) experiments [155, 156, 157, 158, 14].

What we accomplished in this project is developing a numerical method to simulate the NMR signal and compare the simulated and experimental results to get insight of how the NMR response related to the microscopic physics of the material. The complete theoretical understanding of the two-particle signals measured in NMR requires two components. The first one is a precise relation of the NMR signal to correlation functions [159, 160, 161] and the low-energy spin susceptibility. There are a number of efforts towards this goal and the theory is now rather mature. Shastry, Mila and Rice[159, 160] introduced the Hamiltonian that describes the effective electron-nuclear interaction for various nuclei in cuprates. Later, Zha *et.al* [162] included an extra term of the hyperfine coupling between ^{17}O nuclei and their next-nearest-neighbor Cu^{2+} to reconcile the neutron scattering results. The spin-lattice relaxation time (T_1) is related to the dynamical spin susceptibility via the fluctuation-dissipation theorem[163]. An d-wave interpretation of T_1 and T_{2g} based on RPA model was proposed by Monien and Pines [164]. These efforts result in a set of equations that connect the NMR signals and the dynamical spin susceptibility.

The second challenge to understand the NMR experiments of high T_c cuprates is the a reliable calculation of the spin susceptibility itself, which is what hinders the progress for decades. Some analysis of experimental data use curve fitting based on phenomenological relation [165]. This method often fails across phase transition boundary. Some semi-analytical models was proposed [166] based on the idea that one-component system (i.e., one spin degree of freedom per CuO$_2$ unit) with strong antiferromagnetic correlation suffices to explain the NMR data in normal state. Anaylsis was also done using random phase approximation (RPA) at weak-coupling[167, 168] and attractive Hubbard model [169]. However, before our work described in this chapter, there lacks calculation of NMR signals in the pseudogap region of cuprates using a non-perturbative method.

It is worth mentioning that there are many spectorscopic techniques that probe into the controversial pseudogap problem. They can be categorized as one-particle probes, which measure the spectral function and show depression in density of states at antinodal k-points in pseudogap region, and the two-particle probes, which measure two-particle response function or transport properties, such as optical conductivity, spin susceptibility, electronic Raman scattering. It is interesting to compare the observation and explaination of the pseudogap from different experiments. As shown in Ref. [13] (see Fig. 4.1), they conclude the same onset temperature for pseudogap. On the theoretical side, there have been intensive results from one-particle simulations [91, 170, 112, 171, 134, 135, 144, 137] of fermion model systems. We also provide a comparison of calculated results of pseudogap onset temperature and gap energy based on one-particle and two-particle quantities.

In the following sections, we will analysis the three quantities that experimentalists are most interested in, namely, the Knight shift, the spin echo decay rate and the spin lattice relaxation rate.

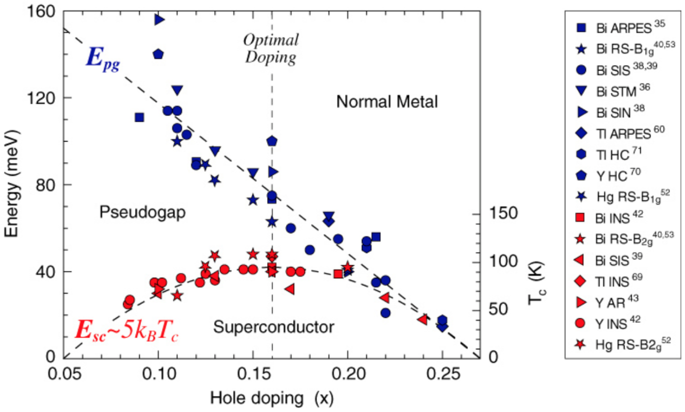

Figure 4.1: Experimental phase diagram of multiple high T_c cuprates showing the doping dependence of psedogap energy scale and superconducting transition temprature. Data collected from both one-particle quantity probes and two-particle quantity probes. Figure taken from Ref. [13]

4.3 Knight Shift

The NMR shift is a measure of resonant frequency of a nucleus in a sample relative to its value in free space. In the cuprates, according to the Mila-Rice-Shastry model [159, 160] for hyperfine coupling with itinerant Cu^{2+} holes in high T_c cuprates, the Knight shift K^S measured in nuclear magnetic resonance experiment is proportional to the uniform spin susceptibility,

$$K^S \propto \chi_m(\mathbf{q} = (0,0), \nu = 0). \tag{4.1}$$

For example, according to Ref. [161], in YBa$_2$Cu$_3$O$_7$

$$\begin{aligned}
{}^{63}K^S_{\parallel} &= \frac{A_{\parallel} + 4B}{{}^{63}\gamma_n \gamma_e \hbar^2} \chi_m(\boldsymbol{q} = 0, \nu = 0), \\
{}^{63}K^S_{\perp} &= \frac{A_{\perp} + 4B}{{}^{63}\gamma_n \gamma_e \hbar^2} \chi_m(\boldsymbol{q} = 0, \nu = 0), \\
{}^{17}K^S_{\beta} &= \frac{A_{\perp} + 4B}{{}^{17}\gamma_n \gamma_e \hbar^2} \chi_m(\boldsymbol{q} = 0, \nu = 0), \\
{}^{89}K^S &= \frac{A_{\perp} + 4B}{{}^{89}\gamma_n \gamma_e \hbar^2} \chi_m(\boldsymbol{q} = 0, \nu = 0),
\end{aligned} \tag{4.2}$$

${}^{63}K^S_{\parallel}$, ${}^{63}K^S_{\perp}$, ${}^{17}K^S_{\beta}$, and ${}^{89}K^S$ are all proportional to $\chi_m(\boldsymbol{q} = 0, \nu = 0)$, with different ratios determined by the on-site coupling strength and the transferred hyperfine coupling strength of the Cu^{2+} spin to the ${}^{63}Cu$, ${}^{17}O$ and ${}^{89}Y$ nuclei. Here the indices $\parallel$ and $\perp$ refer to the direction of the static magnetic field. $A_{\parallel}$, $A_{\perp}$, B, C_{β} and D are hyperfine coupling constants.

In Fig. 4.3 we present the simulated NMR Knight shift as a function of temperature T/t for a several doping levels x. For these parameters, the largest T_{c} on the hole doped side is $T_{\mathrm{c}} = 0.03t$ at $x = 0.09$. At large doping $x = 0.1453$ (triangle, solid blue line), the simulated Knight shift monotonically increases as T is reduced. Doped cases show a maximum at a temperature T^*_{Ks}, indicated by filled symbols. As the density decreases from $x = 0.0841$ to $x = 0$, this T^*_{Ks} gradually moves to higher T. At all temperatures studied,

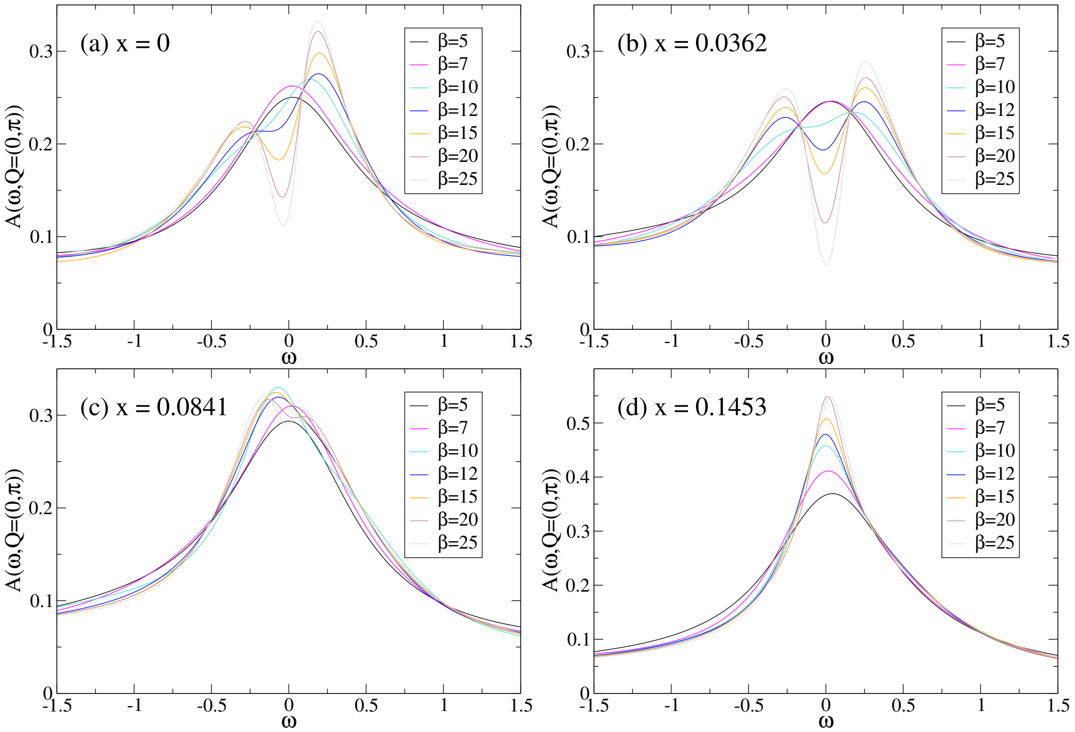

Figure 4.2: Spectral function $A(\omega, \boldsymbol{Q} = (0, \pi))$ for 8 site Hubbard model with $U = 6t$, $t' = -0.1t$, $x = 0, 0.0362, 0.0831, 0.1453$, obtained using DCA and Maxent.

the overall magnitude of the Knight shift increases as doping is increased.

Several features in the simulated results of the Knight shift described above are consistent with what is observed in NMR experiment on high T_c cuprates, and we show side-by-side comparison to those data in Fig. 4.3. Firstly, in the underdoped regime the downturn of χ as T is lowered is widely observed in K_s at various nuclei sites, see *e.g.* Fig. 8 in Ref. [158] on $YBa_2Cu_3O_{6.63}$ and Fig. 7 in Ref. [172] on $YBa_2Cu_4O_8$; and similar data for $\chi(T)$ is found in squid magnetometry of $La_{2-x}Sr_xCuO_4$ [165], which has historically been interpreted as the onset of the pseudogap phase [158]. Secondly, the increasing Knight shift with increasing doping is observed in a wide range of compounds, including $La_{2-x}Sr_xCuO_4$ [165, 173], YBa_2CuO_{7-x} and $YBa_2Cu_4O_8$ [161], and $Y_{1-x}Pr_xBa_2Cu_3O_7$ [161].

At high temperature, there is a distinct difference between the susceptibility measured in the bilayer material $YBa_2CuO_{6.63}$, which displays a broad maximum at $500K$ and remains approximately constant up to $630K$ [172], and that of the single layer material

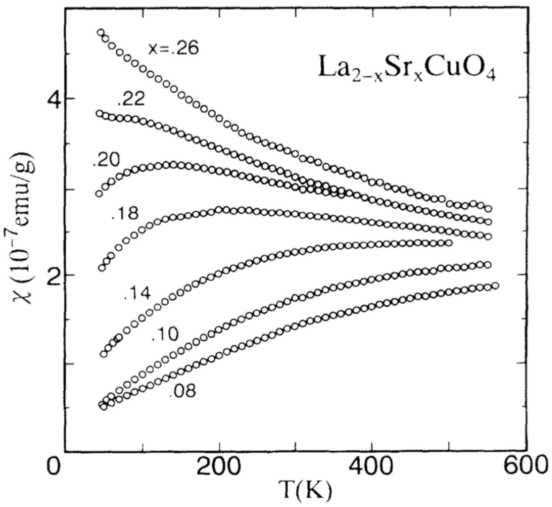

(a) Magnetic susceptibility for the superconducting samples of $La_2Sr_xCuO_4$. (Fig.4 in Ref. [165])

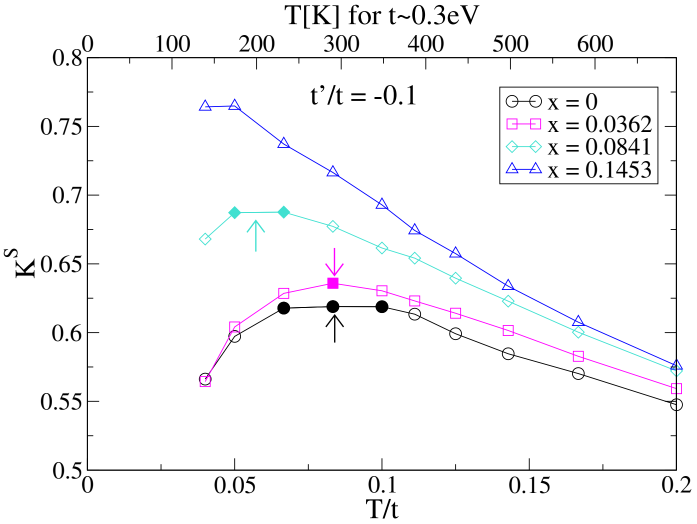

(b) Knight shift $K^S \propto \chi_m$ as a function of temperature T/t (lower x-axis) for a series of doping levels computed at $U = 6t$, $t' = -0.1t$ obtained from 8-site DCA. Filled symbols: the peak positions of the Knight shift. Arrows: onset of normal state pseudogap obtained by analytical continuation of the single particle spectral function at $\boldsymbol{K} = (0, \pi)$. Upper x-axis: T/t in units of Kelvin assuming $t \sim 0.3eV$.

Figure 4.3: Side-by-side comparison of Knight shift.

$La_{2-x}Sr_xCuO_4$ [174, 165], where measurements indicate a slowly decreasing Knight shift above T^*. This discrepancy may be caused by magnetic coupling of copper-oxygen planes in the bilayer materials. Our calculations, which are done on a purely two-dimensional system, are consistent with measurements performed on single layer materials.

The arrows in Fig. 4.3 indicate the onset temperature of the pseudogap in the single particle spectral function calculated by analytical continuation of the single particle Green's function [175] using the maximum entropy method [95, 96]. From the temperature evolution of $A_{K=(\pi,0)}(\omega)$, we define T^* as the temperature at which a suppression of the density of states appears near zero frequency. The spectral functions with same parameters as Fig. 4.3 are plotted in Fig. 4.2. In agreement with Ref. [176, 177], and as observed in a study of an attractive model [178], T^*_{Ks} exhibits the same dependence on temperature and doping level as T^*, showing crossover temperatures identified with single-particle quantities (density of states) and two-particle quantities (Knight shift) to be the same.

4.3.1 Extract Energy Scale

We can examine the gapped nature of χ_m by expanding further upon the data in Fig. 4.3 in an Arrhenius plot. As illustrated in Fig. 4.4, once a gap has fully opened, the resulting curves become straight lines within uncertainties, allowing us to interpret our data as thermal excitations over a rigid gap and to extract an energy scale from the slopes using $\chi_m(T) = \chi_0 \exp(-\Delta_{\mathrm{pg(2p)}}/T)$. The inset of Fig. 4.4 shows the comparison between the pseudogap energy determined by this method (open symbols) and the corresponding pseudogap energy extracted from the peak-to-peak distance of the single particle spectral function at the antinode (filled symbols). The two energy gaps are proportional as a function of doping. The distinct energy scales are however expected since $\Delta_{\mathrm{pg(2p)}}$ averages over the Brillouin zone while $\Delta_{\mathrm{pg(1p)}}$ only considers the antinodal momenta. As a result, their actual gap values in this case differ by a factor of 75, independent of doping. Similar comparisons for experimental data on $YBa_2Cu_4O_8$ yield values of $\Delta_{\mathrm{pg(1p)}} \approx 150\mathrm{meV}$ and

$\Delta_{\mathrm{pg(2p)}} = 7.75\mathrm{meV}$, a difference of a factor of 20[13, 179, 180, 181, 14]. Potentially, a quantitative comparison of this ratio to experiment it might allow for a more precise determination of model parameters than considering single-particle properties alone.

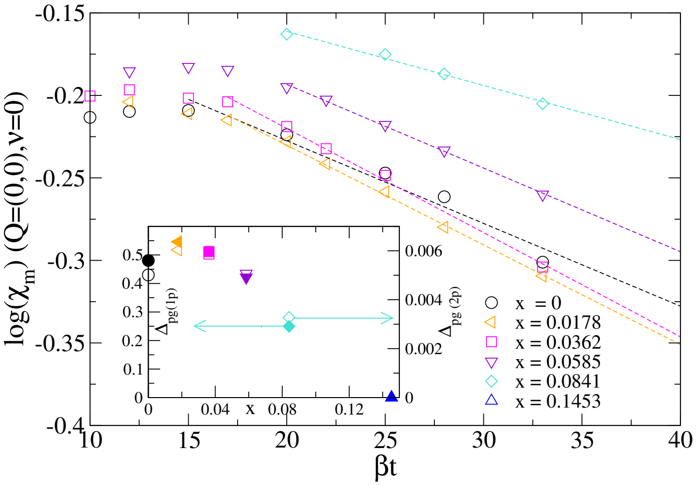

Figure 4.4: Extraction of $\Delta_{pg(2p)}$ from Knight shift data via $\chi_m(T) = \chi_0 \exp(-\Delta_{pg(2p)}/T)$. Open symbols: data of Fig. 4.3 plotted as $log(\chi_m)$ vs. β. Dashed lines: linear fits to the data in exponentially decaying regime. Inset: comparison between pseudogap energy extracted from the slope of Arrhenius plot (open symbols, right y-axis) and from the single particle spectral function at $K = (0, \pi)$ (filled symbols, left y-axis).

4.3.2 Spin Susceptibility Scaling

Another interesting scaling behavior of the spin susceptibility of LSCO materials was found in NMR experiment. For a large doping range, scaled spin susceptibilities of LSCO overlap on a universal curve, following the same scaling function $F_m(T/T_{max}(x))$. A comparison of simulated and experimental results are made in Fig. 4.5.

4.4 Spin-echo Decay Rate

Spin-echo decay rate is a measure of indirect spin-spin coupling, which is particularly important in high T_c material. For the ^{63}Cu nuclear spin echo decay rate $^{63}1/T_{2\mathrm{G}}$ in param-

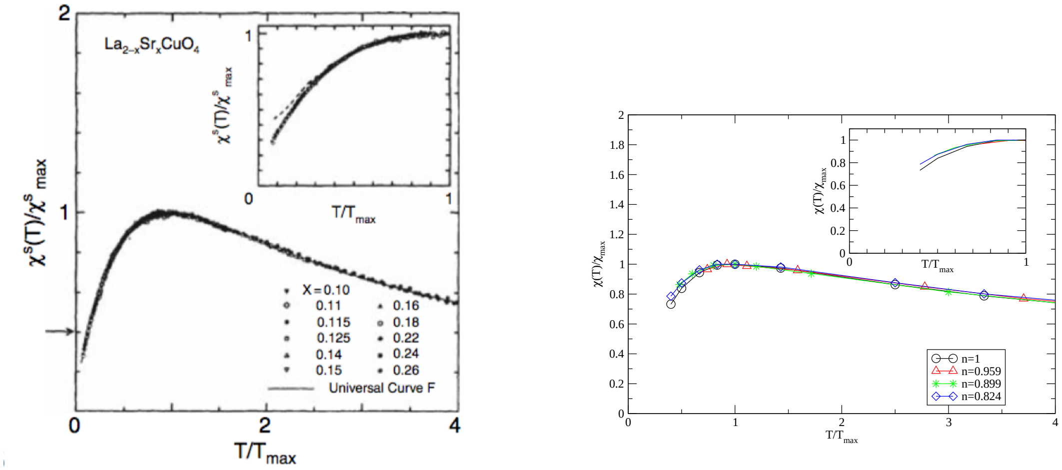

Figure 4.5: Upper panel: the scaling behavior of Knight shift from NMR experiment on LSCO. Figure taken from Ref. [14]. Lower panel: Knight shift obtained at $U = 6t$, $t' = 0$, 8-site cluster DCA, plotted as $\chi_m(T)/\chi_{m,max}$ vs. T/T_{max}. The resulting scaling curve is a "Universal Curve F" [14]

agnetic state of high T_c cuprates, [182] showed that

$$^{63}T_{2G}^{-2} = \frac{0.69}{128\hbar^2}\Big[\frac{1}{N}\sum_{\mathbf{q}} {}^{63}F_{\text{eff}}(\mathbf{q})^2\chi'_m(\mathbf{q},0)^2 - \big(\frac{1}{N}\sum_{\mathbf{q}} {}^{63}F_{\text{eff}}(\mathbf{q})\chi'_m(\mathbf{q},0)\big)^2\Big], \tag{4.3}$$

where $\chi'_m(\mathbf{q}, \nu = 0)$ denotes the real part of the real-frequency dynamical spin susceptibility at momentum $\mathbf{q}$ and frequency $\nu = 0$ and N is number of $\mathbf{q}$ points sampled in the first Brillouin zone. The prefactor 0.69 originates from the natural abundance of ^{63}Cu [183], and $^{63}F_{\text{eff}}$ is defined in Ref. [161] with hyperfine coupling constants A and B as $^{63}F_{\text{eff}} = \{A_{\parallel} + 2B[\cos(q_x a) + \cos(q_y a)]\}^2$, $A_{\parallel} = -4B$. For simplicity we set $B \equiv 1$ and consider only proportionality.

Fig. 4.7 shows the spin echo decay time T_{2G}, a measure of indirect spin-spin coupling, calculated according to Eq. 4.3. Due to the divergence of lattice susceptibility near (π, π), we use the cluster susceptibility. This quantity shows a linear rise with temperature in the normal state and increases as doping is increased. The inset of Fig. 4.7 plots this data as T_{2G}^{-1}, the spin echo decay rate. T_{2G}^{-1} becomes less temperature dependent as more charge carriers are added. Otherwise, and consistent with experiment, T_{2G} is rather featureless in

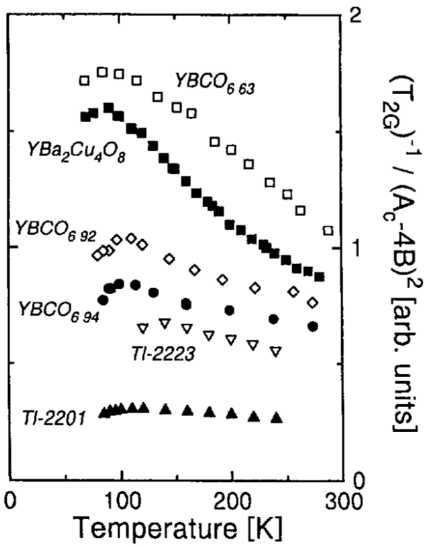

Figure 4.6: Temperature dependence of $1/T_2$ in various material. (Fig. 8 in Ref. [15])

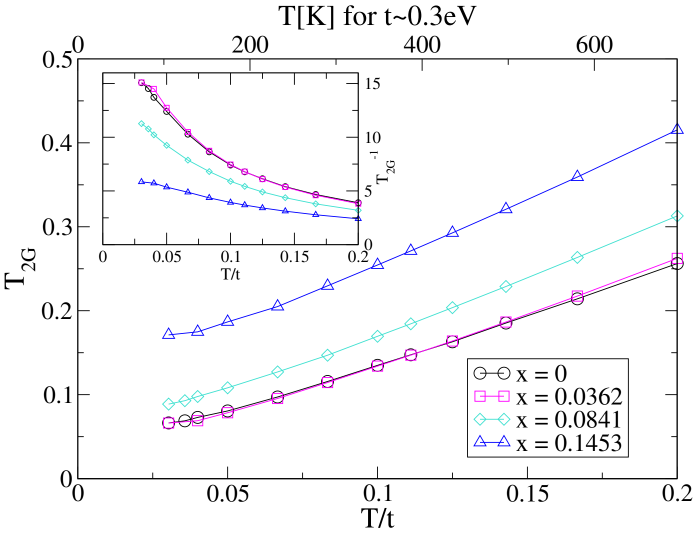

Figure 4.7: Spin echo decay time T_{2G} as a function of temperature for doping level ranging from $x = 0$ to $x = 0.145$, calculated at $U = 6t$, $t' = -0.1t$. Inset: spin echo decay rate T_{2G}^{-1}.

the normal state and shows no marked change upon entering the pseudogap region.

The linear increase of $T_{2\mathrm{G}}$ depicted in Fig. 4.7 is similar to data obtained on $\mathrm{YBa_2Cu_4O_8}$ in NMR experiments reported in Fig. 3 of [184] and Fig. 3 of [185], and NQR experiment (Fig. 4 of [172]). The change of magnitude of a factor of 4 from $100K$ to $700K$ is comparable in this calculation and experiment. The increase of $T_{2\mathrm{G}}^{-1}$ as charge carriers are added is similarly observed in $\mathrm{YBa_2Cu_3O_{7-x}}$ experiment, see e.g. Fig. 8 of Ref. [15] and Fig. 11

of Ref. [161]. We find no indication of a change of slope around $\sim 500K$ as discussed in Fig. 4 of Ref. [172].

4.5 Spin-lattice Relaxation Time

The spin-lattice relaxation rate $1/T_1$ is related to the imaginary part of dynamical spin susceptibility on the real frequency axis as

$$\frac{1}{T_1 T} \propto \lim_{\nu \to 0} \sum_{\boldsymbol{q}} {}^{\alpha}F_{\parallel}(\boldsymbol{q}) \frac{\chi''_m(\boldsymbol{q}, \nu)}{\nu}, \tag{4.4}$$

where ${}^{\alpha}F_{\parallel}(\boldsymbol{q})$ differs for ${}^{63}Cu$ and ${}^{17}O$, as defined in Ref. [161]. For the two isotopes used in this paper,

$$\begin{aligned} {}^{63}F_{\parallel} &= A_{\perp} + 2B[\cos(\boldsymbol{q}_x) + \cos(\boldsymbol{q}_y)]^2 \\ {}^{17}F_{\parallel} &= 2C_{\parallel}^2[1 + 0.5[\cos(\boldsymbol{q}_x) + \cos(\boldsymbol{q}_y)]] \\ A_{\perp} &= 0.84B, C_{\parallel} = 0.91B. \end{aligned} \tag{4.5}$$

Obtaining $\chi''_m(q, \nu)/\nu$ from Matsubara frequency data requires analytical continuation. If temperature is low enough, we can consider the parametrization

$$\chi''_m(\boldsymbol{q}, \nu) = \nu \chi_m(\boldsymbol{q}, 0)/\Gamma_{\boldsymbol{q}}. \tag{4.6}$$

We can then write the spin structure factor, $S(q, \tau)$ at time $\tau = \beta/2$ as

$$S(\boldsymbol{q}, \tau = \frac{\beta}{2}) = \int d\nu \frac{\chi_m(\boldsymbol{q}, 0)\nu}{\Gamma_{\boldsymbol{q}} \sinh \frac{\nu}{2T}} = \frac{\chi_m(\boldsymbol{q}, 0)}{\Gamma_{\boldsymbol{q}}} \int \frac{4T^2 \lambda d\lambda}{\sinh \lambda} = T^2 \pi^2 \frac{\chi_m(\boldsymbol{q}, 0)}{\Gamma_{\boldsymbol{q}}} \tag{4.7}$$

where $S(\boldsymbol{q},\tau) = \langle s^z_{\boldsymbol{q}}(\tau) s^z_{-\boldsymbol{q}}(0)\rangle$ and $S^z_{\boldsymbol{q}}$ is the real-to-k-space Fourier transform of $s^z_i = n_{i\uparrow} - n_{i\downarrow}$. To connect $S(\boldsymbol{q},\tau)$ with spin susceptibility,

$$S(\boldsymbol{q},\tau) = \langle s^z_{\boldsymbol{q}}(\tau) s^z_{-\boldsymbol{q}}(0)\rangle = \frac{1}{N}\langle \sum_{\boldsymbol{R}_i\boldsymbol{R}_j} e^{-i\boldsymbol{q}(\boldsymbol{R}_i-\boldsymbol{R}_j)} \times [n_{i\uparrow}(\tau) - n_{i\downarrow}(\tau)][n_{j\uparrow}(0) - n_{j\downarrow}(0)]\rangle$$
$$= \frac{1}{N}\langle \sum_{\boldsymbol{R}_i\boldsymbol{R}_j} e^{-i\boldsymbol{q}(\boldsymbol{R}_i-\boldsymbol{R}_j)} \times [c^\dagger_{i\uparrow}c_{i\uparrow}c^\dagger_{j\uparrow}c_{j\uparrow} - c^\dagger_{i\downarrow}c_{i\downarrow}c^\dagger_{j\uparrow}c_{j\uparrow} - c^\dagger_{i\uparrow}c_{i\uparrow}c^\dagger_{j\downarrow}c_{j\downarrow} + c^\dagger_{i\downarrow}c_{i\downarrow}c^\dagger_{j\downarrow}c_{j\downarrow}]\rangle \tag{4.8}$$

where we have omitted τ in the equation. Note that creation/annihilation operator site i has imaginary time τ and site j $\tau = 0$.

$$\frac{1}{\sqrt{N}}\sum_{\boldsymbol{q}} c_{\boldsymbol{q}} e^{i\boldsymbol{q}\boldsymbol{R}_i} = c_i,\ \frac{1}{\sqrt{N}}\sum_{\boldsymbol{q}} c^\dagger_{\boldsymbol{q}} e^{-i\boldsymbol{q}\boldsymbol{R}_i} = c^\dagger_i \tag{4.9}$$

Omitting spin indices for now, the terms in equation 4.8 become

$$\frac{1}{N^3}[\sum_{\boldsymbol{k}_1\boldsymbol{k}_2}(\sum_{\boldsymbol{R}_i} e^{iR_i(-\boldsymbol{q}+\boldsymbol{k}_1-\boldsymbol{k}_2)})c^\dagger_{\boldsymbol{k}_1}c_{\boldsymbol{k}_2}][\sum_{\boldsymbol{p}_1\boldsymbol{p}_2}(\sum_{\boldsymbol{R}_j} e^{i\boldsymbol{R}_j(\boldsymbol{q}+\boldsymbol{p}_1-\boldsymbol{p}_2)})c^\dagger_{\boldsymbol{p}_1}c_{\boldsymbol{p}_2}] \tag{4.10}$$
$$= \frac{1}{N}\sum_{\boldsymbol{k}_2} c^\dagger_{\boldsymbol{k}_2+\boldsymbol{q}}c_{\boldsymbol{k}_2}\sum_{\boldsymbol{p}_2} c^\dagger_{\boldsymbol{p}_2-\boldsymbol{q}}c_{\boldsymbol{p}_2} \tag{4.11}$$

There are four terms like this, with spin ↑↑↑↑, ↓↓↑↑, ↑↑↓↓, ↓↓↓↓ separately. Given the symmetry of 2-particle Green's function, we find

$$S(\boldsymbol{q},\tau) = \frac{1}{N}\langle(2\sum_{kk'} c^\dagger_{\boldsymbol{k}+\boldsymbol{q}\uparrow}(\tau)c_{\boldsymbol{k}\uparrow}(\tau)c^\dagger_{\boldsymbol{k}'\uparrow}(0)c_{\boldsymbol{k}'+\boldsymbol{q}\uparrow}(0)$$
$$- 2\sum_{\boldsymbol{k}\boldsymbol{k}'} c^\dagger_{\boldsymbol{k}+\boldsymbol{q}\uparrow}(\tau)c_{\boldsymbol{k}\uparrow}(\tau)c^\dagger_{\boldsymbol{k}'\downarrow}(0)c_{\boldsymbol{k}'+\boldsymbol{q}\downarrow}(0))\rangle \tag{4.12}$$

where $\boldsymbol{k} = \boldsymbol{k}_2$, $\boldsymbol{k}' = \boldsymbol{p}_2 - \boldsymbol{q}$. This is the magnetic channel susceptibility

$$S(\boldsymbol{q},\tau) = \frac{1}{N}\sum_{\boldsymbol{k}\boldsymbol{k}'} \chi_m(\boldsymbol{k}+\boldsymbol{q},\tau;\boldsymbol{k},\tau;\boldsymbol{k}',0;\boldsymbol{k}'+\boldsymbol{q},0) = \frac{2}{N}\sum_{kk'} \chi_m^{kk'q}(\tau,\tau,0). \tag{4.13}$$

Fourier transforming it to Matsubara frequency space, we obtain

$$S(\boldsymbol{q},\tau) = \frac{2}{N\beta^3}\sum_{\boldsymbol{k}\boldsymbol{k}',\omega\omega'\nu} \chi_m^{\omega\omega'\nu}(\boldsymbol{k}\boldsymbol{k}'\boldsymbol{q})e^{-i\nu\tau} \tag{4.14}$$

Within DCA,

$$\sum_{\boldsymbol{Q}} {}^{\alpha}F_{\parallel}(\boldsymbol{Q})S(\boldsymbol{Q},\tau) = \frac{2}{N\beta^3}(\frac{N}{N_c})^3 \sum_{\boldsymbol{K}\boldsymbol{K}'\boldsymbol{Q}}\sum_{\omega\omega'\nu} {}^{\alpha}F_{\parallel}(\boldsymbol{Q})\chi_m^{\omega\omega'\nu}(\boldsymbol{K},\boldsymbol{K}',\boldsymbol{Q})e^{-i\nu\tau} \tag{4.15}$$

$$= \frac{2}{\beta}\sum_{\boldsymbol{Q},\nu} {}^{\alpha}F_{\parallel}(\boldsymbol{Q})\chi_m(\boldsymbol{Q},i\nu)e^{-i\nu\tau} \tag{4.16}$$

And combining Eq. 4.6, Eq. 4.7 and Eq. 4.15 yields

$$\frac{1}{T_1} = \frac{\sum_{\boldsymbol{Q}} {}^{\alpha}F_{\parallel}(q)S(\boldsymbol{Q},\tau=\beta/2)}{\pi^2 T} = \frac{2}{\beta\pi^2 T}\sum_{\boldsymbol{Q},\nu} {}^{\alpha}F_{\parallel}(\boldsymbol{Q})\chi_m(\boldsymbol{Q},i\nu)e^{-i\nu\beta/2} \tag{4.17}$$

$$= \frac{2}{\pi^2}\sum_{\boldsymbol{Q},n} {}^{\alpha}F_{\parallel}(\boldsymbol{Q})\chi_m(\boldsymbol{Q},i\nu_n)(-1)^n. \tag{4.18}$$

Fig. 4.8 shows that DCA and RPA calculations agree in the small interaction, low temperature region. Their discrepancy at higher temperature is expected, as explained in Eq. 8 in the main text, as the quality of the approximation of $\frac{1}{T_1}$ becomes better as $T \to 0$.

Fig. 4.9 shows the simulated spin lattice relaxation rate multiplied by the inverse temperature, $(T_1T)^{-1}$, as a function of T for three dopings (see Eq. 4.17) with structure factors corresponding to copper and oxygen nuclei. All results are obtained at an interaction strength of $U = 6t$ using the cluster susceptibility. $(T_1T)^{-1}$ for ^{63}Cu (solid line) rises rapidly when temperature is reduced. As doping is reduced, the value of $(T_1T)^{-1}$ decreases, and no clear indication of the pseudogap onset temperature is visible. In contrast, $(T_1T)^{-1}$

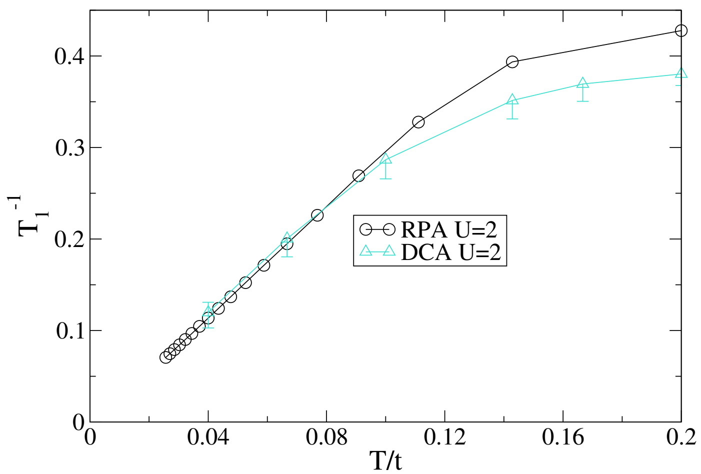

Figure 4.8: Spin lattice decay rate of 8-site Hubbard model at $U = 2t$, $t' = 0$. Black solid line, open circle symbol: RPA results. Green solid line with error bar: DCA results.

for ^{17}O (solid line) has peaks at about the same temperatures as T^*_{Ks}. $(T_1T)^{-1}$ for both ^{63}Cu and ^{17}O become doping independent at even higher temperature (see supplemental material).

While reliable results for T_1 from other theoretical methods are absent in the pseudogap regime, our results can directly be compared to real-frequency RPA calculations for T_1 in the weak coupling regime [167]. These calculations are neither limited by the momentum resolution of DCA, nor do they suffer from the limitations of analytic continuation. Therefore they provide a stringent check on the precision with which we can obtain relaxation rates. Our simulations show that T_1^{-1} smoothly decreases towards zero as temperature is reduced, in good agreement with RPA for $U = 2t$ [167], hinting at limitations of the random phase approximation in the intermediate coupling regime where deviations are apparent.

The experimentally measured spin-lattice relaxation rates are strongly material dependent. One common feature found for the planar Cu site in YBCO materials in the normal state is that $(T_1T)^{-1}$ increases slowly and linearly as T decreases in a large range of temperature above T^* [158, 179]. As T is lowered below T^*, it shows a decrease towards T_c. In contrast, experiments in LSCO materials show that $(T_1T)^{-1}$ for the planar Cu site increases rapidly as temperature is decreased until T_c, with a larger rate as the doping level is

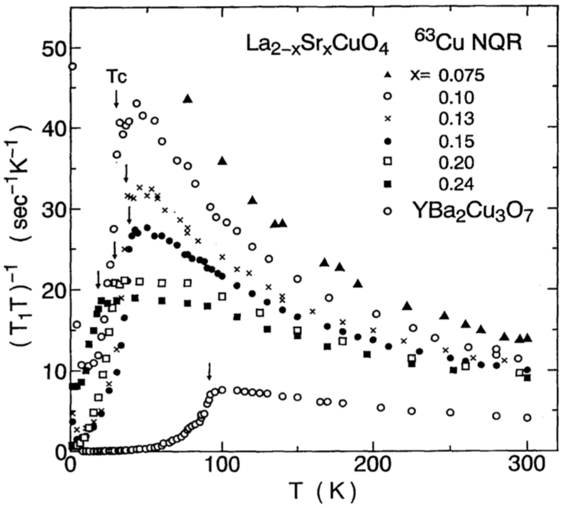

(a) Temperature dependence of $1/(T_1T)$ of Cu for $La_{2-x}Sr_xCuO_4$. $x = 0.075$(▲), 0.1(○), 0.13(×), 0.15(●), 0.2(□), 0.24(■). Data for $YBa_2Cu_3O_7$ plotted for comparison. (Fig.4 in Ref. [173])

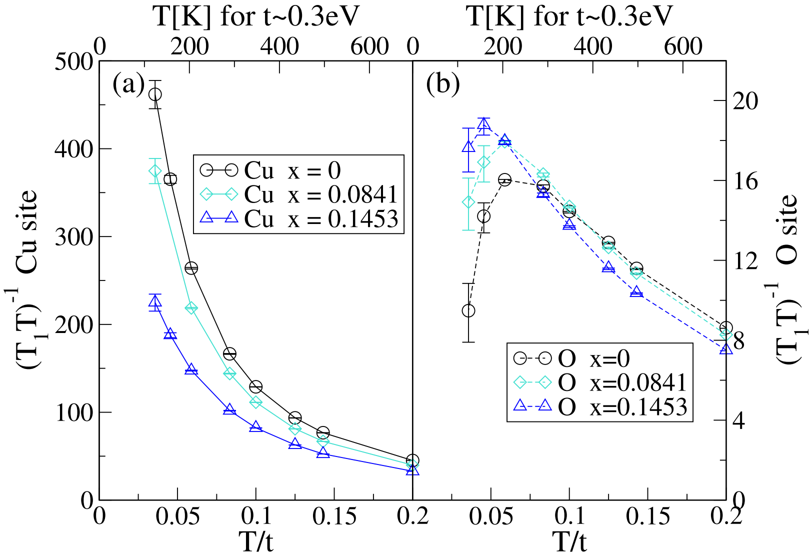

(b) $(T_1T)^{-1}$ plotted as a function of temperature at $U = 6t$, $t' = -0.1t$, for $x = 0$ to $x = 0.145$, by 8-site DCA. Panel (a), solid lines: symmetry factors corresponding to ^{63}Cu site. Panel (b), dashed line: ^{17}O site (See supplemental material for explanation of uncertainties).

Figure 4.9: Side-by-side comparison of $(T_1T)^{-1}$ for copper and oxygen sites.

decreased (see Ref. [173], Fig. 4). $(T_1T)^{-1}$ data for planar ^{17}O in LSCO are proportional to the Knight shift in the range from $100K$ to $200K$ [186]. Doping-independent $(T_1)^{-1}$ is observed in NQR experiment on LSCO above $700K$(Fig.2 in Ref. [187]), and NMR experiment on YBa$_2$(Cu$_{1-x}$Zn$_x$)$_4$O$_8$ above $150K$(Fig.2 in Ref. [188]). A comparison of these two types of materials is made in Ref. [15]. Our result is consistent with the experimental result of LSCO and inconsistent with YBCO. We attribute this to the presence of interplanar spin couplings in the latter materials [189], whose existence is confirmed by neutron-scattering experiment [190], and surmise that more complicated bilayer models might be required to yield consistent result for the YBCO spin lattice relaxation rates, also suggested from previous theoretical work [191].

Expanding upon the previous section, we comment further on the distinct behavior of the ^{63}Cu and ^{17}O signals in the calculated $(T_1T)^{-1}$ data of Fig. 4.9. Both calculations originate from the same spin susceptibility, and are distinguished only by the convolution with $^{63}F_{\|}$ and $^{17}F_{\|}$ structure factors, which are **q**-dependent functions.

In order to make these effects transparent, we present cuts in the $\mathbf{Q} = (q_x, q_y)$ plane of the static spin susceptibility on the matsubara axis, $\chi(i\nu_0, q_x, q_y)$, in Fig. 4.10(a). Plotted are 8-site DCA results, which therefore have only 4-distinct values at the M, Γ, X points and at $\mathbf{Q} = (\pi/2, \pi/2)$. As the temperature decreases, we see that the $X = (\pi, 0)$ point has no temperature dependence. There does exist temperature dependence at both $\mathbf{Q} = (\pi/2, \pi/2)$ and Γ. However, the predominant effect with reduced temperature is the strong temperature dependence of the susceptibility near $M = (\pi, \pi)$, which shows a continual increase upon decreasing temperature. This is distinct behavior from the Γ point, which shows increasing behavior until $T/t = T^* = 0.083$, after which it decreases (see inset of Fig. 4.10(b). The contribution at $\Gamma = (0, 0)$ is precisely the NMR Knight shift (see Fig. 4.3).

The impact of the strong anti-ferromagnetic (π, π) scattering vector is compounded by the influence of the Form factors $^{63}F_{\|}$ and $^{17}F_{\|}$. These are plotted in Fig. 4.10(b). We see than for the Cu sites, the $^{63}F_{\|}$ picks up both contributions of temperature dependence from $M = (\pi, \pi)$ and near $\Gamma = (0, 0)$. However, the signal is completely dominated by the monotonic increase with decreasing temperature of the susceptibility at the M-point. For oxygen sites, the $^{17}F_{\|}$ suppresses the growth of the susceptibility near (π, π), emphasizing instead the temperature dependence in the remaining regions around the Γ point. It is for this reason that NMR probes show site selective pseudogap behavior (observed on oxygen NMR and not in copper NMR).

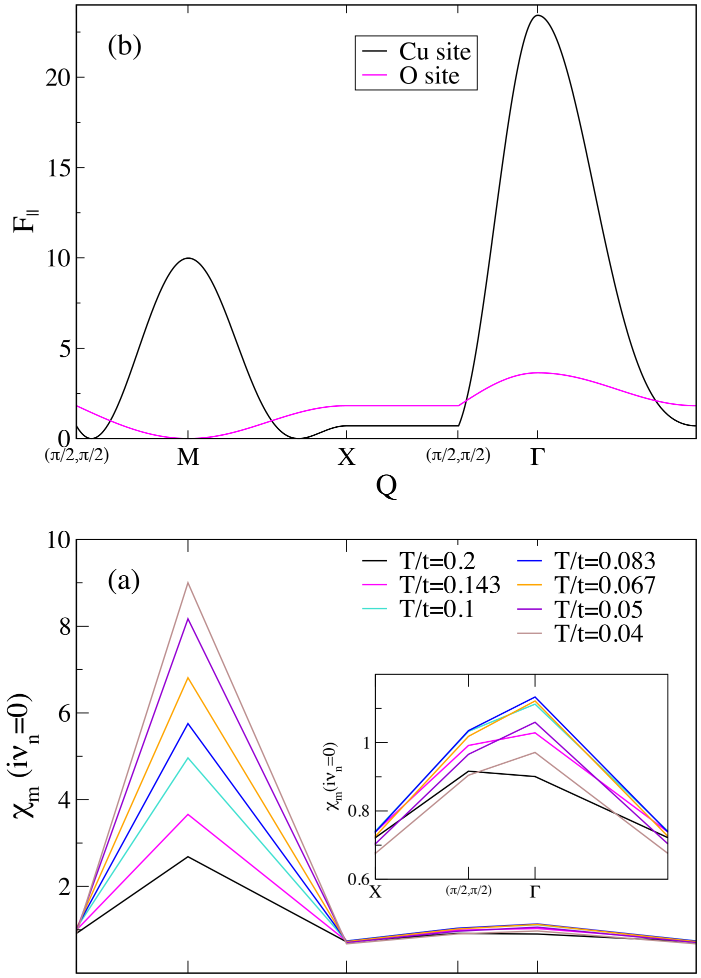

Figure 4.10: (a) Zero frequency spin susceptibility at different momentum Q for various temperatures. Inset: The same data, zoomed in near $Q = (0,0)$.(b) The structure factor for copper ($^{63}F_{\parallel}$) and oxygen ($^{17}F_{\parallel}$) sites given by equation 4.5.

CHAPTER 5

NMR Response Below Critical Temperature

5.1 Overview

This chapter presents my derivation of the two-particle quantities calculation within Nambu formalism. These equations are used for calculating two-particle Green's function, dynamical susceptibilities and vertex functions below superconducting critical temperature. Sec. 5.2 introduces the background of our work. Sec. 5.3 to Sec. 5.5 are relevant equations with their diagrammatic representations. In Sec. 5.6, the Dyson-Schwinger equation of motion provides a method of decompose the self-energy [192]. In the last section 5.7, the preliminary result of the Knight shift is shown, which is in qualitative agreement with NMR experiments on high T_c cuprate superconductor.

5.2 Introduction

NMR experiments play an essential role in the study of high T_c cuprates. One reason is that NMR is the only experiment that can measure the decay of Knight shift in the superconducting state, when the signals of other direct magnetic measurements would not be able to survive the dominant diamagnetic response [14].

Experimental NMR results tell different stories for conventional superconductors and high T_c cuprates. In conventional superconductors, the temperature-independent spin susceptibility gives rise to a constant Knight shift above T_c [193] while the Knight shift vanishes below T_c according to Yosida function [194]. As for the relaxation rate, the Korringa ratio $(T_1 T K^2)^{-1}$ is temperature independent above T_c and the NMR coherence peak (the so-called Hebel-Slichter peak) can be found in $1/T_1$ [195]. In high T_c superconductors, the NMR reponse is in clear contrast to what is predicted for conventional, BCS-type behavior. The Knight shift starts to decrease at temperature above T_c, signaling the pseudogap opening. The Korringa ratio is temperature dependent and no coherence peak was found in $1/T_1$ below T_c [196]. The enhancement in $1/T_1$ just below T_c predicted by BCS theory is also absent [197, 198]. Knight shift decreases below T_c for both parallel and perpendicular field orientations, consistent with singlet pairing of superconducting Cooper pairs [199].

To date, the theoretical and numerical analysis of the NMR response below T_c is limited to RPA-based calculations [200] or phenomenological models [201, 198, 202]. These methods are not sufficient for two reasons. Firstly, Monien and Pines [200] applied different pairing symmetries to the interpretation of NMR shift variation below T_c and found compatibility with d-wave behavior and also concluded that strong coupling is important. Therefore, it is necessary to have a non-perturbative approach for the calculation of NMR response below T_c. Secondly, most phenomenologial models fail to capture the abrupt change in Knight shift and relaxation time [201, 167] or have to use other assumptions below T_c [198].

In the previous chapter, we obtain simulated the NMR response above T_c that are in qualitative agreement with experimental results. In this chapter, we provide the equations to calculate two-particle quantities within DCA and Nambu formalism. The simulated Knight shift result is in consistent with NMR experiment above and below T_c using the same model and algorithm. A publication presenting these results is currently in preparation.

5.3 Propagator within Nambu Formalism

To study NMR signals below critical temperature T_c, we need to allow the system to enter a superconducting state. To deal with the non-zero anomalous Green's function in a convenient way, we introduce a two-component operator, the so-called Nambu spinor, proposed by Nambu [116]

$$\phi_{k\sigma} = \begin{pmatrix} c_{k\sigma} \\ c^{\dagger}_{-k-\sigma} \end{pmatrix} \qquad \phi^{\dagger}_{k\sigma} = \begin{pmatrix} c^{\dagger}_{k\sigma} & c_{-k-\sigma} \end{pmatrix}, \tag{5.1}$$

Their commutation relation is fermionic

$$\{\phi_k, \phi_q\} = \delta_{k,q}\mathbb{I} \tag{5.2}$$

where $\mathbb{I}$ is a 2×2 unit matrix. With the aid of these Nambu spinor, the Green's function can be defined as a 2×2 unit matrix.

$$\underline{G}_{\boldsymbol{k}}(\tau) = -\langle T\phi_{\boldsymbol{k}\sigma}(\tau)\phi^{\dagger}_{\boldsymbol{k}\sigma}\rangle = -\begin{pmatrix} \langle T[c_{\boldsymbol{k}\uparrow}(\tau)c^{\dagger}_{\boldsymbol{k}\uparrow}]\rangle & \langle T[c_{\boldsymbol{k}\uparrow}(\tau)c_{-\boldsymbol{k}\downarrow}]\rangle \\ \langle T[c^{\dagger}_{-\boldsymbol{k}\downarrow}(\tau)c^{\dagger}_{\boldsymbol{k}\uparrow}]\rangle & \langle T[c^{\dagger}_{-\boldsymbol{k}\downarrow}(\tau)c_{-\boldsymbol{k}\downarrow}]\rangle \end{pmatrix} \tag{5.3}$$

In this chapter, symbols with underline denote quantities constructed by normal and anomalous components in 2×2 matrix form or 2×2 block matrix form. The two anomalous Green' s function describes the creation/annihilation of a Cooper pair and are not independent. The upper right element in the matrix $\underline{G}_{01}$ is the complex conjugate of lower left element $\underline{G}_{10}$. Using the commutation relation of fermions, the diagonal elements are also connected. The full imaginary time propagator in matrix form can be written as

$$\underline{G}_{\boldsymbol{k}}(\tau) = -\begin{pmatrix} G_{\boldsymbol{k}\uparrow}(\tau) & F_{\boldsymbol{k}\uparrow}(\tau) \\ F^{*}_{\boldsymbol{k}\uparrow}(\tau) & -G_{-\boldsymbol{k}\downarrow}(-\tau) \end{pmatrix} \tag{5.4}$$

Fourier transforming them to Matsubara frequency space, we obtain

$$\underline{G}_{\boldsymbol{k}}(\omega) = \int_0^\beta \int_0^\beta e^{i\omega\tau} e^{-i\omega\tau'} \underline{G}_{\boldsymbol{k}}(\tau) \tag{5.5}$$

$$= \begin{pmatrix} G_{\boldsymbol{k}\uparrow}(\omega) & F_{\boldsymbol{k}\uparrow}(\omega) \\ F^\dagger_{\boldsymbol{k}\downarrow}(\omega) & -G_{-\boldsymbol{k}\downarrow}(-\omega) \end{pmatrix} \tag{5.6}$$

$$= \begin{pmatrix} \langle Tc_{\boldsymbol{k}\uparrow}(\omega)c^\dagger_{\boldsymbol{k}\uparrow}(\omega)\rangle & \langle Tc_{\boldsymbol{k}\uparrow}(\omega)c_{-\boldsymbol{k}\downarrow}(-\omega)\rangle \\ \langle Tc^\dagger_{-\boldsymbol{k}\downarrow}(-\omega)c^\dagger_{k\uparrow}(\omega)\rangle & \langle Tc^\dagger_{-\boldsymbol{k}\downarrow}(-\omega)c_{-\boldsymbol{k}\downarrow}(-\omega)\rangle \end{pmatrix} \tag{5.7}$$

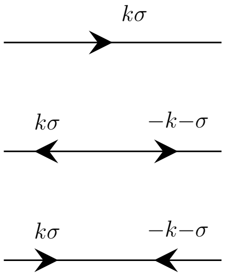

Figure 5.1: The diagram of one particle propagators. From to top to bottom: $G_\sigma(k)$, $F^*_\sigma(k)$, $F_\sigma(k)$.

In the diagrammatic form, the lines with arrow in Fig. 5.1 denote the Green's function and anomalous Green's function in momentum and Matsubara frequency space.

5.4 General Susceptibility

The full expression for two particle Green's function is obtained by substituting creation/annihilation operators with the corresponding Nambu spinor

$$\begin{aligned}
&\langle \psi_1 \otimes \psi_2^\dagger \otimes \psi_3 \otimes \psi_4^\dagger \rangle \qquad (5.8)\\
&= \begin{pmatrix} c_1^\dagger c_2 c_3^\dagger c_4 & 0 & 0 & c_{-1} c_2 c_{-3} c_4 \\ 0 & V1 & V2 & 0 \\ 0 & V3 & V4 & 0 \\ c_1^\dagger c_{-2}^\dagger c_3^\dagger c_{-4}^\dagger & 0 & 0 & c_{-1} c_{-2}^\dagger c_{-3} c_{-4}^\dagger \end{pmatrix} \qquad (5.9)
\end{aligned}$$

where the subscripts can be momentum, site coordinate, imaginary time, Matsubara frequency, spin, *etc.* The most generalized two particle Green's function has a total of 16 elements. Eight of them have odd number of creation/annihilation operators, which will be zero with only singlet coupling. The four elements at position V_1, V_2, V_3, V_4 are merely the complex conjugate of elements at the corner of the matrix. So two particle quantities can be simplified to a 2×2 matrix, with normal part and anomalous parts.

The general susceptibility can be defined as a combination of one-particle and two-particle Green's function with a similar form as what is defined within non superconducting state

$$\begin{aligned}
&\underline{\chi}_{\sigma_1\sigma_2\sigma_3\sigma_4}(r_1 r_2 r_3 r_4, \tau_1\tau_2\tau_3\tau_4) = \underline{G}_{4\sigma_1\sigma_2\sigma_3\sigma_4}(\boldsymbol{r}_1\boldsymbol{r}_2\boldsymbol{r}_3\boldsymbol{r}_4, \tau_1\tau_2\tau_3\tau_4) \qquad (5.10)\\
&- \begin{pmatrix} \underline{G}_{00}(\boldsymbol{r}_1\boldsymbol{r}_2, \tau_1\tau_2)\underline{G}_{00}(\boldsymbol{r}_3\boldsymbol{r}_4, \tau_3\tau_4) & \underline{G}_{10}(\boldsymbol{r}_1\boldsymbol{r}_2, \tau_1\tau_2)\underline{G}_{01}(\boldsymbol{r}_3\boldsymbol{r}_4, \tau_3\tau_4) \\ \underline{G}_{01}(\boldsymbol{r}_1\boldsymbol{r}_2, \tau_1\tau_2)\underline{G}_{10}(\boldsymbol{r}_3\boldsymbol{r}_4, \tau_3\tau_4) & \underline{G}_{11}(\boldsymbol{r}_1\boldsymbol{r}_2, \tau_1\tau_2)\underline{G}_{11}(\boldsymbol{r}_3\boldsymbol{r}_4, \tau_3\tau_4) \end{pmatrix} \delta_{\sigma_1\sigma_2}\delta_{\sigma_3\sigma_4} \\
&\qquad (5.11)
\end{aligned}$$

where the subscript $i, j = 0, 1$ of $\underline{G}_{ij}$ means its position in the 2×2 matrix or the block that it belongs to in a 2 block by 2 block matrix. With the symmetry of and periodicity of

Green's function and the time-translational invariance of the Hamiltonian, one can reduce the number of time/coordinate points from 4 to 3. Furthermore, when restricted to paramagnetic state, the 16 combinations of spin-indexes $\sigma_1, \sigma_2, \sigma_3, \sigma_4$ are not independent. To conserve spin, only 3 of the combinations remain: (1)↑↑↑↑=↓↓↓↓= $\sigma\sigma$; (2)↑↑↓↓=↓↓↑↑= $\sigma\sigma'$; (3)↑↓↓↑=↓↑↑↓= $\overline{\sigma\sigma'}$. Therefore, the definition can be simplified to

$$\underline{\chi}_{\sigma\sigma'}(\boldsymbol{r}_1\boldsymbol{r}_2\boldsymbol{r}_3, \tau_1\tau_2\tau_3) = \underline{G}_{4\sigma\sigma'}(\boldsymbol{r}_1\boldsymbol{r}_2\boldsymbol{r}_3, \tau_1\tau_2\tau_3) \tag{5.12}$$

$$- \begin{pmatrix} \underline{G}_{00}(\boldsymbol{r}_1\boldsymbol{r}_2, \tau_1\tau_2)\underline{G}_{00}(\boldsymbol{r}_3, \tau_3) & \underline{G}_{10}(\boldsymbol{r}_1\boldsymbol{r}_2, \tau_1\tau_2)\underline{G}_{01}(\boldsymbol{r}_3, \tau_3) \\ \underline{G}_{01}(\boldsymbol{r}_1\boldsymbol{r}_2, \tau_1\tau_2)\underline{G}_{10}(\boldsymbol{r}_3, \tau_3) & \underline{G}_{11}(\boldsymbol{r}_1\boldsymbol{r}_2, \tau_1\tau_2)\underline{G}_{11}(\boldsymbol{r}_3, \tau_3) \end{pmatrix} \tag{5.13}$$

$\chi_{\overline{\sigma\sigma'}}$ has similar definition, but the second term is zero. To calculate quantities relevant to NMR reponse, I will temporarily skip the calculation in the $\overline{\sigma\sigma'}$ channel.

When switching to momentum and frequency space, the same $ph-$ and $pp-$ channel Fourier transform in Eq. 2.5 and Eq. 2.4 can be applied to get $\chi_{ph}(\boldsymbol{k}\boldsymbol{k'}\boldsymbol{q}, \omega\omega'\nu)$ and $\chi_{pp}(\boldsymbol{k}\boldsymbol{k'}\boldsymbol{q}, \omega\omega'\nu)$. From this point, we will use the notation $k \equiv (\boldsymbol{k}, \omega)$ and $q \equiv (\boldsymbol{q}, \nu)$ in the equations and diagrams.

The measurement of G_4 is the core issue and the most computationally expensive part of calculating 2-particle Green's function and vertex functions. To obtain it, we first measure the two-frequency Green's function in Nambu formalism as

$$\underline{G}_{kp} = \langle T\psi_k\psi_p^\dagger\rangle = \langle T \begin{pmatrix} c_{k\uparrow}c_{p\uparrow}^\dagger & c_{k\uparrow}c_{-p\downarrow} \\ c_{-k\downarrow}^\dagger c_{p\uparrow}^\dagger & c_{-k\downarrow}^\dagger c_{-p\downarrow} \end{pmatrix} \rangle \tag{5.14}$$

The measurement of this quantity is performed stochastically in the CTAUX solver, with formula similar to that of one-frequency Green's function measurement. With DCA approximation,

$$\underline{G}_{KP} = \delta_{K,P}\underline{G}^0(K) - \frac{1}{\beta N}\underline{G}^0(K)[\sum_{r,s} e^{i(\omega\tau_r + KX_r)}\underline{M}_{r,s}e^{-i(\omega'\tau_s + PX_s)}]\underline{G}^0(P) \tag{5.15}$$

We employ Wick's Theorem

$$\begin{aligned}
G_{4ph\uparrow\downarrow}(k,k',q) &= \frac{1}{\beta N}\langle c^{\dagger}_{k\uparrow}c_{k+q\uparrow}c^{\dagger}_{k'+q\downarrow}c_{k'\downarrow}\rangle \\
&= -\langle c_{k+q\uparrow}c^{\dagger}_{k\uparrow}\rangle\langle c^{\dagger}_{k'+q\downarrow}c_{k'\downarrow}\rangle + \langle c^{\dagger}_{k'+q\downarrow}c^{\dagger}_{k\uparrow}\rangle\langle c_{k+q\uparrow}c_{k'\downarrow}\rangle \\
&= -\underline{G}_{11}(-k,-k-q)\times\underline{G}_{00}(k',k'+q)+\underline{G}_{10}(-k'-q,k)\times\underline{G}_{01}(k+q,-k') \\
&= -\underline{G}_{00}(k+q,k)\times\underline{G}_{11}(-k'-q,-k')+\underline{G}_{10}(-k,k'+q)\times\underline{G}_{01}(k',-k-q)
\end{aligned} \tag{5.16}$$

$$\begin{aligned}
G_{4ph\uparrow\uparrow}(k,k',q) &= \frac{1}{\beta N}\langle c^{\dagger}_{k\uparrow}c_{k+q\uparrow}c^{\dagger}_{k'+q\uparrow}c_{k'\uparrow}\rangle \\
&= \langle c_{k+q\uparrow}c^{\dagger}_{k\uparrow}\rangle\langle c_{k'\uparrow}c^{\dagger}_{k'+q\uparrow}\rangle - \langle c_{k'\uparrow}c^{\dagger}_{k\uparrow}\rangle\langle c_{k+q\uparrow}c^{\dagger}_{k'+q\uparrow}\rangle \\
&= \underline{G}_{00}(k+q,k)\times\underline{G}_{00}(k',k'+q)-\underline{G}_{00}(k',k)\times\underline{G}_{00}(k+q,k'+q) \\
&= \underline{G}_{11}(-k,-k-q)\times\underline{G}_{11}(-k'-q,-k')-\underline{G}_{11}(-k,-k')\times\underline{G}_{11}(-k'-q,-k-q)
\end{aligned} \tag{5.17}$$

$$\begin{aligned}
G_{4pp\uparrow\downarrow}(k,k',q) &= \frac{1}{\beta N}\langle c^{\dagger}_{k\uparrow}c_{q-k'\uparrow}c^{\dagger}_{q-k\downarrow}c_{k'\downarrow}\rangle \\
&= -\langle c_{q-k'\uparrow}c^{\dagger}_{k\uparrow}\rangle\langle c^{\dagger}_{q-k\downarrow}c_{k'\downarrow}\rangle + \langle c^{\dagger}_{q-k\downarrow}c^{\dagger}_{k\uparrow}\rangle\langle c_{q-k'\uparrow}c_{k'\downarrow}\rangle \\
&= -\underline{G}_{00}(q-k',k)\times\underline{G}_{11}(k-q,-k')+\underline{G}_{10}(k-q,k)\times\underline{G}_{01}(q-k',-k') \\
&= -\underline{G}_{11}(-k,k'-q)\times\underline{G}_{00}(k',q-k)+\underline{G}_{10}(-k,q-k)\times\underline{G}_{01}k',k'-q)
\end{aligned} \tag{5.18}$$

$$\begin{aligned}
G_{4pp\uparrow\uparrow}(k,k',q) &= \frac{1}{\beta N}\langle c^{\dagger}_{k\uparrow}c_{q-k'\uparrow}c^{\dagger}_{q-k\uparrow}c_{k'\uparrow}\rangle \\
&= \langle c_{q-k'\uparrow}c^{\dagger}_{k\uparrow}\rangle\langle c_{k'\uparrow}c^{\dagger}_{q-k\uparrow}\rangle - \langle c_{k'\uparrow}c^{\dagger}_{k\uparrow}\rangle\langle c_{q-k'\uparrow}c^{\dagger}_{q-k\uparrow}\rangle \\
&= \underline{G}_{00}(q-k',k)\times\underline{G}_{00}(k',q-k) - \underline{G}_{00}(k',k)\times\underline{G}_{00}(q-k',q-k) \\
&= \underline{G}_{11}(-k,k'-q)\times\underline{G}_{11}(k-q,-k') - \underline{G}_{11}(-k,-k')\times\underline{G}_{11}(k-q,k'-q)
\end{aligned} \tag{5.19}$$

These formulas are similar to what we have in the non-superconducting state, except that there are extra non-zero terms given by anomalous Green's functions. Besides, the two-particle anomalous Green's function is

$$\begin{aligned}
F_{4phuu}(k,k',q) &= \frac{1}{\beta N}\langle c_{-\sigma}(-k)c_{\sigma}(k+q)c_{-\sigma}(-k'-q)c_{\sigma}(k')\rangle \\
&= \langle c_{k'\uparrow}c_{-k'-q\downarrow}\rangle\langle c_{k+q\uparrow}c_{-k\downarrow}\rangle - \langle c_{k'\uparrow}c_{-k\downarrow}\rangle\langle c_{k+q\uparrow}c_{-k'-q\downarrow}\rangle \\
&= \underline{G}_{01}(k',k'+q)\times\underline{G}_{01}(k+q,-k) + \underline{G}_{01}(k',k)\times\underline{G}_{01}(k+q,k'+q)
\end{aligned} \tag{5.20}$$

$$\begin{aligned}
F_{4phud}(k,k',q) &= \frac{1}{\beta N}\langle c_{-\sigma}(-k)c_{\sigma}(k+q)c_{\sigma}(-k'-q)c_{-\sigma}(k')\rangle \\
&= \langle c_{-q-k'\uparrow}c_{k'\downarrow}\rangle\langle c_{k+q\uparrow}c_{-k\downarrow}\rangle - \langle c_{-k'-q\uparrow}c_{-k\downarrow}\rangle\langle c_{k+q'\uparrow}c_{k'\downarrow}\rangle \\
&= \underline{G}_{01}(-q-k',-k')\times\underline{G}_{01}(k+q,k) - \underline{G}_{01}(-k'-q,k)\times\underline{G}_{01}(k+q',-k')
\end{aligned} \tag{5.21}$$

The diagram of two particle quantities is shown in Fig. 5.2. As what we defined in previous chapters, these vertices has three momentum indices $\boldsymbol{k}, \boldsymbol{k}', \boldsymbol{q}$, two fermionic frequency indices ω, ω' and a bosonic frequency index ν. In Fig. 5.2, the line with arrow from left to right in the upper part means eletron propagating and the line with arrow from right to left in the lower part means hole propagating. The anomalous vertices are denoted with capital letter with a tilde on the top. Both the normal and anomalous vertices conserve

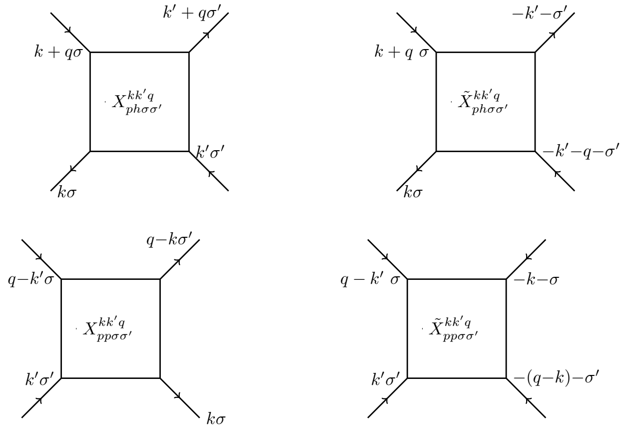

Figure 5.2: Upper left: the diagram of normal vertex in particle-hole channel. Upper right: the diagram of anomalous vertex in particle-hole channel. Lower left: the diagram of normal vertex in particle-particle channel. Upper Lower right: the diagram of anomalous vertex in particle-particle channel.

momentum, spin and charge.

It is worth mentioning that the $ph-$ and $pp-$ channel are connected by

$$\begin{aligned} X^{kk'q}_{pp\sigma\sigma'} &= X^{kk'(q-k-k')}_{ph\sigma\sigma'} \qquad & \tilde{X}^{kk'q}_{pp\sigma\sigma'} &= \tilde{X}^{kk'(q-k-k')}_{ph\sigma\sigma'} \\ X^{kk'q}_{ph\sigma\sigma'} &= X^{kk'(q+k+k')}_{pp\sigma\sigma'} \qquad & \tilde{X}^{kk'q}_{ph\sigma\sigma'} &= \tilde{X}^{kk'(q+k+k')}_{pp\sigma\sigma'} \end{aligned} \tag{5.22}$$

These relations can be easily checked by substituting the momentum and frequency indices. However, separate measurement of two-particle Green's function in each channel is still necessary, since in most cases, dynamic susceptibilities in low bosonic frequency range are needed, in $ph-$ and $pp-$ channel.

5.5 Full Vertex and Irreducible Vertex

5.5.1 particle-hole channel

In the case of an interacting system, the susceptibility can be decomposed into a bubble term (the bare susceptibility) and a vertex correction.

$$\begin{aligned}\chi^{kk'q}_{ph\sigma\sigma'} = \chi^{kk'q}_{0ph}\delta_{\sigma\sigma'} &- G(k)G(k+q)K^{kk'q}_{ph\sigma\sigma'}G(k')G(k'+q)\\ &- G(k)G(k+q)\tilde{K}^{kk'q}_{ph\sigma\sigma'}F(-k')F^{\dagger}(-k'-q)\\ &- F^{\dagger}(k)F(k+q)(\tilde{K}^{kk'q}_{ph\sigma\sigma'})^{\dagger}G(k')G(k'+q)\\ &- F^{\dagger}(k)F(k+q)(K^{kk'q}_{ph\sigma\sigma'})^{\dagger}F(-k')F^{\dagger}(-k'-q)\end{aligned} \tag{5.23}$$

$$\begin{aligned}\tilde{\chi}^{kk'q}_{ph\sigma\sigma'} = \tilde{\chi}^{kk'q}_{0ph}\delta_{\sigma\sigma'} &- G(k)G(k+q)\tilde{K}^{kk'q}_{ph\sigma\sigma'}G(-k')G(-k'-q)\\ &- G(k)G(k+q)K^{kk'q}_{ph\sigma\sigma'}F^{\dagger}(-k')F(-k'-q)\\ &- F^{\dagger}(k)F(k+q)(K^{kk'q}_{ph\sigma\sigma'})^{\dagger}G(-k')G(-k'-q)\\ &- F^{\dagger}(k)F(k+q)(\tilde{K}^{kk'q}_{ph\sigma\sigma'})^{\dagger}F^{\dagger}(-k')F(-k'-q)\end{aligned} \tag{5.24}$$

where the bubble part of χ in ph channel is

$$\underline{\chi}^{kk'q}_{0ph} = -\beta N_c \delta_{kk'} \begin{pmatrix} \underline{G}_{00}(k)\underline{G}_{00}(k+q) & \underline{G}_{10}(k)\underline{G}_{01}(k+q) \\ \underline{G}_{01}(k)\underline{G}_{10}(k+q) & \underline{G}_{11}(k)\underline{G}_{11}(k+q) \end{pmatrix} \tag{5.25}$$

With kk' as row and column index, the full $\underline{\chi}_0$ matrix can be separated evenly into four matrix, all of which are diagonal.

Recall that we restrict ourselves to the paramagnetic state, the spin index of one-particle Green's function can be omitted due to symmetry.

The full vertex K in the vertex correction term in Eq. 5.23 and Eq. 5.24 includes all possible scattering between two propogating fermions. In Ref. [11], the full vertex is rep-

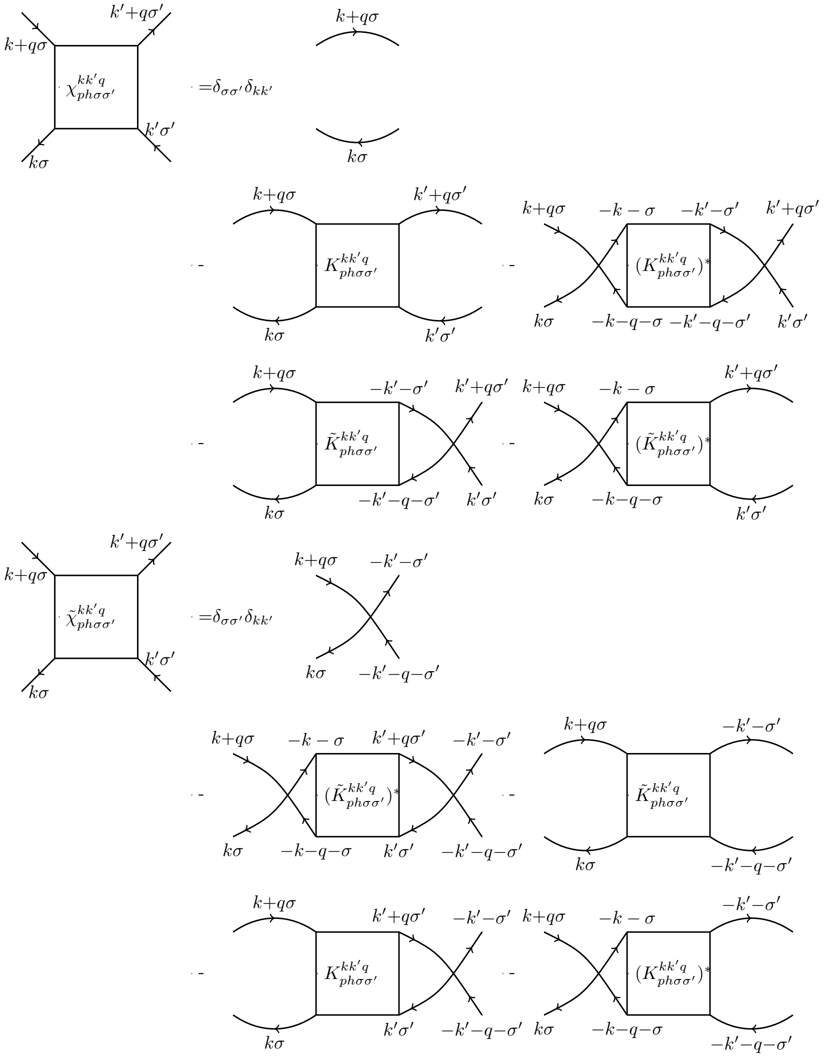

Figure 5.3: Upper: the diagram of Eq. 5.23. Lower: the diagram of Eq.5.24.

resented by capital letter F. Here we use K to avoid confusion with anomalous Green's function F. In the diagrammatic point of view, K includes all fully connected two particle diagrams. Most of them can be separated into two parts by cutting two internal Green's function lines. With this concept, we can define the irreducible vertex functions represented by two particle diagrams that cannot be separated into two parts by cutting two internal Green's function lines. The irreducible vertex act like the ”self-energy” on the two particle level. Their connection to the full vertex function is like a counterpart of Dyson's equation.

$$
\begin{aligned}
K^{kk'q}_{ph\uparrow\uparrow} = \Gamma^{kk'q}_{ph\uparrow\uparrow} &+ \frac{1}{\beta N_c}\sum_{k_1\sigma_1}\Gamma^{kk_1q}_{ph\uparrow\sigma_1}G_{\sigma_1}(k_1)G_{\sigma_1}(k_1+q)K^{k_1k'q}_{ph\sigma_1\uparrow} \\
&+ \frac{1}{\beta N_c}\sum_{k_1\sigma_1}\Gamma^{kk_1q}_{ph\uparrow\sigma_1}F^*_{\sigma_1}(k_1)F_{\sigma_1}(k_1+q)(\tilde{K}^{k_1k'q}_{ph-\sigma_1\uparrow})^* \\
&+ \frac{1}{\beta N_c}\sum_{k_1\sigma_1}\tilde{\Gamma}^{kk_1q}_{ph\uparrow\sigma_1}F_{-\sigma_1}(-k_1)F^*_{-\sigma_1}(-k_1-q)K^{k_1k'q}_{ph\sigma_1\uparrow} \\
&+ \frac{1}{\beta N_c}\sum_{k_1\sigma_1}\tilde{\Gamma}^{kk_1q}_{ph\uparrow\sigma_1}G_{-\sigma_1}(-k_1)G_{-\sigma_1}(-k_1-q)(\tilde{K}^{k_1k'q}_{ph-\sigma_1\uparrow})^*
\end{aligned} \tag{5.26}
$$

$$
\begin{aligned}
\tilde{K}^{kk'q}_{ph\uparrow\uparrow} = \tilde{\Gamma}^{kk'q}_{ph\uparrow\uparrow} &+ \frac{1}{\beta N_c}\sum_{k_1\sigma_1}\Gamma^{kk_1q}_{ph\uparrow\sigma_1}F^*_{\sigma_1}(k_1)F_{\sigma_1}(k_1+q)(K^{k_1k'q}_{ph-\sigma_1\uparrow})^* \\
&+ \frac{1}{\beta N_c}\sum_{k_1\sigma_1}\Gamma^{kk_1q}_{ph\uparrow\sigma_1}G_{\sigma_1}(k_1)G_{\sigma_1}(k_1+q)\tilde{K}^{k_1k'q}_{ph\sigma_1\uparrow} \\
&+ \frac{1}{\beta N_c}\sum_{k_1\sigma_1}\tilde{\Gamma}^{kk_1q}_{ph\uparrow\sigma_1}G_{-\sigma_1}(-k_1)G_{-\sigma_1}(-k_1-q)(K^{k_1k'q}_{ph-\sigma_1\uparrow})^* \\
&+ \frac{1}{\beta N_c}\sum_{k_1\sigma_1}\tilde{\Gamma}^{kk_1q}_{ph\uparrow\sigma_1}F_{-\sigma_1}(-k_1)F^*_{-\sigma_1}(-k_1-q)\tilde{K}^{k_1k'q}_{ph\sigma_1\uparrow}
\end{aligned} \tag{5.27}
$$

$$
\begin{aligned}
K^{kk'q}_{ph\uparrow\downarrow} = \Gamma^{kk'q}_{ph\uparrow\downarrow} &+ \frac{1}{\beta N_c}\sum_{k_1\sigma_1}\Gamma^{kk_1q}_{ph\uparrow\sigma_1}G_{\sigma_1}(k_1)G_{\sigma_1}(k_1+q)K^{k_1k'q}_{ph\sigma_1\downarrow} \\
&+ \frac{1}{\beta N_c}\sum_{k_1\sigma_1}\Gamma^{kk_1q}_{ph\uparrow\sigma_1}F^*_{\sigma_1}(k_1)F_{\sigma_1}(k_1+q)(\tilde{K}^{k_1k'q}_{ph-\sigma_1\downarrow})^* \\
&+ \frac{1}{\beta N_c}\sum_{k_1\sigma_1}\tilde{\Gamma}^{kk_1q}_{ph\uparrow\sigma_1}F_{-\sigma_1}(-k_1)F^*_{-\sigma_1}(-k_1-q)K^{k_1k'q}_{ph\sigma_1\downarrow} \\
&+ \frac{1}{\beta N_c}\sum_{k_1\sigma_1}\tilde{\Gamma}^{kk_1q}_{ph\uparrow\sigma_1}G_{-\sigma_1}(-k_1)G_{-\sigma_1}(-k_1-q)(\tilde{K}^{k_1k'q}_{ph-\sigma_1\downarrow})^*
\end{aligned} \tag{5.28}
$$

$$
\begin{aligned}
\tilde{K}^{kk'q}_{ph\uparrow\downarrow} = \tilde{\Gamma}^{kk'q}_{ph\uparrow\downarrow} &+ \frac{1}{\beta N_c}\sum_{k_1\sigma_1}\Gamma^{kk_1q}_{ph\uparrow\sigma_1}F^*_{\sigma_1}(k_1)F_{\sigma_1}(k_1+q)(K^{k_1k'q}_{ph-\sigma_1\downarrow})^* \\
&+ \frac{1}{\beta N_c}\sum_{k_1\sigma_1}\Gamma^{kk_1q}_{ph\uparrow\sigma_1}G_{\sigma_1}(k_1)G_{\sigma_1}(k_1+q)\tilde{K}^{k_1k'q}_{ph\sigma_1\downarrow} \\
&+ \frac{1}{\beta N_c}\sum_{k_1\sigma_1}\tilde{\Gamma}^{kk_1q}_{ph\uparrow\sigma_1}G_{-\sigma_1}(-k_1)G_{-\sigma_1}(-k_1-q)(K^{k_1k'q}_{ph-\sigma_1\downarrow})^* \\
&+ \frac{1}{\beta N_c}\sum_{k_1\sigma_1}\tilde{\Gamma}^{kk_1q}_{ph\uparrow\sigma_1}F_{-\sigma_1}(-k_1)F^*_{-\sigma_1}(-k_1-q)\tilde{K}^{k_1k'q}_{ph\sigma_1\downarrow}
\end{aligned}
\tag{5.29}
$$

Eq. 5.26 and Eq. 5.27 can be decoupled analytically considering their sum and the difference respectively. The two decoupled equations are the density and the magnetic channel. And the four terms at right hand side of the equation can be rearranged into a block matrix multiplication form. Then the normal and anomalous full vertex function can be assembled together.

$$
\begin{pmatrix} K_{m,d} & \tilde{K}_{m,d} \\ \tilde{K}^*_{m,d} & K^*_{m,d} \end{pmatrix}^{kk'q} = \begin{pmatrix} \Gamma_{m,d} & \tilde{\Gamma}_{m,d} \\ \tilde{\Gamma}^*_{m,d} & \Gamma^*_{m,d} \end{pmatrix}^{kk'q}
$$
$$
+ \frac{1}{\beta N_c}\sum_{k_1}\begin{pmatrix} \Gamma_{m,d} & \tilde{\Gamma}_{m,d} \\ \tilde{\Gamma}^*_{m,d} & \Gamma^*_{m,d} \end{pmatrix}^{kk_1q}\begin{pmatrix} G(k_1)G(k_1+q) & F(k_1)^*F(k_1+q) \\ F(k_1)F(k_1+q)^* & G(-k_1)G(-k_1-q) \end{pmatrix}\begin{pmatrix} K_{m,d} & \tilde{K}_{m,d} \\ \tilde{K}^*_{m,d} & K^*_{m,d} \end{pmatrix}^{k_1k'q}
\tag{5.30}
$$

Or simply

$$
\underline{K}_{m,d} = \underline{\Gamma}_{m,d} + \frac{1}{\beta^2 N_c^2}\underline{\Gamma}_{m,d}\underline{\chi}_{0ph}\underline{K}_{m,d}
\tag{5.31}
$$

This equation can be used to solve for Γ by inversion of matrix with kk' as row and column index.

$$
\underline{\Gamma}_{m,d} = \sum_{k_1}\underline{K}^{kk_1q}_{m,d}[(\mathbb{I} + \frac{1}{\beta^2 N_c^2}\underline{\chi}_{0ph}\underline{K}_{m,d})^{-1}]^{k_1k'q}
\tag{5.32}
$$

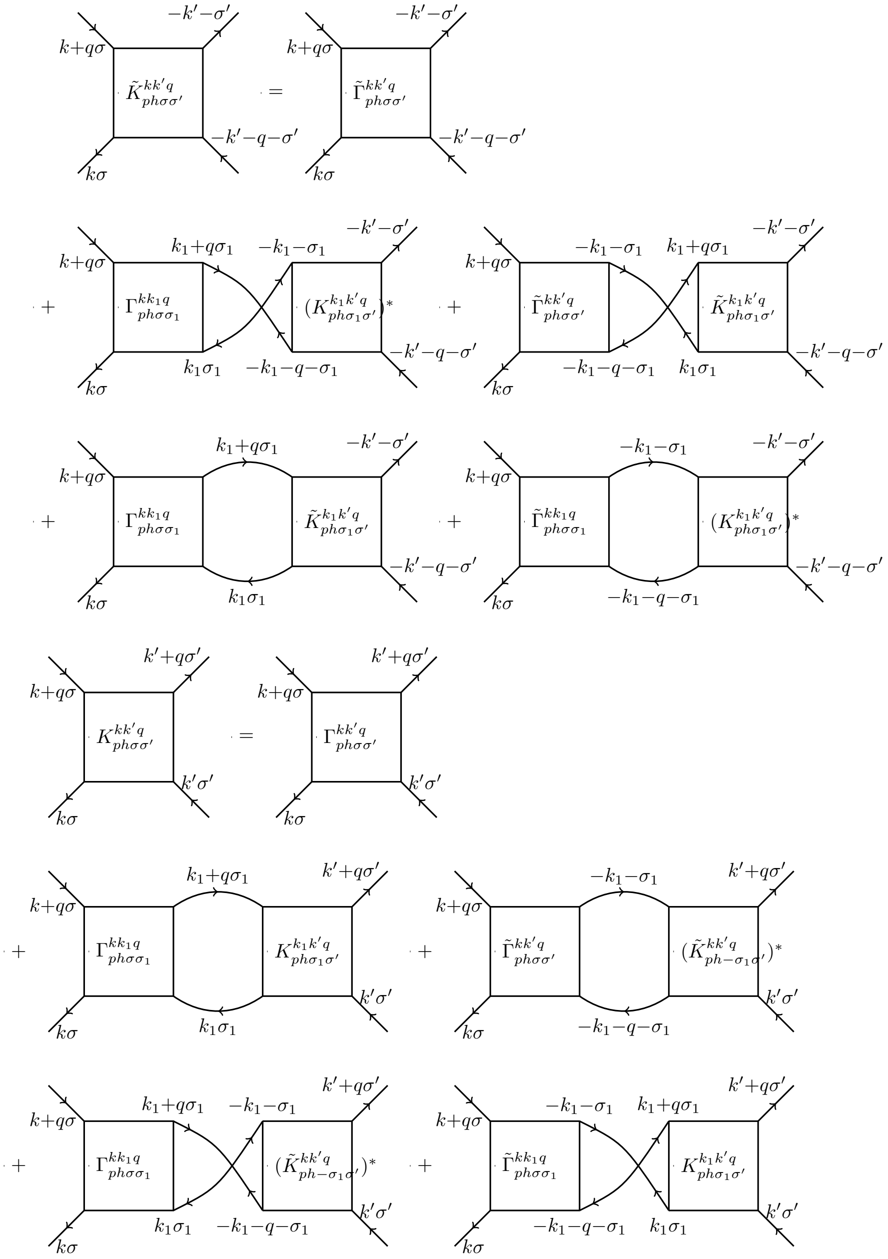

Figure 5.4: Upper: the diagram of normal full vertex in particle-hole channel. Lower: the diagram of anomalous full vertex in particle-hole channel.

Eq. 5.23 and Eq. 5.24 can be decoupled in the same way into magnetic and density channel.

Combine it with the definition of chi_0, we get

$$
\begin{aligned}
\begin{pmatrix} \chi_{m,d} & \tilde{\chi}_{m,d} \\ \tilde{\chi}^*_{m,d} & \chi^*_{m,d} \end{pmatrix}^{kk'q} &= \begin{pmatrix} \chi_{0ph} & \tilde{\chi}_{0ph} \\ \tilde{\chi}^*_{0ph} & \chi^*_{0ph} \end{pmatrix}^{kk'q} \\
-\frac{1}{\beta^2 N_c^2}\sum_{k_1} \begin{pmatrix} \chi_{0ph} & \tilde{\chi}_{0ph} \\ \tilde{\chi}^*_{0ph} & \chi^*_{0ph} \end{pmatrix}^{kk'q} & \begin{pmatrix} K_{m,d} & \tilde{K}_{m,d} \\ \tilde{K}^*_{m,d} & K^*_{m,d} \end{pmatrix}^{kk'q} \begin{pmatrix} \chi_{0ph} & \tilde{\chi}_{0ph} \\ \tilde{\chi}^*_{0ph} & \chi^*_{0ph} \end{pmatrix}^{kk'q}
\end{aligned}
\tag{5.33}
$$

Or simply

$$
\underline{\chi}_{m,d} = \underline{\chi}_{0ph} - \frac{1}{\beta^2 N_c^2}\underline{\chi}_{0ph}\underline{K}_{m,d}\underline{\chi}_{0ph} \tag{5.34}
$$

Combine the two matrix equations, we get the Bethe-Salpeter equation with Nambu formalism in the same format as that of non-superconducting state.

$$
\underline{\Gamma}_{m,d} = \beta^2 N_c^2 (\underline{\chi}^{-1}_{m,d} - \underline{\chi}^{-1}_{0ph}) \tag{5.35}
$$

5.5.2 particle-particle channel

For the three spin-combination in particle-particle channel, $\uparrow\uparrow$,$\uparrow\downarrow$ and $\overline{\uparrow\downarrow}$, $\uparrow\uparrow$ is obviously independent from the two other spin-combination. To spin-diagonalize the $\uparrow\downarrow$ and $\overline{\uparrow\downarrow}$, write down the Bethe-Salpeter equation in these two channels, both the normal vertex part and the anomalous vertex part.

$$\begin{aligned}K^{kk'q}_{pp\uparrow\downarrow} = \Gamma^{kk'q}_{pp\uparrow\downarrow} &+ \frac{1}{2\beta N_c}\sum_{k_1\sigma_1}\Gamma^{k_1k'q}_{pp\sigma_1\uparrow-\sigma_1\downarrow}G(k_1)G(q-k_1)K^{kk_1q}_{pp\uparrow-\sigma_1\downarrow\sigma_1}\\ &+ \frac{1}{2\beta N_c}\sum_{k_1\sigma_1}\Gamma^{k_1k'q}_{pp\sigma_1\uparrow-\sigma_1\downarrow}F(k_1)F(q-k_1)(\tilde{K}^{kk_1q}_{pp\downarrow\sigma_1\uparrow-\sigma_1})^*\\ &+ \frac{1}{2\beta N_c}\sum_{k_1\sigma_1}\Gamma^{k_1k'q}_{pp-\sigma_1\uparrow\sigma_1\downarrow}F^*(k_1)F^*(q-k_1)K^{kk_1q}_{pp\uparrow-\sigma_1\downarrow\sigma_1}\\ &+ \frac{1}{2\beta N_c}\sum_{k_1\sigma_1}\tilde{\Gamma}^{k_1k'q}_{pp-\sigma_1\uparrow\sigma_1\downarrow}G(-k_1)G(-q+k_1)(\tilde{K}^{kk_1q}_{pp\downarrow-\sigma_1\uparrow\sigma_1})^*\end{aligned}\tag{5.36}$$

$$\begin{aligned}\tilde{K}^{kk'q}_{pp\uparrow\downarrow} = \tilde{\Gamma}^{kk'q}_{pp\uparrow\downarrow} &+ \frac{1}{2\beta N_c}\sum_{k_1\sigma_1}\Gamma^{k_1k'q}_{pp\sigma_1\uparrow-\sigma_1\downarrow}F(k_1)F(q-k_1)(K^{kk_1q}_{pp\uparrow-\sigma_1\downarrow\sigma_1})^*\\ &+ \frac{1}{2\beta N_c}\sum_{k_1\sigma_1}\Gamma^{k_1k'q}_{pp\sigma_1\uparrow-\sigma_1\downarrow}G(k_1)G(q-k_1)\tilde{K}^{kk_1q}_{pp\downarrow-\sigma_1\uparrow\sigma_1}\\ &+ \frac{1}{2\beta N_c}\sum_{k_1\sigma_1}\tilde{\Gamma}^{k_1k'q}_{pp-\sigma_1\uparrow\sigma_1\downarrow}G(-k_1)G(-q+k_1)(K^{kk_1q}_{pp\uparrow-\sigma_1\downarrow\sigma_1})^*\\ &+ \frac{1}{2\beta N_c}\sum_{k_1\sigma_1}\tilde{\Gamma}^{k_1k'q}_{pp-\sigma_1\uparrow\sigma_1\downarrow}F^*(k_1)F^*(q-k_1)\tilde{K}^{kk_1q}_{pp\downarrow-\sigma_1\uparrow\sigma_1}\end{aligned}\tag{5.37}$$

$$\begin{aligned}K^{kk'q}_{pp\overline{\uparrow\downarrow}} = \Gamma^{kk'q}_{pp\overline{\uparrow\downarrow}} &+ \frac{1}{2\beta N_c}\sum_{k_1\sigma_1}\Gamma^{k_1k'q}_{pp\sigma_1\downarrow-\sigma_1\uparrow}G(k_1)G(q-k_1)K^{kk_1q}_{pp\uparrow-\sigma_1\downarrow\sigma_1}\\ &+ \frac{1}{2\beta N_c}\sum_{k_1\sigma_1}\Gamma^{k_1k'q}_{pp\sigma_1\downarrow-\sigma_1\uparrow}F(k_1)F(q-k_1)(\tilde{K}^{kk_1q}_{pp\downarrow\sigma_1\uparrow-\sigma_1})^*\\ &+ \frac{1}{2\beta N_c}\sum_{k_1\sigma_1}\Gamma^{k_1k'q}_{pp-\sigma_1\downarrow\sigma_1\uparrow}F^*(k_1)F^*(q-k_1)K^{kk_1q}_{pp\uparrow-\sigma_1\downarrow\sigma_1}\\ &+ \frac{1}{2\beta N_c}\sum_{k_1\sigma_1}\tilde{\Gamma}^{k_1k'q}_{pp-\sigma_1\downarrow\sigma_1\uparrow}G(-k_1)G(-q+k_1)(\tilde{K}^{kk_1q}_{pp\downarrow-\sigma_1\uparrow\sigma_1})^*\end{aligned}\tag{5.38}$$

$$
\begin{aligned}
\tilde{K}^{kk'q}_{pp\overline{\uparrow\downarrow}} = \tilde{\Gamma}^{kk'q}_{pp\overline{\uparrow\downarrow}} &+ \frac{1}{2\beta N_c}\sum_{k_1\sigma_1}\Gamma^{k_1k'q}_{pp\sigma_1\downarrow-\sigma_1\uparrow}F(k_1)F(q-k_1)(K^{kk_1q}_{pp\uparrow-\sigma_1\downarrow\sigma_1})^* \\
&+ \frac{1}{2\beta N_c}\sum_{k_1\sigma_1}\Gamma^{k_1k'q}_{pp\sigma_1\downarrow-\sigma_1\uparrow}G(k_1)G(q-k_1)\tilde{K}^{kk_1q}_{pp\downarrow-\sigma_1\uparrow\sigma_1} \\
&+ \frac{1}{2\beta N_c}\sum_{k_1\sigma_1}\tilde{\Gamma}^{k_1k'q}_{pp-\sigma_1\downarrow\sigma_1\uparrow}G(-k_1)G(-q+k_1)(K^{kk_1q}_{pp\uparrow-\sigma_1\downarrow\sigma_1})^* \\
&+ \frac{1}{2\beta N_c}\sum_{k_1\sigma_1}\tilde{\Gamma}^{k_1k'q}_{pp-\sigma_1\downarrow\sigma_1\uparrow}F^*(k_1)F^*(q-k_1)\tilde{K}^{kk_1q}_{pp\downarrow-\sigma_1\uparrow\sigma_1}
\end{aligned}
\tag{5.39}
$$

The $\frac{1}{2}$ factor is used to avoid double counting, since we sum over all $k_1\sigma_1$. $pp\uparrow\downarrow$ and $pp\overline{\uparrow\downarrow}$ are entangled in the same way as $ph\uparrow\downarrow$ and $ph\uparrow\uparrow$, so they can also be decoupled by the sum and difference of equation Eq. 5.36, Eq. 5.37, Eq. 5.38 and Eq. 5.39

$$
\begin{aligned}
&\begin{pmatrix} K_t & \tilde{K}_t \\ \tilde{K}^*_t & K^*_t \end{pmatrix}^{kk'q} = \begin{pmatrix} \Gamma_t & \tilde{\Gamma}_t \\ \tilde{\Gamma}^*_t & \Gamma^*_t \end{pmatrix}^{kk'q} \\
&+ \frac{1}{2\beta N_c}\sum_{k_1}\begin{pmatrix} \Gamma_t & \tilde{\Gamma}_t \\ \tilde{\Gamma}^*_t & \Gamma^*_t \end{pmatrix}^{k_1k'q}\begin{pmatrix} G(k_1)G(q-k_1) & F(k_1)F(q-k_1) \\ F^*(k_1)F^*(q-k_1) & G(-k_1)G(-(q-k_1)) \end{pmatrix}\begin{pmatrix} K_t & \tilde{K}_t \\ \tilde{K}^*_t & K^*_t \end{pmatrix}^{kk_1q}
\end{aligned}
\tag{5.40}
$$

and

$$
\begin{aligned}
&\begin{pmatrix} K_s & \tilde{K}_s \\ \tilde{K}^*_s & K^*_s \end{pmatrix}^{kk'q} = \begin{pmatrix} \Gamma_s & \tilde{\Gamma}_s \\ \tilde{\Gamma}^*_s & \Gamma^*_s \end{pmatrix}^{kk'q} \\
&- \frac{1}{2\beta N_c}\sum_{k_1}\begin{pmatrix} \Gamma_s & \tilde{\Gamma}_s \\ \tilde{\Gamma}^*_s & \Gamma^*_s \end{pmatrix}^{k_1k'q}\begin{pmatrix} G(k_1)G(q-k_1) & F(k_1)F(q-k_1) \\ F^*(k_1)F^*(q-k_1) & G(-k_1)G(-(q-k_1)) \end{pmatrix}\begin{pmatrix} K_s & \tilde{K}_s \\ \tilde{K}^*_s & K^*_s \end{pmatrix}^{kk_1q}
\end{aligned}
\tag{5.41}
$$

Or simply

$$\underline{K}_t = \underline{\Gamma}_t - \frac{1}{2\beta^2 N_c^2} \underline{\Gamma}_t \underline{\chi}_{0pp} \underline{K}_t \tag{5.42}$$

and

$$\underline{K}_s = \underline{\Gamma}_s + \frac{1}{2\beta^2 N_c^2} \underline{\Gamma}_s \underline{\chi}_{0pp} \underline{K}_s \tag{5.43}$$

where the bubble in pp channel is

$$\underline{\chi}_{0pp}^{kk'q} = -\beta N_c \delta_{kk'} \begin{pmatrix} \underline{G}_{00}(k)\underline{G}_{00}(q-k) & \underline{G}_{01}(k)\underline{G}_{01}(q-k) \\ \underline{G}_{10}(k)\underline{G}_{10}(q-k) & \underline{G}_{11}(k)\underline{G}_{11}(q-k) \end{pmatrix} \tag{5.44}$$

To connect χ_0 and K in the $pp\uparrow\downarrow$ and $pp\overline{\uparrow\downarrow}$ channel, the diagrams are shown in Fig. 5.6. It reads

$$\begin{aligned} \chi_{pp\overline{\uparrow\downarrow}} = -\beta N_c G(k)G(q-k)\delta_{kk'} &- G(k')G(q-k')K^{kk'q}_{pp\overline{\uparrow\downarrow}}G(k)G(q-k) \\ &- G(k')G(q-k')\tilde{K}^{kk'q}_{pp\overline{\uparrow\downarrow}}F^*(k)F^*(q-k) \\ &- F(k')F(q-k')(K^{kk'q}_{pp\overline{\uparrow\downarrow}})^*F^*(k)F^*(q-k) \\ &- F(k')F(q-k')(\tilde{K}^{kk'q}_{pp\overline{\uparrow\downarrow}})^*G(k)G(q-k) \end{aligned} \tag{5.45}$$

$$\begin{aligned} \tilde{\chi}_{pp\overline{\uparrow\downarrow}} = -\beta N_c F(k)F(q-k)\delta_{kk'} &- G(k')G(q-k')\tilde{K}^{kk'q}_{pp\overline{\uparrow\downarrow}}G(-k)G(-(q-k)) \\ &- G(k')G(q-k')K^{kk'q}_{pp\overline{\uparrow\downarrow}}F(k)F(q-k) \\ &- F(k')F(q-k')(\tilde{K}^{kk'q}_{pp\overline{\uparrow\downarrow}})^*F(k)F(q-k) \\ &- F(k')F(q-k')(K^{kk'q}_{pp\overline{\uparrow\downarrow}})^*G(-k)G(-(q-k)) \end{aligned} \tag{5.46}$$

$pp\uparrow\downarrow$ channel has almost the same diagram. The two differences are: (1) the bubble terms in both normal and anomalous χ vanish; (2) the spins on the left-most part of each diagram flip. Therefore,

$$\underline{\chi}_t = \underline{\chi}_{0pp} - \frac{1}{\beta^2 N_c^2}\underline{\chi}_{0pp}\underline{K}_t\underline{\chi}_{0pp} \tag{5.47}$$

and

$$\underline{\chi}_s = -\underline{\chi}_{0pp} - \frac{1}{\beta^2 N_c^2}\underline{\chi}_{0pp}\underline{K}_s\underline{\chi}_{0pp} \tag{5.48}$$

Combining the two matrix equations, we get the Bethe-Salpeter equation with Nambu formalism in the same format as that of non-superconducting state.

$$\underline{\Gamma}_t = \beta^2 N_c^2[4(\underline{\chi}_t + \underline{\chi}_{0pp})^{-1} - 2\underline{\chi}_{0pp}^{-1}) \tag{5.49}$$

and

$$\underline{\Gamma}_s = \beta^2 N_c^2[4(\underline{\chi}_s - \underline{\chi}_{0pp})^{-1} + 2\underline{\chi}_{0pp}^{-1}) \tag{5.50}$$

As has been discussed in chapter 2, within DCA approximation, $\Gamma_{cluster} = \Gamma_{lattice}$. So the lattice susceptibility and the cluster susceptibility are connected by the Bethe-Salpeter equation as

$$\underline{\chi}_l^{-1} - \underline{\chi}_{0l}^{-1} = \underline{\chi}_c^{-1} - \underline{\chi}_{0c}^{-1} \tag{5.51}$$

where the subscript l means lattice and c means cluster. This relation holds for every spin-independent channel, such as $d-$, $m-$, $s-$, $t-$, $pp \uparrow\uparrow -$ channel.

5.6 Equation of Motion

The self-energy describes all scattering effects of electron originated from Coulomb interaction in the correlated systems. When the interaction is purely local, the self-energy is connected to the full vertex by Dyson-schwinger equation of motion [108]

$$\Sigma(k) = \frac{Un}{2} - \frac{U}{\beta^2 N}\sum_{k'q} F_{\uparrow\downarrow}(k,k',q)G(k')G(k'+q)G(k+q) \tag{5.52}$$

This equation can be extended to the Nambu formalism as shown in Fig. 5.7 [192]. The mathematical expressions are

$$\begin{aligned}
\Sigma(k) = \Sigma_H(k) &- \frac{U}{\beta^2 N_c^2}\sum_{k'q} K_{ph\uparrow\downarrow}(k,k',q)G(k+q)G(k')G(k'+q) \\
&- \frac{U}{\beta^2 N_c^2}\sum_{k'q} K_{ph\uparrow\downarrow}(k,k',q)G(k+q)F^*(k')F(k'+q) \\
&- \frac{U}{\beta^2 N_c^2}\sum_{k'q} \tilde{K}_{ph\uparrow\downarrow}(k,k',q)G(k+q)G(-k')G(-k'-q) \\
&- \frac{U}{\beta^2 N_c^2}\sum_{k'q} \tilde{K}_{ph\uparrow\downarrow}(k,k',q)G(k+q)F(k')F^*(k'+q)
\end{aligned} \tag{5.53}$$

$$\begin{aligned}
\tilde{\Sigma}(k) = \tilde{\Sigma}_H(k) &- \frac{U}{\beta^2 N}\sum_{k'q} K_{ph\uparrow\downarrow}(k,k',q)F^*(k+q)G(k')G(k'+q) \\
&- \frac{U}{\beta^2 N}\sum_{k'q} K_{ph\uparrow\downarrow}(k,k',q)F^*(k'+q)F^*(k')F(k'+q) \\
&- \frac{U}{\beta^2 N}\sum_{k'q} \tilde{K}_{ph\uparrow\downarrow}(k,k',q)F^*(k+q)G(-k')G(-k'-q) \\
&- \frac{U}{\beta^2 N}\sum_{k'q} \tilde{K}_{ph\uparrow\downarrow}(k,k',q)F^*(k+q)F(k')F^*(k'+q)
\end{aligned} \tag{5.54}$$

where Σ_H and $\tilde{\Sigma}_H$ are the Hatree term. Recall that $K_m = K_{ph\uparrow\uparrow} - K_{ph\uparrow\downarrow}$ and $K_d = K_{ph\uparrow\uparrow} + K_{ph\uparrow\downarrow}$.

In $pp-$ channel, the Dyson-Schwinger equations are

$$\begin{aligned}\Sigma(k) = \Sigma_H(k) &- \frac{U}{\beta^2 N_c^2}\sum_{k'q} K_{pp\uparrow\downarrow}(k,k',q)G(k')G(q-k')G(k)\\ &- \frac{U}{\beta^2 N_c^2}\sum_{k'q} K_{pp\uparrow\downarrow}(k,k',q)G(k')G(q-k')G(q-k)\\ &- \frac{U}{\beta^2 N_c^2}\sum_{k'q}(\tilde{K}_{pp\uparrow\downarrow}(k,k',q))^* G(-k')F(q-k')F(q-k)\\ &- \frac{U}{\beta^2 N_c^2}\sum_{k'q}(\tilde{K}_{pp\uparrow\downarrow}(k,k',q))^* F^*(k')F(q-k')G(q-k)\end{aligned}\tag{5.55}$$

$$\begin{aligned}\tilde{\Sigma}(k) = \tilde{\Sigma}_H(k) &- \frac{U}{\beta^2 N^2}\sum_{k'q} \tilde{K}_{pp\uparrow\downarrow}(k,k',q)G(k')G(q-k')F^*(q-k)\\ &- \frac{U}{\beta^2 N_c^2}\sum_{k'q}(K_{pp\uparrow\downarrow}(k,k',q))^* G(-k')F(q-k')G(-(q-k))\\ &- \frac{U}{\beta^2 N_c^2}\sum_{k'q} \tilde{K}_{pp\uparrow\downarrow}(k,k',q)F^*(k')G(q-k')G(-(q-k))\\ &- \frac{U}{\beta^2 N_c^2}\sum_{k'q}(K_{pp\uparrow\downarrow}(k,k',q))^* F(k')F(q-k')F^*(q-k)\end{aligned}\tag{5.56}$$

Their diagrammatic forms are plotted in Fig. 5.8

5.7 Knight Shift

The first cuprates Knight shift measurement below T_c (Fig. 5.9) was carried out by M.Takigawa *et al.*[16] with a standard pulsed spectrometer and fine powder $YBa_2Cu_3O_7$. The observed Knight shift is composed of two part, contributions from spin and orbital magnetization. $K = K_{orb} + K_{spin}$. K_{spin}, similar to the case in normal state, is proportional to the static spin susceptibility. K_{orb} is a almost a constant below and above critical temperature. For our 2D Hubbard model, the simulated Knight shift is K_{ab} for planar Cu(2), when the diamagnetic correction is very small. The Hubbard model excludes the effect of spin-orbit scattering, the simulated Knight shift is $K_s = K_{spin} \propto \chi_m(\boldsymbol{Q} = 0, \nu = 0)$ They were followed by S. E. Barrett [203], who used ^{89}Y NMR resonance line to measure the field inside the sample. The results from both groups show a steep slope around $T = T_c$, much steeper than what weak-coupling s-wave Yosida function [204] would predict. That is, the conventional BCS model is not appropriate for modeling the planar Cu nuclei arrays in high T_c cuprates.

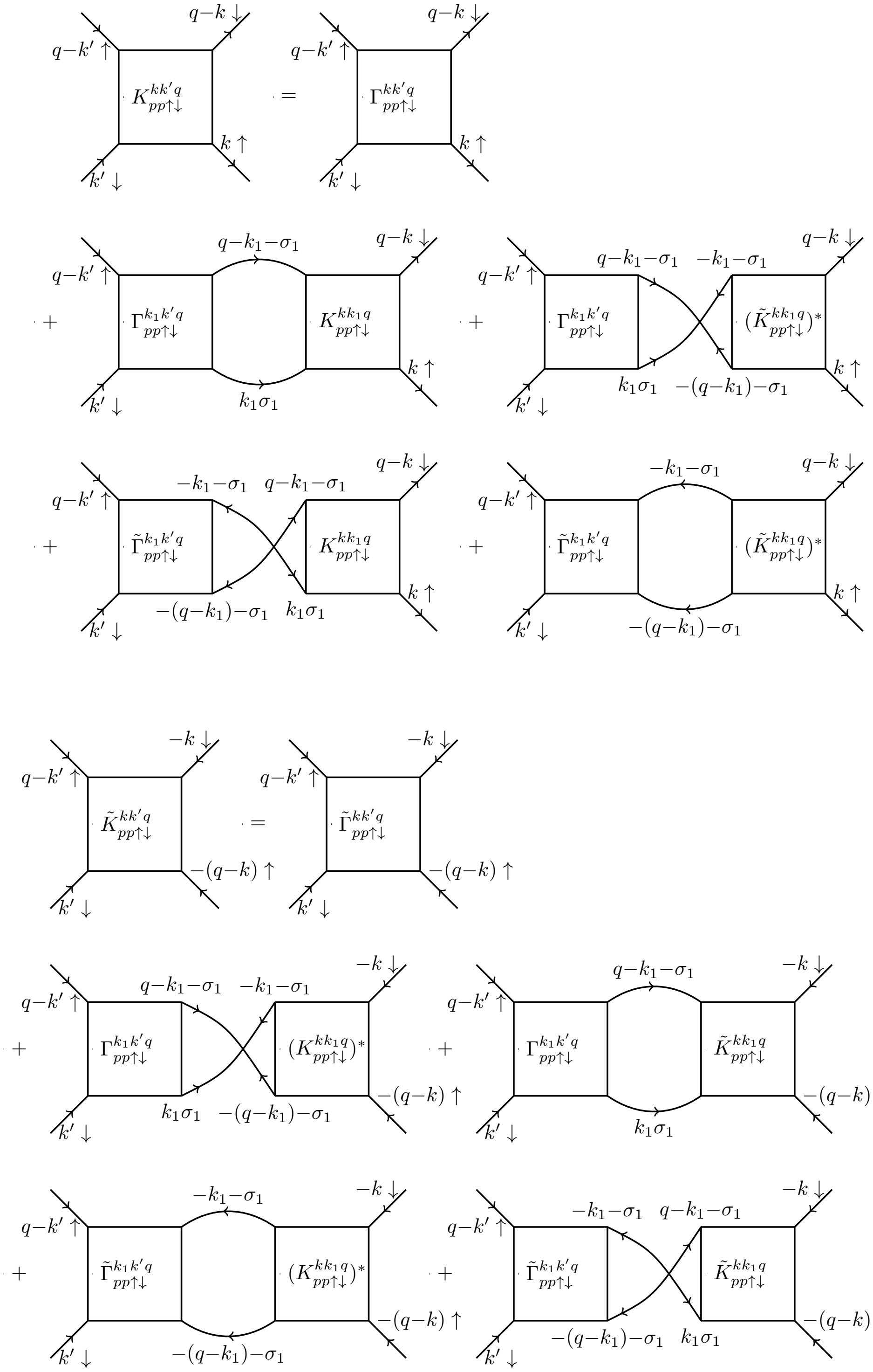

Figure 5.5: Upper: the diagram of normal full vertex in particle-particle channel. Lower: the diagram of anomalous full vertex in particle-particle channel.

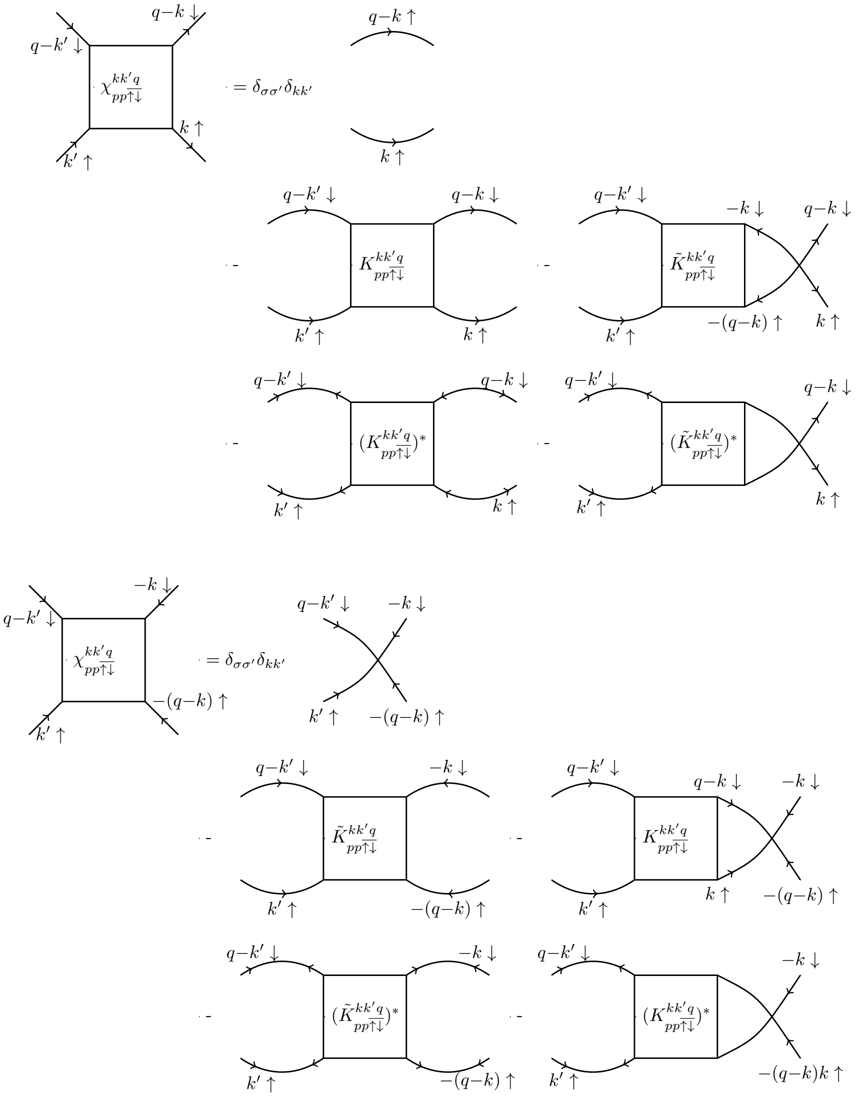

Figure 5.6: The diagram of the definition of full vertex in particle-particle channel in $pp\overline{\uparrow\downarrow}$ spin-combination.

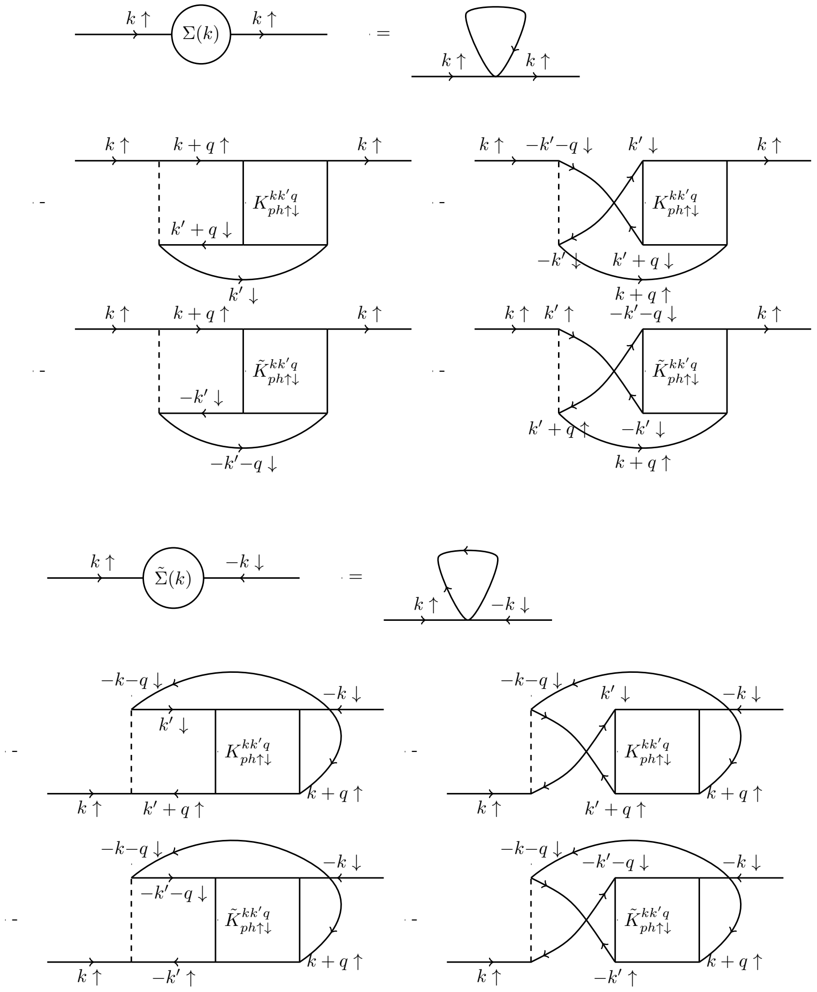

Figure 5.7: The diagram of equation of motion in $ph-$channel.

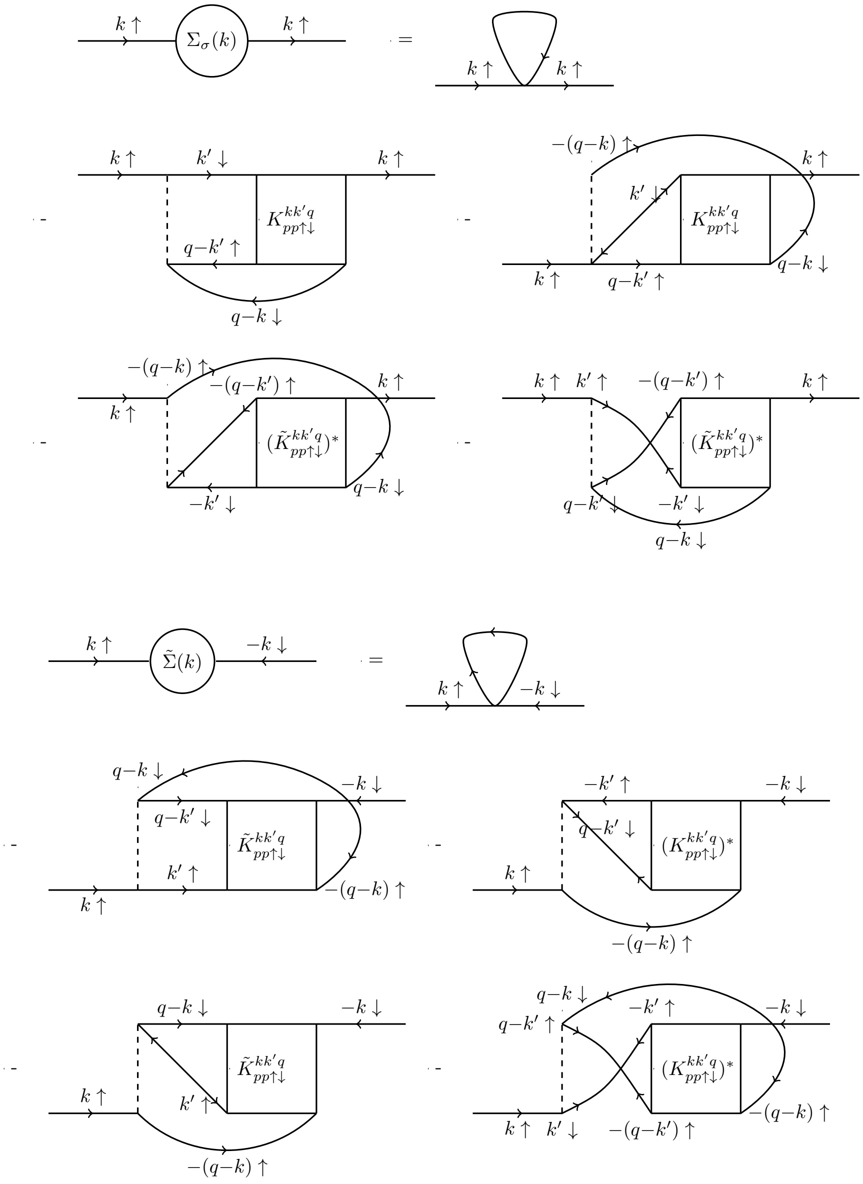

Figure 5.8: The diagram of equation of motion in $pp-$channel.

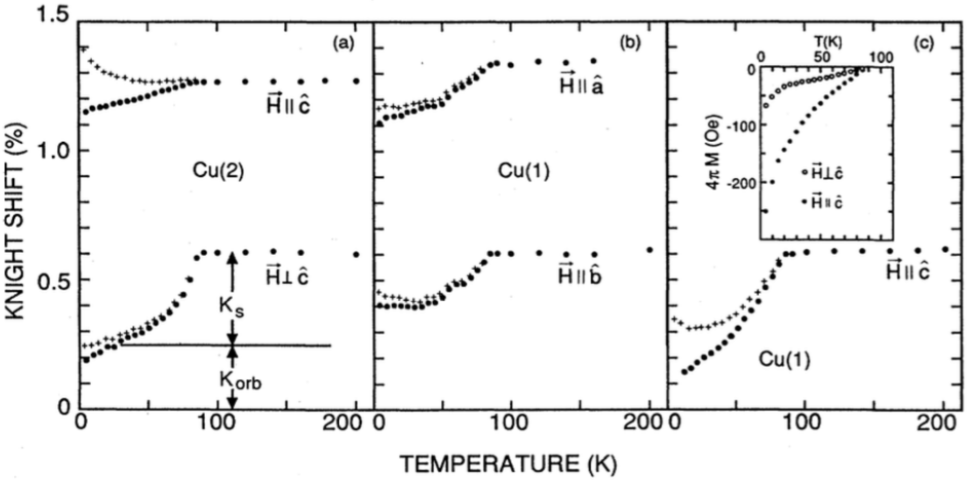

Figure 5.9: The temperature dependence of the Knight shift of chain Cu(1) and planar Cu(2) nuclei in $YBa_2Cu_3O_7$ with different field orientations. The crosses and filled circles are the results with and without diamagnetic field correction, respectively. Panel(c) inset: magnetization at the same field. Figure reproduced from Ref. [16]

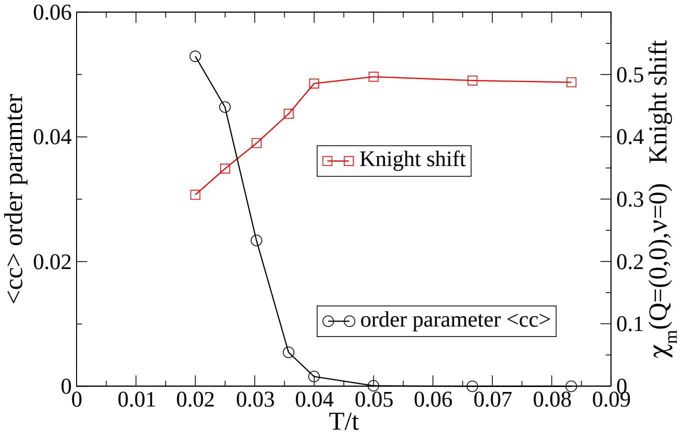

Figure 5.10: Red solid line, square symbol: the Knight shift with temperature range extending into superconducting states. Black solid line, circle symbol: order parameter $F = \langle T c_\uparrow c_\downarrow \rangle$. Data obtained using $U = 6t$, $t' = 0$, 8 site cluster, DCA calculation.

CHAPTER 6

Conclusion

In this thesis we have studied a strongly correlated electron model, the two dimensional Hubbard Model, which is considered to embody the essential physics of high temperature superconducting materials (Chap. 1 Sec. 1.2, Sec. 1.3). To solve this model, we used the extension of dynamical mean-field theory (DMFT), the dynamical cluster extension (DCA) and continuous time auxiliary field impurity solver (CTAUX). DCA is a non-perturbative method that treat short range correlations exactly and long range interactions in a mean-field way. It has been proved to be a powerful tool for strongly correlated systems.

While most DMFT studies hitherto have focused on one-particle properties, valuable information is also enclosed in two-particle quantities, like dynamical susceptibility and vertex functions. Our main achievements is the calculation of two-particle response functions in strongly correlated electron systems using non-perturbative methods. Two applications of the calculation of two-particle quantities in non-superconducting state are shown in Chap. 3 and Chap. 4, concerning the dynamical magnetic susceptibility and superconducting pairing susceptibility .

In Chap. 3, we discovered that the correlated pairing susceptibility $\chi - \chi_0$ is a good indicator for the vicinity of parameters for optimal superconductivity transition temperature at much higher temperature than T_c. This provide us an approach to sweep over the entirety of the phase space with much smaller computational burden and less severe sign problem. Using this method, we have explored the susceptibility of the Hubbard model towards superconducting order over large range of interaction and doping, also for different next-nearest-neighbor hopping parameter t' and symmetries. We find that both weak and strong interaction regimes, as well as low doping and half filled regimes, are non- optimal for superconducting fluctuations. For non-zero t' we find a shift of the optimal superconducting features to the electron doped side of the phase diagram, due to the establishment of a competing pseudo-gap on the hole doped side. These results can give experimentalists thoughts and guidance of synthesizing new high T_c materials.

In Chap. 4, we make use of the other channel of the general susceptibility, the magnetic channel. We show simulated results for the doping and temperature evolution of the Knight shift, the relaxation time, and the spin echo decay time in the pseudo-gap regime of the two-dimensional Hubbard model and compare them to the NMR experiment of high T_c cuprates. These calculations show trends in temperature and doping evolution that are in remarkable agreement with experiment on single layer compounds. This consistency suggests that the salient aspects of the physics of the cuprate pseudo-gap are contained within the simple single-orbital Hubbard model.

In Chap. 5, we derived equations to obtain the two-particle quantities with Nambu formalism. The approach has been presented in great details. The goal was to extract the dynamical susceptibilities of the lattice system from the two-particle Green's function obtained by the impurity solver. This is essential for the analysis of simulating the NMR experiments under superconducting critical temperature and may also find its application in the diagnostic of fluctuations.

BIBLIOGRAPHY

[1] Mitchell, J. F., Argyriou, D. N., Berger, A., Gray, K. E., Osborn, R., and Welp, U., "Spin, Charge, and Lattice States in Layered Magnetoresistive Oxides," *The Journal of Physical Chemistry B*, Vol. 105, No. 44, 2001, pp. 10731–10745.

[2] Nakatsuji, S. and Maeno, Y., "Quasi-Two-Dimensional Mott Transition System $\mathrm{Ca}_{2-x}\mathrm{Sr}_x\mathrm{RuO}_4$," *Phys. Rev. Lett.*, Vol. 84, Mar 2000, pp. 2666–2669.

[3] Nakatsuji, S., Dobrosavljević, V., Tanasković, D., Minakata, M., Fukazawa, H., and Maeno, Y., "Mechanism of Hopping Transport in Disordered Mott Insulators," *Phys. Rev. Lett.*, Vol. 93, Sep 2004, pp. 146401.

[4] Foo, M. L., Wang, Y., Watauchi, S., Zandbergen, H. W., He, T., Cava, R. J., and Ong, N. P., "Charge Ordering, Commensurability, and Metallicity in the Phase Diagram of the Layered $\mathrm{Na}_x\mathrm{CoO}_2$," *Phys. Rev. Lett.*, Vol. 92, Jun 2004, pp. 247001.

[5] Limelette, P., Wzietek, P., Florens, S., Georges, A., Costi, T. A., Pasquier, C., Jérome, D., Mézière, C., and Batail, P., "Mott Transition and Transport Crossovers in the Organic Compound $\kappa{-}(\mathrm{BEDT}{-}\mathrm{TTF})_2\mathrm{Cu}[\mathrm{N}(\mathrm{CN})_2]\mathrm{Cl}$," *Phys. Rev. Lett.*, Vol. 91, Jul 2003, pp. 016401.

[6] Dagotto, E., *Complexity in Strongly Correlated Electronic Systems*, Vol. 309, American Association for the Advancement of Science, 2005.

[7] wikimedia commons.

[8] Plakida, N., *High-Temperature Cuprate Superconductors Experiment, Theory, and Applications*, Springer-Verlag Berlin Heidelberg, 2010.

[9] Timusk, T. and Statt, B., "The pseudogap in high-temperature superconductors: an experimental survey," *Reports on Progress in Physics*, Vol. 62, No. 1, 1999, pp. 61.

[10] Andreas Erb, Michael Lambacher, A. H. and Gross, R.

[11] Rohringer, G., Valli, A., and Toschi, A., "Local electronic correlation at the two-particle level," *Phys. Rev. B*, Vol. 86, No. 12, Sept. 2012, pp. 125114.

[12] Gull, E., Parcollet, O., and Millis, A. J., "Superconductivity and the Pseudogap in the Two-Dimensional Hubbard Model," *Phys. Rev. Lett.*, Vol. 110, May 2013, pp. 216405.

[13] Hüfner, S., Hossain, M. A., Damascelli, A., and Sawatzky, G. A., "Two gaps make a high-temperature superconductor?" *Reports on Progress in Physics*, Vol. 71, No. 6, 2008, pp. 062501.

[14] Walstedt, R. E., *The NMR probe of high-Tc materials*, Springer, Berlin New York, 2008.

[15] Berthier, C., Julien, M. H., Horvatić, M., and Berthier, Y., "NMR Studies of the Normal State of High Temperature Superconductors," *Journal de Physique I*, Vol. 6, Dec. 1996, pp. 2205–2236.

[16] Takigawa, M., Hammel, P. C., Heffner, R. H., and Fisk, Z., "Spin susceptibility in superconducting $\mathrm{YBa_2Cu_3O_7}$ from $^{63}\mathrm{Cu}$ Knight shift," *Phys. Rev. B*, Vol. 39, Apr 1989, pp. 7371–7374.

[17] Millis, A. J., "Lecture notes on "Strongly Correlated" Transition Metal Oxides," Lecture Notes, 2012.

[18] Coleman, P., *Heavy Fermions: Electrons at the Edge of Magnetism*, John Wiley and Sons, Ltd, 2007.

[19] Salamon, M. B. and Jaime, M., "The physics of manganites: Structure and transport," *Rev. Mod. Phys.*, Vol. 73, Aug 2001, pp. 583–628.

[20] Ishiguro, T., Yamaji, K., and Saito, G., *Organic Superconductors (Springer Series in Solid-State Sciences)*, Springer, 2013.

[21] Ando, T., Fowler, A. B., and Stern, F., "Electronic properties of two-dimensional systems," *Rev. Mod. Phys.*, Vol. 54, Apr 1982, pp. 437–672.

[22] Kotliar, G. and Vollhardt, D., "Strongly Correlated Materials: Insights From Dynamical Mean-Field Theory," *Physics Today*, Vol. 57, No. 3, 2004, pp. 53–59.

[23] Gastiasoro, M. N. and Andersen, B. M., "Competing magnetic double-Q phases and superconductivity-induced reentrance of C_2 magnetic stripe order in iron pnictides," *Phys. Rev. B*, Vol. 92, Oct 2015, pp. 140506.

[24] Aarnink, R. and Overweg, J., "Magnetic Resonance Imaging, a success story for superconductivity," *Europhysics News*, Vol. 43, July-August 2012, pp. 26–29.

[25] Schmser, P., "Superconductivity in high energy particle accelerators," *Progress in Particle and Nuclear Physics*, Vol. 49, No. 1, 2002, pp. 155 – 244.

[26] Sorbom, B., Ball, J., Palmer, T., Mangiarotti, F., Sierchio, J., Bonoli, P., Kasten, C., Sutherland, D., Barnard, H., Haakonsen, C., Goh, J., Sung, C., and Whyte, D., "ARC: A compact, high-field, fusion nuclear science facility and demonstration power plant with demountable magnets," *Fusion Engineering and Design*, Vol. 100, 2015, pp. 378 – 405.

[27] Thomas Brückel, G., *Neutron Scattering Lectures of the JCNS Laborator Course held at Forschungszentrum Jülich and the research reactor FRM II of TU Munich In cooperation with RWTH Aachen and University of Münster*, Schriften des Forschungszentrums Jülich: Reihe Schlüsseltechnologien, Forschungszentrum Jülich, 2012.

[28] Vicsek, T., "Complexity: The bigger picture," *Nature*, Vol. 418, No. 6894, 07 2002, pp. 131–131.

[29] Lee, P. A., Nagaosa, N., and Wen, X.-G., "Doping a Mott insulator: Physics of high-temperature superconductivity," *Rev. Mod. Phys.*, Vol. 78, Jan 2006, pp. 17–85.

[30] Lee, P. A. and Wen, X.-G., "Unusual Superconducting State of Underdoped Cuprates," *Phys. Rev. Lett.*, Vol. 78, May 1997, pp. 4111–4114.

[31] "Towards a complete theory of high Tc," *Nat Phys*, Vol. 2, No. 3, Mar 2006, pp. 138–143.

[32] Loh, E. Y., Gubernatis, J. E., Scalettar, R. T., White, S. R., Scalapino, D. J., and Sugar, R. L., "Sign problem in the numerical simulation of many-electron systems," *Phys. Rev. B*, Vol. 41, May 1990, pp. 9301–9307.

[33] Shi, H. and Zhang, S., "Infinite variance in fermion quantum Monte Carlo calculations," *Phys. Rev. E*, Vol. 93, Mar 2016, pp. 033303.

[34] Shi, H. and Zhang, S., "Symmetry in auxiliary-field quantum Monte Carlo calculations," *Phys. Rev. B*, Vol. 88, Sep 2013, pp. 125132.

[35] Prokof'ev, N. V. and Svistunov, B. V., "Polaron Problem by Diagrammatic Quantum Monte Carlo," *Phys. Rev. Lett.*, Vol. 81, Sep 1998, pp. 2514–2517.

[36] Mishchenko, A. S., Prokof'ev, N. V., Sakamoto, A., and Svistunov, B. V., "Diagrammatic quantum Monte Carlo study of the Fröhlich polaron," *Phys. Rev. B*, Vol. 62, Sep 2000, pp. 6317–6336.

[37] Houcke, K. V., Kozik, E., Prokof'ev, N., and Svistunov, B., "Diagrammatic Monte Carlo," *Physics Procedia*, Vol. 6, 2010, pp. 95 – 105.

[38] Rubtsov, A. N., Katsnelson, M. I., and Lichtenstein, A. I., "Dual fermion approach to nonlocal correlations in the Hubbard model," *Phys. Rev. B*, Vol. 77, Jan 2008, pp. 033101.

[39] Knizia, G. and Chan, G. K.-L., "Density Matrix Embedding: A Simple Alternative to Dynamical Mean-Field Theory," *Phys. Rev. Lett.*, Vol. 109, Nov 2012, pp. 186404.

[40] Knizia, G. and Chan, G. K.-L., "Density Matrix Embedding: A Strong-Coupling Quantum Embedding Theory," *Journal of Chemical Theory and Computation*, Vol. 9, No. 3, 2013, pp. 1428–1432, PMID: 26587604.

[41] White, S. R., "Density matrix formulation for quantum renormalization groups," *Phys. Rev. Lett.*, Vol. 69, Nov 1992, pp. 2863–2866.

[42] White, S. R., "Density-matrix algorithms for quantum renormalization groups," *Phys. Rev. B*, Vol. 48, Oct 1993, pp. 10345–10356.

[43] Maier, T., Jarrell, M., Pruschke, T., and Hettler, M. H., "Quantum cluster theories," *Rev. Mod. Phys.*, Vol. 77, 2005, pp. 1027–1080.

[44] Gros, C., "Superconductivity in correlated wave functions," *Phys. Rev. B*, Vol. 38, Jul 1988, pp. 931–934.

[45] Yokoyama, H. and Shiba, H., "Variational Monte-Carlo Studies of Hubbard Model. II," *Journal of the Physical Society of Japan*, Vol. 56, No. 10, 1987, pp. 3582–3592.

[46] Bartlett, R. J. and Musial, M., "Coupled-cluster theory in quantum chemistry," *Rev. Mod. Phys.*, Vol. 79, Feb 2007, pp. 291–352.

[47] Rodríguez-Guzmán, R., Schmid, K. W., Jiménez-Hoyos, C. A., and Scuseria, G. E., "Symmetry-projected variational approach for ground and excited states of the two-dimensional Hubbard model," *Phys. Rev. B*, Vol. 85, Jun 2012, pp. 245130.

[48] Rodríguez-Guzmán, R., Jiménez-Hoyos, C. A., Schutski, R., and Scuseria, G. E., "Multireference symmetry-projected variational approaches for ground and excited states of the one-dimensional Hubbard model," *Phys. Rev. B*, Vol. 87, Jun 2013, pp. 235129.

[49] LeBlanc, J. P. F., Antipov, A. E., Becca, F., Bulik, I. W., Chan, G. K.-L., Chung, C.-M., Deng, Y., Ferrero, M., Henderson, T. M., Jimnez-Hoyos, C. A., Kozik, E., Liu, X.-W., Millis, A. J., Prokof'ev, N. V., Qin, M., Scuseria, G. E., Shi, H., Svistunov, B. V., Tocchio, L. F., Tupitsyn, I. S., White, S. R., Zhang, S., Zheng, B.-X., Zhu, Z., and Gull, E., 2015.

[50] van Delft, D., *Freezing physics : Heike Kamerlingh Onnes and the quest for cold.*, Amsterdam, KNAW, 2007.

[51] Shao, H. M., Shen, L. J., Shen, J. C., Hua, X. Y., Yuan, P. F., and Yao, X. X., "Synthesis of single-phase HgBa $_2$Ca $_2$Cu $_3$O $_{8+}$ superconductor," *Physica C Superconductivity*, Vol. 232, Oct. 1994, pp. 5–9.

[52] Timusk, T. and Statt, B., "The pseudogap in high-temperature superconductors: an experimental survey," *Reports on Progress in Physics*, Vol. 62, Jan. 1999, pp. 61–122.

[53] Falicov, L. M. and Kimball, J. C., "Simple Model for Semiconductor-Metal Transitions: $\mathrm{SmB_6}$ and Transition-Metal Oxides," *Phys. Rev. Lett.*, Vol. 22, May 1969, pp. 997–999.

[54] Jefferson, J., "Derivation of the t-J model for high temperature superconductivity," *Physica B: Condensed Matter*, Vol. 165, 1990, pp. 1013 – 1014.

[55] Emery, V. J., "Theory of high-T_c superconductivity in oxides," *Phys. Rev. Lett.*, Vol. 58, Jun 1987, pp. 2794–2797.

[56] Heisenberg, W., "Zur Theorie des Ferromagnetismus," *Zeit. Phys.*, Vol. 49, No. 9-10, 1928, pp. 619–636.

[57] Anderson, P. W., "The Resonating Valence Bond State in La2CuO4 and Superconductivity," *Science*, Vol. 235, No. 4793, 1987, pp. 1196–1198.

[58] Scalapino, D., "Numerical Studies of the 2D Hubbard Model," *Handbook of High-Temperature Superconductivity*, edited by J. Schrieffer and J. Brooks, Springer New York, 2007, pp. 495–526.

[59] de Boer, J. H. and Verwey, E. J. W., "Semi-conductors with partially and with completely filled 3 d -lattice bands," *Proceedings of the Physical Society*, Vol. 49, No. 4S, 1937, pp. 59.

[60] Mott, N. F. and Peierls, R., "Discussion of the paper by de Boer and Verwey," *Proceedings of the Physical Society*, Vol. 49, No. 4S, 1937, pp. 72.

[61] Anderson, P., *The theory of Superconductivity in the High-Tc Cuprate Superconductors*, Princeton University Press, 1997.

[62] de' Medici, L., Wang, X., Capone, M., and Millis, A. J., "Correlation strength, gaps, and particle-hole asymmetry in high-T_c cuprates: A dynamical mean field study of the three-band copper-oxide model," *Phys. Rev. B*, Vol. 80, Aug 2009, pp. 054501.

[63] Weber, C., Haule, K., and Kotliar, G., "Optical weights and waterfalls in doped charge-transfer insulators: A local density approximation and dynamical mean-field theory study of $La_{2-x}Sr_xCuO_4$," *Phys. Rev. B*, Vol. 78, Oct 2008, pp. 134519.

[64] Hanke, W., Kiesel, M. L., Brehm, S., Aichhorn, M., and Arrigoni, E., "The 3-band Hubbard-model versus the 1-band model for the high-T¡sub¿c¡/sub¿ cuprates: Pairing dynamics, superconductivity and the ground-state phase diagram," Vol. 188, No. 1, 2010, pp. 15–32.

[65] Rger, R., Tocchio, L. F., Valent, R., and Gros, C., "The phase diagram of the square lattice bilayer Hubbard model: a variational Monte Carlo study," *New Journal of Physics*, Vol. 16, No. 3, 2014, pp. 033010.

[66] Kancharla, S. S. and Okamoto, S., "Band insulator to Mott insulator transition in a bilayer Hubbard model," *Phys. Rev. B*, Vol. 75, May 2007, pp. 193103.

[67] Amaricci, A., Camjayi, A., Haule, K., Kotliar, G., Tanasković, D., and Dobrosavljević, V., "Extended Hubbard model: Charge ordering and Wigner-Mott transition," *Phys. Rev. B*, Vol. 82, Oct 2010, pp. 155102.

[68] Strohmaier, N., Takasu, Y., Günter, K., Jördens, R., Köhl, M., Moritz, H., and Esslinger, T., "Interaction-Controlled Transport of an Ultracold Fermi Gas," *Phys. Rev. Lett.*, Vol. 99, Nov 2007, pp. 220601.

[69] Jordens, R., Strohmaier, N., Gunter, K., Moritz, H., and Esslinger, T., "A Mott insulator of fermionic atoms in an optical lattice," *Nature*, Vol. 455, No. 7210, Sep 2008, pp. 204–207.

[70] Bethe, H., "Zur Theorie der Metalle," *Zeitschrift für Physik*, Vol. 71, No. 3, 1931, pp. 205–226.

[71] Lieb, E. H. and Wu, F. Y., "Absence of Mott Transition in an Exact Solution of the Short-Range, One-Band Model in One Dimension," *Phys. Rev. Lett.*, Vol. 20, Jun 1968, pp. 1445–1448.

[72] Georges, A. and Kotliar, G., "Hubbard model in infinite dimensions," *Phys. Rev. B*, Vol. 45, Mar 1992, pp. 6479–6483.

[73] Georges, A., Kotliar, G., Krauth, W., and Rozenberg, M. J., "Dynamical mean-field theory of strongly correlated fermion systems and the limit of infinite dimensions," *Rev. Mod. Phys.*, Vol. 68, Jan 1996, pp. 13–125.

[74] Bohm, D. and Pines, D., "A Collective Description of Electron Interactions: III. Coulomb Interactions in a Degenerate Electron Gas," *Phys. Rev.*, Vol. 92, Nov 1953, pp. 609–625.

[75] Anisimov, V. I., Poteryaev, A. I., Korotin, M. A., Anokhin, A. O., and Kotliar, G., "First-principles calculations of the electronic structure and spectra of strongly correlated systems: dynamical mean-field theory," *Journal of Physics: Condensed Matter*, Vol. 9, No. 35, 1997, pp. 7359.

[76] Biermann, S., Aryasetiawan, F., and Georges, A., "First-Principles Approach to the Electronic Structure of Strongly Correlated Systems: Combining the GW Approximation and Dynamical Mean-Field Theory," *Phys. Rev. Lett.*, Vol. 90, Feb 2003, pp. 086402.

[77] Vollhardt, D., "Dynamical Mean-Field Theory of Electronic Correlations in Models and Materials," *American Institute of Physics Conference Series*, edited by A. Avella and F. Mancini, Vol. 1297 of *American Institute of Physics Conference Series*, Nov. 2010, pp. 339–403.

[78] M.Potthoff, "Self-energy-functional approach to systems of correlated electrons," *Eur.Phys.J.B*, Vol. 32, 2003, pp. 429–436.

[79] Park, H., Haule, K., and Kotliar, G., "Cluster Dynamical Mean Field Theory of the Mott Transition," *Phys. Rev. Lett.*, Vol. 101, Oct 2008, pp. 186403.

[80] Biroli, G., Parcollet, O., and Kotliar, G., "Cluster dynamical mean-field theories: Causality and classical limit," *Phys. Rev. B*, Vol. 69, May 2004, pp. 205108.

[81] Parcollet, O., Biroli, G., and Kotliar, G., “Cluster Dynamical Mean Field Analysis of the Mott Transition,” *Phys. Rev. Lett.*, Vol. 92, Jun 2004, pp. 226402.

[82] Torchinsky, D. H., Mahmood, F., Bollinger, A. T., Boovi, I., and Gedik, N., “Fluctuating charge-density waves in a cuprate superconductor,” *Nat Mater*, Vol. 12, No. 5, May 2013, pp. 387–391.

[83] Kotliar, G., Savrasov, S. Y., Pálsson, G., and Biroli, G., “Cellular Dynamical Mean Field Approach to Strongly Correlated Systems,” *Phys. Rev. Lett.*, Vol. 87, Oct 2001, pp. 186401.

[84] Lichtenstein, A. I. and Katsnelson, M. I., “Antiferromagnetism and ***d*** -wave superconductivity in cuprates: A cluster dynamical mean-field theory,” *Phys. Rev. B*, Vol. 62, Oct 2000, pp. R9283–R9286.

[85] Rubtsov, A. N., Katsnelson, M. I., and Lichtenstein, A. I., “Dual fermion approach to nonlocal correlations in the Hubbard model,” *Phys. Rev. B*, Vol. 77, Jan 2008, pp. 033101.

[86] Toschi, A., Katanin, A. A., and Held, K., “Dynamical vertex approximation: A step beyond dynamical mean-field theory,” *Phys. Rev. B*, Vol. 75, Jan 2007, pp. 045118.

[87] Slezak, C., Jarrell, M., Maier, T., and Deisz, J., “Multi-scale extensions to quantum cluster methods for strongly correlated electron systems,” *Journal of Physics: Condensed Matter*, Vol. 21, No. 43, 2009, pp. 435604.

[88] Potthoff, M., *Self-Energy-Functional Theory*, Springer Berlin Heidelberg, Berlin, Heidelberg, 2012, pp. 303–339.

[89] Maier, T. A., Jarrell, M., Schulthess, T. C., Kent, P. R. C., and White, J. B., “Systematic Study of d-Wave Superconductivity in the 2D Repulsive Hubbard Model,” *Phys. Rev. Lett.*, Vol. 95, Nov 2005, pp. 237001.

[90] Jarrell, M., Maier, T., Huscroft, C., and Moukouri, S., “Quantum Monte Carlo algorithm for nonlocal corrections to the dynamical mean-field approximation,” *Phys. Rev. B*, Vol. 64, Oct 2001, pp. 195130.

[91] Huscroft, C., Jarrell, M., Maier, T., Moukouri, S., and Tahvildarzadeh, A. N., “Pseudogaps in the 2D Hubbard Model,” *Phys. Rev. Lett.*, Vol. 86, Jan 2001, pp. 139–142.

[92] Gull, E., Werner, P., Parcollet, O., and Troyer, M., “Continuous-time auxiliary-field Monte Carlo for quantum impurity models,” *EPL (Europhysics Letters)*, Vol. 82, No. 5, 2008, pp. 57003.

[93] Rombouts, S., Heyde, K., and Jachowicz, N., “A discrete Hubbard-Stratonovich decomposition for general, fermionic two-body interactions,” *Physics Letters A*, Vol. 242, No. 4, 1998, pp. 271 – 276.

[94] Gull, E., Staar, P., Fuchs, S., Nukala, P., Summers, M. S., Pruschke, T., Schulthess, T. C., and Maier, T., "Submatrix updates for the continuous-time auxiliary-field algorithm," *Phys. Rev. B*, Vol. 83, Feb 2011, pp. 075122.

[95] Jarrell, M. and Gubernatis, J., "Bayesian inference and the analytic continuation of imaginary-time quantum Monte Carlo data," *Physics Reports*, Vol. 269, No. 3, 1996, pp. 133 – 195.

[96] Levy, R., LeBlanc, J. P. F., and Gull, E., "Implementation of the Maximum Entropy Method for Analytic Continuation," *ArXiv e-prints*, June 2016.

[97] Damascelli, A., Hussain, Z., and Shen, Z.-X., "Angle-resolved photoemission studies of the cuprate superconductors," *Rev. Mod. Phys.*, Vol. 75, Apr 2003, pp. 473–541.

[98] Pessaud, S., Gervais, F., de Sousa, D., Lobo, R., Champeaux, C., Marchet, P., Catherinot, A., Longuet, J. L., and Ravel, F., "Optical conductivity of high- T c cuprate thin films deposited by multi-target laser ablation," *Journal of Physics: Condensed Matter*, Vol. 12, No. 7, 2000, pp. 1517.

[99] Kupi, I., "Resonant two-magnon Raman scattering in high-Tc cuprates," *Journal of Raman Spectroscopy*, Vol. 42, No. 5, 2011, pp. 998–1006.

[100] Tallon, J. L., Bernhard, C., and Niedermayer, C., "Muon spin relaxation studies of superconducting cuprates," *Superconductor Science and Technology*, Vol. 10, No. 7A, 1997, pp. A38.

[101] Le Tacon, M., Bosak, A., Souliou, S. M., Dellea, G., Loew, T., Heid, R., Bohnen, K.-P., Ghiringhelli, G., Krisch, M., and Keimer, B., "Inelastic X-ray scattering in YBa2Cu3O6.6 reveals giant phonon anomalies and elastic central peak due to charge-density-wave formation," *Nat Phys*, Vol. 10, No. 1, Jan 2014, pp. 52–58, Article.

[102] Ashby, P. E. C. and Carbotte, J. P., "*c*," *Phys. Rev. B*, Vol. 87, May 2013, pp. 184514.

[103] Tomczak, J. M. and Biermann, S., "Optical properties of correlated materials Or why intelligent windows may look dirty," *physica status solidi (b)*, Vol. 246, No. 9, 2009, pp. 1996–2005.

[104] Tomczak, J. M., Poteryaev, A. I., and Biermann, S., "Momentum-resolved spectroscopy of correlated metals: A view from dynamical mean field theory," *Comptes Rendus Physique*, Vol. 10, No. 6, 2009, pp. 537 – 547, Theoretical spectroscopy-Spectroscopie thorique.

[105] Yang, S.-X., Terletska, H., Meng, Z. Y., Moreno, J., and Jarrell, M., "Mean-field embedding of the dual-fermion approach for correlated electron systems," *Phys. Rev. E*, Vol. 88, Dec 2013, pp. 063306.

[106] Rohringer, G., Toschi, A., Hafermann, H., Held, K., Anisimov, V. I., and Katanin, A. A., "One-particle irreducible functional approach: A route to diagrammatic extensions of the dynamical mean-field theory," *Phys. Rev. B*, Vol. 88, Sep 2013, pp. 115112.

[107] Taranto, C., Andergassen, S., Bauer, J., Held, K., Katanin, A., Metzner, W., Rohringer, G., and Toschi, A., "From Infinite to Two Dimensions through the Functional Renormalization Group," *Phys. Rev. Lett.*, Vol. 112, May 2014, pp. 196402.

[108] Gunnarsson, O., Schäfer, T., LeBlanc, J. P. F., Gull, E., Merino, J., Sangiovanni, G., Rohringer, G., and Toschi, A., "Fluctuation Diagnostics of the Electron Self-Energy: Origin of the Pseudogap Physics," *Phys. Rev. Lett.*, Vol. 114, Jun 2015, pp. 236402.

[109] Hochkeppel, S., Assaad, F. F., and Hanke, W., "Dynamical-quantum-cluster approach to two-particle correlation functions in the Hubbard model," *Phys. Rev. B*, Vol. 77, May 2008, pp. 205103.

[110] Kinza, M. and Honerkamp, C., "Two-particle correlations in a functional renormalization group scheme using a dynamical mean-field theory approach," *Phys. Rev. B*, Vol. 88, Nov 2013, pp. 195136.

[111] Staar, P., Maier, T., and Schulthess, T. C., "Two-particle correlations in a dynamic cluster approximation with continuous momentum dependence: Superconductivity in the two-dimensional Hubbard model," *Phys. Rev. B*, Vol. 89, May 2014, pp. 195133.

[112] Macridin, A., Jarrell, M., Maier, T., Kent, P. R. C., and D'Azevedo, E., "Pseudogap and Antiferromagnetic Correlations in the Hubbard Model," *Phys. Rev. Lett.*, Vol. 97, Jul 2006, pp. 036401.

[113] Kuneš, J., "Efficient treatment of two-particle vertices in dynamical mean-field theory," *Phys. Rev. B*, Vol. 83, Feb 2011, pp. 085102.

[114] Janiš, V., "Stability of self-consistent solutions for the Hubbard model at intermediate and strong coupling," *Phys. Rev. B*, Vol. 60, Oct 1999, pp. 11345–11360.

[115] Baym, G. and Kadanoff, L. P., "Conservation Laws and Correlation Functions," *Phys. Rev.*, Vol. 124, Oct 1961, pp. 287–299.

[116] Nambu, Y., "Quasi-Particles and Gauge Invariance in the Theory of Superconductivity," *Phys. Rev.*, Vol. 117, Feb 1960, pp. 648–663.

[117] Baym, G. and Kadanoff, L. P., "Conservation Laws and Correlation Functions," *Phys. Rev.*, Vol. 124, Oct 1961, pp. 287–299.

[118] Fotso, H., Yang, S., Chen, K., Pathak, S., Moreno, J., Jarrell, M., Mikelsons, K., Khatami, E., and Galanakis, D., *Dynamical Cluster Approximation*, Springer-Verlag Berlin Heidelberg, 2012.

[119] White, S. R., Scalapino, D. J., Sugar, R. L., Loh, E. Y., Gubernatis, J. E., and Scalettar, R. T., "Numerical study of the two-dimensional Hubbard model," *Phys. Rev. B*, Vol. 40, Jul 1989, pp. 506–516.

[120] White, S. R., Scalapino, D. J., Sugar, R. L., Bickers, N. E., and Scalettar, R. T., "Attractive and repulsive pairing interaction vertices for the two-dimensional Hubbard model," *Phys. Rev. B*, Vol. 39, Jan 1989, pp. 839–842.

[121] Deng, Y., Kozik, E., Prokof'ev, N. V., and Svistunov, B. V., "Emergent BCS regime of the two-dimensional fermionic Hubbard model: Ground-state phase diagram," *EPL (Europhysics Letters)*, Vol. 110, No. 5, 2015, pp. 57001.

[122] Khatami, E., Scalettar, R. T., and Singh, R. R. P., "Finite-temperature superconducting correlations of the Hubbard model," *Phys. Rev. B*, Vol. 91, Jun 2015, pp. 241107.

[123] Luitz, D., *Numerical methods and applications in many fermion systems*, Ph.D. thesis, Julius-Maximilians-Universitat Wurzburg, Wurzburg, 2012.

[124] Chen, X., LeBlanc, J. P. F., and Gull, E., "Superconducting Fluctuations in the Normal State of the Two-Dimensional Hubbard Model," *Phys. Rev. Lett.*, Vol. 115, Sep 2015, pp. 116402.

[125] Moreo, A., "Pairing correlations in the two-dimensional Hubbard model," *Phys. Rev. B*, Vol. 45, Mar 1992, pp. 5059–5061.

[126] Moreo, A. and Scalapino, D. J., "Correlations in the two-dimensional Hubbard model," *Phys. Rev. B*, Vol. 43, Apr 1991, pp. 8211–8216.

[127] Chubukov, A. V. and Lu, J. P., "Pairing instabilities in the two-dimensional Hubbard model," *Phys. Rev. B*, Vol. 46, Nov 1992, pp. 11163–11166.

[128] Deng, Y., Kozik, E., Prokof'ev, N. V., and Svistunov, B. V., "Emergent BCS regime of the two-dimensional fermionic Hubbard model: Ground-state phase diagram," *EPL (Europhysics Letters)*, Vol. 110, No. 5, 2015, pp. 57001.

[129] Arita, R. and Held, K., "Crossover from d-wave to p-wave pairing in the $t - t^{'}$ Hubbard model at zero temperature," *Phys. Rev. B*, Vol. 73, Feb 2006, pp. 064515.

[130] Raghu, S., Kivelson, S. A., and Scalapino, D. J., "Superconductivity in the repulsive Hubbard model: An asymptotically exact weak-coupling solution," *Phys. Rev. B*, Vol. 81, Jun 2010, pp. 224505.

[131] Arita, R., Kuroki, K., and Aoki, H., "d- and p-Wave Superconductivity Mediated by Spin Fluctuations in Two- and Three-Dimensional Single-Band Repulsive Hubbard Model," *Journal of the Physical Society of Japan*, Vol. 69, No. 4, 2000, pp. 1181–1191.

[132] dos Santos, R. R., "Enhanced pairing in the repulsive Hubbard model with next-nearest-neighbor hopping," *Phys. Rev. B*, Vol. 39, Apr 1989, pp. 7259–7262.

[133] Tremblay, A.-M., "Two-Particle-Self-Consistent Approach for the Hubbard Model," *Strongly Correlated Systems*, edited by A. Avella and F. Mancini, Vol. 171 of *Springer Series in Solid-State Sciences*, Springer Berlin Heidelberg, 2012, pp. 409–453.

[134] Werner, P., Gull, E., Parcollet, O., and Millis, A. J., "Momentum-selective metal-insulator transition in the two-dimensional Hubbard model: An 8-site dynamical cluster approximation study," *Phys. Rev. B*, Vol. 80, No. 4, 2009, pp. 045120.

[135] Gull, E., Parcollet, O., Werner, P., and Millis, A. J., "Momentum-sector-selective metal-insulator transition in the eight-site dynamical mean-field approximation to the Hubbard model in two dimensions," *Phys. Rev. B*, Vol. 80, No. 24, Dec 2009, pp. 245102.

[136] Kyung, B., Landry, J.-S., and Tremblay, A.-M. S., "Antiferromagnetic fluctuations and d -wave superconductivity in electron-doped high-temperature superconductors," *Phys. Rev. B*, Vol. 68, Nov 2003, pp. 174502.

[137] Sordi, G., Sémon, P., Haule, K., and Tremblay, A.-M. S., "Strong Coupling Superconductivity, Pseudogap, and Mott Transition," *Phys. Rev. Lett.*, Vol. 108, May 2012, pp. 216401.

[138] Gull, E. and Millis, A. J., "Energetics of superconductivity in the two-dimensional Hubbard model," *Phys. Rev. B*, Vol. 86, Dec 2012, pp. 241106.

[139] Martins, G. B., Xavier, J. C., Arrachea, L., and Dagotto, E., "Qualitative understanding of the sign of $t^{'}$ asymmetry in the extended $t-J$ model and relevance for pairing properties," *Phys. Rev. B*, Vol. 64, Oct 2001, pp. 180513.

[140] Zheng, B.-X. and Kin-Lic Chan, G., "Ground-state phase diagram of the square lattice Hubbard model from density matrix embedding theory," *ArXiv e-prints*, April 2015.

[141] White, S. R. and Scalapino, D. J., "Competition between stripes and pairing in a $t-t^{'}-J$ model," *Phys. Rev. B*, Vol. 60, Jul 1999, pp. R753–R756.

[142] Pavarini, E., Dasgupta, I., Saha-Dasgupta, T., Jepsen, O., and Andersen, O. K., "Band-Structure Trend in Hole-Doped Cuprates and Correlation with $T_{c\max}$," *Phys. Rev. Lett.*, Vol. 87, Jul 2001, pp. 047003.

[143] Gull, E., Werner, P., Wang, X., Troyer, M., and Millis, A. J., "Local order and the gapped phase of the Hubbard model: A plaquette dynamical mean-field investigation," *EPL (Europhysics Letters)*, Vol. 84, No. 3, 2008, pp. 37009.

[144] Gull, E., Ferrero, M., Parcollet, O., Georges, A., and Millis, A. J., "Momentum-space anisotropy and pseudogaps: A comparative cluster dynamical mean-field analysis of the doping-driven metal-insulator transition in the two-dimensional Hubbard model," *Phys. Rev. B*, Vol. 82, Oct 2010, pp. 155101.

[145] Chubukov, A. V. and Lu, J. P., "Pairing instabilities in the two-dimensional Hubbard model," *Phys. Rev. B*, Vol. 46, Nov 1992, pp. 11163–11166.

[146] Baranov, M. A. and Kagan, M. Y., *Z. Phys. B*, Vol. 86, 1992, pp. 237.

[147] Fukazawa, H. and Yamada, K., *J. Phys. Soc. Japan*, Vol. 71, 2001, pp. 1541.

[148] Rømer, A. T., Kreisel, A., Eremin, I., Malakhov, M. A., Maier, T. A., Hirschfeld, P. J., and Anderson, B. M., "Pairing symmetry of the one-band Hubbard model in the paramagnetic weak-coupling limit: a numerical RPA study," *ArXiv e-prints*, June 2015.

[149] Arita, R. and Held, K., "Crossover from d-wave to p-wave pairing in the $t - t'$ Hubbard model at zero temperature," *Phys. Rev. B*, Vol. 73, Feb 2006, pp. 064515.

[150] Bulut, N., Scalapino, D. J., and White, S. R., "Comparison of Monte Carlo and diagrammatic calculations for the two-dimensional Hubbard model," *Phys. Rev. B*, Vol. 47, Feb 1993, pp. 2742–2753.

[151] Daré, A.-M., Chen, L., and Tremblay, A.-M. S., "Comparisons between Monte Carlo simulations and a simple crossing-symmetric approach to the Hubbard model at low density," *Phys. Rev. B*, Vol. 49, Feb 1994, pp. 4106–4118.

[152] Chubukov, A. V., "Kohn-Luttinger effect and the instability of a two-dimensional repulsive Fermi liquid at T =0," *Phys. Rev. B*, Vol. 48, Jul 1993, pp. 1097–1104.

[153] Chen, X., LeBlanc, J. P. F., and Gull, E., "Simulation of the NMR response in the pseudogap regime of the cuprates," *Nature Communications*, Vol. 8, Apr 2017, pp. 14986 EP –, Article.

[154] J. A. Pople, W. G. Schneider, H. J. B., *High Resolution Nuclear Magnetic Resonance*, McGraw-Hill Inc.,US, 1959.

[155] Warren, W. W., Walstedt, R. E., Brennert, G. F., Cava, R. J., Tycko, R., Bell, R. F., and Dabbagh, G., "Cu spin dynamics and superconducting precursor effects in planes above T_c in $\mathrm{YBa_2Cu_3O_{6.7}}$," *Phys. Rev. Lett.*, Vol. 62, Mar 1989, pp. 1193–1196.

[156] Alloul, H., Ohno, T., and Mendels, P., "$^{89}\mathrm{Y}$ NMR evidence for a fermi-liquid behavior in $\mathrm{YBa_2Cu_3O_{6+x}}$," *Phys. Rev. Lett.*, Vol. 63, Oct 1989, pp. 1700–1703.

[157] Walstedt, R. E., Warren, W. W., Bell, R. F., Cava, R. J., Espinosa, G. P., Schneemeyer, L. F., and Waszczak, J. V., "$^{63}\mathrm{Cu}$ NMR shift and linewidth anomalies in the T_c=60 K phase of Y-Ba-Cu-O," *Phys. Rev. B*, Vol. 41, May 1990, pp. 9574–9577.

[158] Takigawa, M., Reyes, A. P., Hammel, P. C., Thompson, J. D., Heffner, R. H., Fisk, Z., and Ott, K. C., "Cu and O NMR studies of the magnetic properties of $\mathrm{YBa_2Cu_3O_{6.63}}$ (T_c=62 K)," *Phys. Rev. B*, Vol. 43, Jan 1991, pp. 247–257.

[159] Mila, F. and Rice, T., “Analysis of magnetic resonance experiments in YBa2Cu3O7,” *Physica C: Superconductivity*, Vol. 157, No. 3, 1989, pp. 561 – 570.

[160] Shastry, B. S., “*t* - *J* model and nuclear magnetic relaxation in high-T_c materials,” *Phys. Rev. Lett.*, Vol. 63, Sep 1989, pp. 1288–1291.

[161] Barzykin, V. and Pines, D., “Magnetic scaling in cuprate superconductors,” *Phys. Rev. B*, Vol. 52, Nov 1995, pp. 13585–13600.

[162] Zha, Y., Barzykin, V., and Pines, D., “NMR and neutron-scattering experiments on the cuprate superconductors: A critical re-examination,” *Phys. Rev. B*, Vol. 54, Sep 1996, pp. 7561–7574.

[163] Kubo, R., “The fluctuation-dissipation theorem,” *Reports on Progress in Physics*, Vol. 29, No. 1, 1966, pp. 255.

[164] Monien, H., Pines, D., and Takigawa, M., “Application of the antiferromagnetic-Fermi-liquid theory to NMR experiments on $\mathrm{YBa_2Cu_3O_{6.63}}$,” *Phys. Rev. B*, Vol. 43, Jan 1991, pp. 258–274.

[165] Nakano, T., Oda, M., Manabe, C., Momono, N., Miura, Y., and Ido, M., “Magnetic properties and electronic conduction of superconducting $\mathrm{La_{2-\mathit{x}}Sr_{\mathit{x}}CuO_4}$,” *Phys. Rev. B*, Vol. 49, Jun 1994, pp. 16000–16008.

[166] Millis, A. J., Monien, H., and Pines, D., “Phenomenological model of nuclear relaxation in the normal state of $\mathrm{YBa_2Cu_3O_7}$,” *Phys. Rev. B*, Vol. 42, Jul 1990, pp. 167–178.

[167] Bulut, N., Hone, D. W., Scalapino, D. J., and Bickers, N. E., “Knight shifts and nuclear-spin-relaxation rates for two-dimensional models of $\mathrm{CuO_2}$,” *Phys. Rev. B*, Vol. 41, Feb 1990, pp. 1797–1811.

[168] Bulut, N. and Scalapino, D. J., “Analysis of NMR data in the superconducting state of $\mathrm{YBa_2Cu_3O_7}$,” *Phys. Rev. Lett.*, Vol. 68, Feb 1992, pp. 706–709.

[169] Randeria, M., Trivedi, N., Moreo, A., and Scalettar, R. T., “Pairing and spin gap in the normal state of short coherence length superconductors,” *Phys. Rev. Lett.*, Vol. 69, Sep 1992, pp. 2001–2004.

[170] Tremblay, A.-M. S., Kyung, B., and Sénéchal, D., “Pseudogap and high-temperature superconductivity from weak to strong coupling. Towards a quantitative theory (Review Article),” *Low Temperature Physics*, Vol. 32, No. 4, 2006, pp. 424–451.

[171] Kyung, B., Kancharla, S. S., Sénéchal, D., Tremblay, A.-M. S., Civelli, M., and Kotliar, G., “Pseudogap induced by short-range spin correlations in a doped Mott insulator,” *Phys. Rev. B*, Vol. 73, Apr 2006, pp. 165114.

[172] Curro, N. J., Imai, T., Slichter, C. P., and Dabrowski, B., “High-temperature $^{63}\mathrm{Cu(2)}$ nuclear quadrupole and magnetic resonance measurements of $\mathrm{YBa_2Cu_4O_8}$,” *Phys. Rev. B*, Vol. 56, Jul 1997, pp. 877–885.

[173] Ohsugi, S., Kitaoka, Y., Ishida, K., qing Zheng, G., and Asayama, K., "Cu NMR and NQR Studies of High-T c Superconductor La2-xSrxCuO4," *Journal of the Physical Society of Japan*, Vol. 63, No. 2, 1994, pp. 700–715.

[174] Johnston, D. C., "Magnetic Susceptibility Scaling in $\mathrm{La}_{2-x}\mathrm{Sr}_x\mathrm{CuO}_{4-y}$," *Phys. Rev. Lett.*, Vol. 62, Feb 1989, pp. 957–960.

[175] Lin, N., Gull, E., and Millis, A. J., "Physics of the pseudogap in eight-site cluster dynamical mean-field theory: Photoemission, Raman scattering, and in-plane and c-axis conductivity," *Phys. Rev. B*, Vol. 82, Jul 2010, pp. 045104.

[176] Vidhyadhiraja, N. S., Macridin, A., Sen, C., Jarrell, M., and Ma, M., "Quantum Critical Point at Finite Doping in the 2D Hubbard Model: A Dynamical Cluster Quantum Monte Carlo Study," *Phys. Rev. Lett.*, Vol. 102, May 2009, pp. 206407.

[177] Sordi, G., Sémon, P., Haule, K., and Tremblay, A.-M. S., "c-axis resistivity, pseudogap, superconductivity, and Widom line in doped Mott insulators," *Phys. Rev. B*, Vol. 87, Jan 2013, pp. 041101.

[178] Trivedi, N. and Randeria, M., "Deviations from Fermi-Liquid Behavior above T_c in 2D Short Coherence Length Superconductors," *Phys. Rev. Lett.*, Vol. 75, Jul 1995, pp. 312–315.

[179] Tomeno, I., Machi, T., Tai, K., Koshizuka, N., Kambe, S., Hayashi, A., Ueda, Y., and Yasuoka, H., "NMR study of spin dynamics at planar oxygen and copper sites in $\mathrm{YBa}_2\mathrm{Cu}_4\mathrm{O}_8$," *Phys. Rev. B*, Vol. 49, Jun 1994, pp. 15327–15334.

[180] Bankay, M., Mali, M., Roos, J., and Brinkmann, D., "Single-spin fluid, spin gap, and *d* -wave pairing in $\mathrm{YBa}_2\mathrm{Cu}_4\mathrm{O}_8$: A NMR and NQR study," *Phys. Rev. B*, Vol. 50, Sep 1994, pp. 6416–6425.

[181] Williams, G. V. M., Tallon, J. L., Quilty, J. W., Trodahl, H. J., and Flower, N. E., "Absence of an Isotope Effect in the Pseudogap in $\mathrm{YBa}_2\mathrm{Cu}_4O_8$ as Determined by High-Resolution ^{89}Y NMR," *Phys. Rev. Lett.*, Vol. 80, Jan 1998, pp. 377–380.

[182] Pennington, C. H. and Slichter, C. P., "Theory of nuclear spin-spin coupling in $\mathrm{YBa}_2\mathrm{Cu}_3\mathrm{O}_{7-\delta}$," *Phys. Rev. Lett.*, Vol. 66, Jan 1991, pp. 381–384.

[183] Imai, T., Slichter, C. P., Yoshimura, K., Katoh, M., and Kosuge, K., "Spin-spin correlation in the quantum critical regime of $\mathrm{La}_2\mathrm{CuO}_4$," *Phys. Rev. Lett.*, Vol. 71, Aug 1993, pp. 1254–1257.

[184] Corey, R. L., Curro, N. J., O'Hara, K., Imai, T., Slichter, C. P., Yoshimura, K., Katoh, M., and Kosuge, K., "$^{63}\mathrm{Cu}(2)$ nuclear quadrupole and nuclear magnetic resonance studies of $\mathrm{YBa}_2\mathrm{Cu}_4\mathrm{O}_8$ in the normal and superconducting states," *Phys. Rev. B*, Vol. 53, Mar 1996, pp. 5907–5914.

[185] Stern, R., Mali, M., Roos, J., and Brinkmann, D., "Spin pseudogap and interplane coupling in $\mathrm{Y_2Ba_4Cu_7O_{15}}$: A $^{63}\mathrm{Cu}$ nuclear spin-spin relaxation study," *Phys. Rev. B*, Vol. 51, Jun 1995, pp. 15478–15483.

[186] Walstedt, R. E., Shastry, B. S., and Cheong, S.-W., "NMR, neutron scattering, and the one-band model of $\mathrm{La_{2-x}Sr_xCuO_4}$," *Phys. Rev. Lett.*, Vol. 72, May 1994, pp. 3610–3613.

[187] Imai, T., Slichter, C. P., Yoshimura, K., and Kosuge, K., "Low frequency spin dynamics in undoped and Sr-doped $\mathrm{La_2CuO_4}$," *Phys. Rev. Lett.*, Vol. 70, Feb 1993, pp. 1002–1005.

[188] qing Zheng, G., Odaguchi, T., Mito, T., Kitaoka, Y., Asayama, K., and Kodama, Y., "63Cu NQR/NMR Study of Zn-Substituted YBa2 Cu4 O8 Effect of Impurity on Spin-Gap-Like Behavior," *Journal of the Physical Society of Japan*, Vol. 62, No. 8, 1993, pp. 2591–2594.

[189] Takigawa, M., Hults, W. L., and Smith, J. L., "Comparison of nuclear spin relaxation rates at Y and O sites in $\mathrm{YBa_2Cu_3O_{7-y}}$," *Phys. Rev. Lett.*, Vol. 71, Oct 1993, pp. 2650–2653.

[190] Tranquada, J. M., Gehring, P. M., Shirane, G., Shamoto, S., and Sato, M., "Neutron-scattering study of the dynamical spin susceptibility in $\mathrm{YBa_2Cu_3O_{6.6}}$," *Phys. Rev. B*, Vol. 46, Sep 1992, pp. 5561–5575.

[191] Millis, A. J. and Monien, H., "Spin Gaps and Spin Dynamics in $\mathrm{La_{2-x}Sr_xCuO_4}$ and $\mathrm{YBa_2Cu_3O_{7-\delta}}$," *Phys. Rev. Lett.*, Vol. 70, May 1993, pp. 2810–2813.

[192] V. Jani, V. P., "Vertices for correlated electron systems with anomalous propagators," *Sci. Lett. J.*, Vol. 3, 2014.

[193] Magishi, K., Gavilano, J. L., Pedrini, B., Hinderer, J., Weller, M., Ott, H. R., Kazakov, S. M., and Karpinski, J., "Evidence for s-wave superconductivity in the β-pyrochlore oxide $\mathrm{RbOs_2O_6}$," *Phys. Rev. B*, Vol. 71, Jan 2005, pp. 024524.

[194] Michael Jurkutat, Jonas Kohlrautz, S. R. A. E. G. V. W. and Haase, J., "High-Tc Copper Oxide Superconductors and Related Novel," *Springer Series in Materials Science*, edited by A. B.-H. . H. K. . A. Bianconi, chap. 8, Springer Nature, 2017.

[195] Holczer, K., Forro, L., Mihály, L., and Grüner, G., "Observation of the conductivity coherence peak in superconducting $\mathrm{Bi_2Sr_2CaCu_2O_8}$ single crystals," *Phys. Rev. Lett.*, Vol. 67, Jul 1991, pp. 152–155.

[196] Hammel, P. C., Takigawa, M., Heffner, R. H., Fisk, Z., and Ott, K. C., "Spin dynamics at oxygen sites in $\mathrm{YBa_2Cu_3O_7}$," *Phys. Rev. Lett.*, Vol. 63, Oct 1989, pp. 1992–1995.

[197] Hebel, L. C. and Slichter, C. P., "Nuclear Spin Relaxation in Normal and Superconducting Aluminum," *Phys. Rev.*, Vol. 113, Mar 1959, pp. 1504–1519.

[198] Ohsugi, S., Kitaoka, Y., Ishida, K., qing Zheng, G., and Asayama, K., "Cu NMR and NQR Studies of High-T c Superconductor La2-xSrxCuO4," *Journal of the Physical Society of Japan*, Vol. 63, No. 2, 1994, pp. 700–715.

[199] Ning, F. L., Ahilan, K., Imai, T., Sefat, A. S., Jin, R., McGuire, M. A., Sales, B. C., and Mandrus, D., "^{59}Co," *Phys. Rev. B*, Vol. 79, Apr 2009, pp. 140506.

[200] Monien, H. and Pines, D., "Spin excitations and pairing gaps in the superconducting state of $\mathrm{YBa_2Cu_3O_{7-\delta}}$," *Phys. Rev. B*, Vol. 41, Apr 1990, pp. 6297–6305.

[201] Moriya, T., Takahashi, Y., and Ueda, K., "Antiferromagnetic Spin Fluctuations and Superconductivity in Two-Dimensional Metals -A Possible Model for High Tc Oxides," *Journal of the Physical Society of Japan*, Vol. 59, No. 8, 1990, pp. 2905–2915.

[202] Bankay, M., Mali, M., Roos, J., and Brinkmann, D., "Single-spin fluid, spin gap, and d-wave pairing in $\mathrm{YBa_2Cu_4O_8}$: A NMR and NQR study," *Phys. Rev. B*, Vol. 50, Sep 1994, pp. 6416–6425.

[203] Barrett, S. E., Durand, D. J., Pennington, C. H., Slichter, C. P., Friedmann, T. A., Rice, J. P., and Ginsberg, D. M., "$^{63}\mathrm{Cu}$," *Phys. Rev. B*, Vol. 41, Apr 1990, pp. 6283–6296.

[204] Yosida, K., "Paramagnetic Susceptibility in Superconductors," *Phys. Rev.*, Vol. 110, May 1958, pp. 769–770.